

Handbook T-I

Sustainable Materials Engineering

Martínez-Vargas, Sergio

Sierra-Grajeda, Juan Manuel

Pérez-Montejo, Salatiel

Mandujano-Ramírez, Humberto Julián

Coordinators



ECORFAN®

Coordinators

Martínez-Vargas, Sergio
Sierra-Grajeda, Juan Manuel
Pérez-Montejo, Salatiel
Mandujano-Ramírez, Humberto Julián

Editor in Chief

Vargas-Delgado, Oscar. PhD

Executive Director

Ramos-Escamilla, María. PhD

Editorial Director

Peralta-Castro, Enrique. MsC

Web Designer

Escamilla-Bouchan, Imelda. PhD

Web Diagrammer

Luna-Soto, Vladimir. PhD

Editorial Assistant

Trejo-Ramos, Iván. BsC

Philologist

Ramos-Arancibia, Alejandra. BsC

ISBN: 978-607-8948-50-5
ECORFAN Publishing Label: 607-8948
HSME Control Number: 2024-14
HSME Classification (2024): 311224-0114

©ECORFAN-México, S.C.

Park Pedregal Business 3580 – Adolfo Ruiz Cortines Boulevard, CP-01900. San Jeronimo Aculco Álvaro Obregón - Mexico City.

No part of this writing protected by the Federal Copyright Law may be reproduced, transmitted or used in any form or by any means, graphic, electronic or mechanical, including, but not limited to, the following: Quotations in radio or electronic journalistic data compilation articles and bibliographic commentaries. For the purposes of articles 13, 162, 163 fraction I, 164 fraction I, 168, 169, 209 fraction III and other relative articles of the Federal Copyright Law. Infringements: Being compelled to prosecute under Mexican copyright law. The use of general descriptive names, registered names, trademarks, or trade names in this publication does not imply, even in the absence of a specific statement, that such names are exempt from the relevant protection in laws and regulations of Mexico and therefore free for general use by the international scientific community. HAMTFE is part of ECORFAN Media [www.ecorfan.org]. Published by ECORFAN-Mexico. All Rights Reserved.

Derivative works: Users may reproduce tables of contents or prepare lists of chapters including abstracts for internal circulation within their institutions or companies. Other than for chapters published under the CC BY license.

Storage or usage: Except as outlined above or as set out in the relevant user license, no part of this publication may be reproduced, stored in a retrieval system or transmitted in any form or by any means, electronic, mechanical, photocopying, recording or otherwise, without prior written permission of the publisher.

The Authors. Published by ECORFAN-Mexico, S.C. for its Holding Mexico on behalf of Handbook HESPCU. This is an open access handbook under the CC BY-NC-ND license [<http://creativecommons.org/licenses/by-nc-nd/4.0/>]

Handbooks

Definition of Handbooks

Scientific Objectives

To support the International Scientific Community in its written production of Science, Technology and Innovation in the CONAHCYT and PRODEP research areas.

ECORFAN-Mexico, S.C. is a Scientific and Technological Company in contribution to the formation of Human Resources focused on the continuity in the critical analysis of International Research and is attached to the RENIECYT of CONAHCYT with number 1702902, its commitment is to disseminate research and contributions of the International Scientific Community, academic institutions, agencies and entities of the public and private sectors and contribute to the linkage of researchers who perform scientific activities, technological developments and training of specialized human resources with governments, businesses and social organizations.

To encourage the interlocution of the International Scientific Community with other study centres in Mexico and abroad and to promote a wide incorporation of academics, specialists and researchers to the serial publication in Science Niches of Autonomous Universities - State Public Universities - Federal IES - Polytechnic Universities - Technological Universities - Federal Technological Institutes - Teacher Training Colleges - Decentralised Technological Institutes - Intercultural Universities - S&T Councils - CONAHCYT Research Centres.

Scope, Coverage and Audience

Handbooks is a product edited by ECORFAN-Mexico S.C. in its Holding with repository in Mexico, it is a refereed and indexed scientific publication. It admits a wide range of contents that are evaluated by academic peers by the double-blind method, on topics related to the theory and practice of the CONAHCYT and PRODEP research areas respectively with diverse approaches and perspectives, which contribute to the dissemination of the development of Science, Technology and Innovation that allow arguments related to decision-making and influence the formulation of international policies in the field of Science. The editorial horizon of ECORFAN-Mexico® extends beyond academia and integrates other segments of research and analysis outside that field, as long as they meet the requirements of argumentative and scientific rigour, in addition to addressing issues of general and current interest of the International Scientific Society.

Editorial Board

CASTILLO - TÉLLEZ, Beatriz. PhD
University of La Rochelle

CERCADO - QUEZADA, Bibiana. PhD
Intitut National Polytechnique Toulouse

FERNANDEZ - ZAYAS, José Luis. PhD
University of Bristol

HERNANDEZ - ESCOBEDO, Quetzalcoatl Cruz. PhD
Universidad Central del Ecuador

RIVAS - PEREA, Pablo. PhD
University of Texas

ROCHA - RANGEL, Enrique. PhD
Oak Ridge National Laboratory

RODRÍGUEZ - MORALES, José Alberto. PhD
Universidad Politécnica de Madrid

VAZQUEZ - MARTINEZ, Ernesto. PhD
University of Alberta

VEGA - PINEDA, Javier. PhD
University of Texas

RODRIGUEZ - ROBLEDO, Gricelda. PhD
Universidad Santander

Arbitration Committee

CASTILLO - QUIÑONES, Javier Emmanuel. PhD
Universidad Autónoma de Baja California

CHÁVEZ-LUGO, Pedro. PhD
Universidad Michoacana de San Nicolás de Hidalgo

FLORES - RAMÍREZ, Oscar. PhD
Universidad Politécnica de Amozoc

GÓMEZ - MERCADO, Abdiel
Instituto Tecnológico de Pachuca

HERNÁNDEZ - GÓMEZ, Víctor Hugo. PhD
Universidad Nacional Autónoma de México

HERRERA - ROMERO, José Vidal. PhD
Universidad Nacional Autónoma de México

MEJIAS - BRIZUELA, Nildia Yamileth. PhD
Instituto Nacional de Astrofísica, Óptica y Electrónica

PÉREZ - ROBLES, Juan Francisco. PhD
Instituto Tecnológico de Saltillo

AGUILAR - VIRGEN, Quetzalli. PhD
Universidad Autónoma de Baja California

RAMÍREZ - COUTIÑO, Víctor Ángel. PhD
Centro de Investigación y Desarrollo Tecnológico en Electroquímica

Assignment of Rights

By submitting Scientific Work to ECORFAN Handbooks, the author undertakes not to submit it simultaneously to other scientific publications for consideration. To do so, the author must complete the Originality Form for his or her Scientific Work.

The authors sign the Authorization Form for their Scientific Work to be disseminated by the means that ECORFAN-Mexico, S.C. in its Holding Mexico considers pertinent for the dissemination and diffusion of their Scientific Work, ceding their Scientific Work Rights.

Declaration of Authorship

Indicate the name of 1 Author and a maximum of 3 Co-authors in the participation of the Scientific Work and indicate in full the Institutional Affiliation indicating the Unit.

Identify the name of 1 author and a maximum of 3 co-authors with the CVU number - PNPC or SNI-CONAHCYT - indicating the level of researcher and their Google Scholar profile to verify their citation level and H index.

Identify the Name of 1 Author and 3 Co-authors maximum in the Science and Technology Profiles widely accepted by the International Scientific Community ORC ID - Researcher ID Thomson - arXiv Author ID - PubMed Author ID - Open ID respectively.

Indicate the contact for correspondence to the Author (Mail and Telephone) and indicate the Contributing Researcher as the first Author of the Scientific Work.

Plagiarism Detection

All Scientific Works will be tested by the PLAGSCAN plagiarism software. If a Positive plagiarism level is detected, the Scientific Work will not be sent to arbitration and the receipt of the Scientific Work will be rescinded, notifying the responsible Authors, claiming that academic plagiarism is typified as a crime in the Penal Code.

Refereeing Process

All Scientific Works will be evaluated by academic peers using the Double-Blind method. Approved refereeing is a requirement for the Editorial Board to make a final decision which will be final in all cases. MARVID® is a spin-off brand of ECORFAN® specialized in providing expert reviewers all of them with PhD degree and distinction of International Researchers in the respective Councils of Science and Technology and the counterpart of CONAHCYT for the chapters of America-Europe-Asia-Africa and Oceania. The identification of authorship should only appear on a first page, which can be removed, in order to ensure that the refereeing process is anonymous and covers the following stages: Identification of ECORFAN Handbooks with their author occupancy rate - Identification of Authors and Co-authors - PLAGSCAN Plagiarism Detection - Review of Authorization and Originality Forms-Assignment to the Editorial Board - Assignment of the pair of Expert Referees - Notification of Opinion - Statement of Observations to the Author - Modified Scientific Work Package for Editing - Publication.

ECORFAN Sustainable Materials Engineering

Volume I

The Handbook will offer volumes of selected contributions from researchers who contribute to the scientific dissemination activity of the Universidad Autónoma del Carmen in their areas of research in Engineering Sciences. In addition to having a total evaluation, in the hands of the directors of the Universidad Autónoma del Carmen the quality and timeliness of its chapters, each individual contribution was refereed to international standards (V|LEX, RESEARCH GATE, MENDELEY, GOOGLE SCHOLAR and REDIB), the Handbook thus proposes to the academic community, recent reports on new developments in the most interesting and promising areas of research in the Science and Technology.

Sustainable Materials Engineering

Handbooks

Coordinators

Martínez-Vargas, Sergio

Sierra-Grajeda, Juan Manuel

Pérez-Montejo, Salatiel

Mandujano-Ramírez, Humberto Julián

Universidad Autónoma del Carmen

December, 2024

DOI: <https://doi.org/10.35429/H.2024.14.1.96>



Preface

The Faculty of Engineering and Architecture of the Universidad Autónoma del Carmen (UNACAR), through the Master's Program in Materials and Energy Engineering, organized the 1st Colloquium of Research in Materials and Energy Engineering, held on October 23-25, 2024, to precede the 5 previous editions of the Master's Student Colloquium. The main purpose of this first colloquium is to open a space for the dissemination and diffusion of research topics developed by students, academics and technologists of the different undergraduate, master's and doctoral programs in the area of science and engineering of UNACAR and other graduate programs in the region, the country and abroad. Specifically, the colloquium seeks to promote discussion, debate and feedback on research advances in the areas of materials, energy systems, environmental sciences, hydrogen technologies, electrochemistry, corrosion, control and instrumentation, modeling and numerical simulation, among others. The organizers and most of the participants of this first colloquium, who belong to research groups of different Academic Bodies and form the “Thematic Network of Materials and Energy Engineering” together with members of national and international institutions, presented the progress of their research through oral presentations, posters, lectures and virtual conferences, workshops, as well as the exhibition of some technological prototypes designed and manufactured by students.

This Handbook “Sustainable Materials Engineering” is a compilation of the most relevant papers presented at the 1st Colloquium on Materials and Energy Engineering Research, which consists of 10 refereed chapters that constitute the most representative topics addressed in this first colloquium. Each of these chapters, which propose to reduce the ecological-environmental impact and improve the use of natural resources, were inspected through the feedback of a Reviewing Committee that contributed to the improvement of the papers published here, which are oriented in the area of materials and energy engineering.

Coordinators:

Martínez-Vargas, Sergio
Sierra-Grajeda, Juan Manuel
Pérez-Montejo, Salatiel
Mandujano-Ramírez, Humberto Julián





Content





	Page
1 Spectroscopic and phytochemical characterization of green corrosion inhibitors from leaves of the <i>Morinda citrifolia</i> plant based on acetone and ethyl acetate Sánchez-Martínez, Víctor Alberto, Figueroa-Ramírez, Sandra Jazmín, Benavides, Olena and Sierra-Grajeda, Juan Manuel	1-8
2 DFT study on the interaction between carbon dioxide and doped fullerene C30 Toxqui-De La Torre, Ana Paulina, Mandujano-Ramírez, Humberto Julián, Martínez-Vargas, Sergio and Patiño-Carachure, Cristóbal	9-18
3 Analysis of the mechanism of formation and growth of carbon nanostructures produced through the mechanical milling of graphite Aguilar-Cruz, Felix, Flores-Gil, Aaron, Álvarez-García, Emilio, Patiño-Carachure, Cristóbal	19-26
4 Analysis of channel sample in thin section by Raman spectroscopy images Castelán-Antúnez, Citli Celeste, Flores-Gil, Aarón, Patiño-Carachure, Cristobal and Urrieta-Almeida, Edgar	27-35
5 Manufacturing and mechanical characterization of eco-friendly blocks using organic waste as aggregate Muñoz-Talango, Dayana G., Abatal, Mohamed and Santiago-de la Cruz, Arlette A.	36-47
6 Design for laser assembly in confocal raman spectroscopy for in-vivo sample study Urrieta-Almeida, Edgar, Flores, Gil Aarón, Benavides, Olena and Bandala-Garces, Magdalena	48-56
7 Evaluation of sinkholes in a civil work by capturing digital images using an unmanned aerial vehicle Pavón-Moreno, Julio, Escorza-Reyes, Marisol, Vergara-Huerta, Filiberto and Canto-Pérez, Emily	57-68
8 Inhibition of both CaSO₄ scales and corrosion using polyelectrolytes Ramírez-Estrada, Alejandro, Mena-Cervantes, Violeta Yasmín, Aguilar-Aguilar, Fidel Alejandro and Hernández-Altamirano, Raúl	69-77
9 Effect of microstructural changes associated with hydrogen damage in API 5L X60 steels Calan-Canche, Damián, Reda-Cruz, Alfredo, González-Sánchez, Jorge and Flores-Chan, J. E.	78-88
10 Effect of heat treatment on hydrogen permeation of API 5L X60 steel in soil solution Calan-Canche, Damián, Pérez-Montejo, Saltiel, Flores-Chan, J.E. and González-Sánchez, Jorge	89-96





Spectroscopic and phytochemical characterization of green corrosion inhibitors from leaves of the *Morinda citrifolia* plant based on acetone and ethyl acetate





Caracterización espectroscópica y fitoquímica de inhibidores verdes de corrosión provenientes de hojas de la planta *Morinda citrifolia* a base de acetona y acetato de etilo

Sánchez-Martínez, Víctor Alberto^a, Figueroa-Ramírez, Sandra Jazmín*^b, Benavides, Olena^c and Sierra-Grajeda, Juan Manuel^d

^a  Universidad Autónoma del Carmen •  LSL-3116-2024 •  0000-0003-0487-8323 •  1088487

^b  Universidad Autónoma del Carmen •  AIB-1429-2022 •  0000-0003-1368-1741 •  164797

^c  Universidad Autónoma del Carmen •  Q-3771-2019 •  0000-0002-8124-0326 •  339830

^d  Universidad Autónoma del Carmen •  LSK-8588-2024 •  0000-0002-0565-6450 •  219284

CONAHCYT classification:

DOI: <https://doi.org/10.35429/H.2024.14.1.8>

Area: Engineering

Field: Engineering

Discipline: Chemical engineering

Subdiscipline: Organic chemistry

Key Handbooks

In this work we present the obtaining and characterization of acetone and ethyl acetate extracts from the leaves of *Morinda citrifolia*, we study these extracts to know their potential as a candidate corrosion inhibitor, we obtained their spectra and phytochemical tests. To understand this work it is necessary to study the FTIR and UV-Vis spectra, to find the functional groups and compounds of the extracts and to check with the phytochemical tests. It is important to mention that these extracts will be further evaluated as green corrosion inhibitors, in order to have an effective, economical and environmentally friendly method to inhibit the corrosion of metals. The organic compounds of the plant are responsible for reducing the corrosion rate of metals, so their identification is crucial for further evaluation. The authors in order in this book chapter have the following number of citations 0, 4, 3 and 0. The author Sánchez-Martínez has a CONAHCYT scholarship, and the rest of the authors have a PRODEP desirable profile and belong to the National System of Researchers (SNI). All authors are from the Universidad Autónoma del Carmen (State Public Institution). The keywords most frequently used are: spectroscopy, phytochemical tests and *Morinda citrifolia*.

Citation: Sánchez-Martínez, Víctor Alberto, Figueroa-Ramírez, Sandra Jazmín, Benavides, Olena and Sierra-Grajeda, Juan Manuel. 2024. Spectroscopic and phytochemical characterization of green corrosion inhibitors from leaves of the *Morinda citrifolia* plant based on acetone and ethyl acetate. 1-8. ECORFAN.

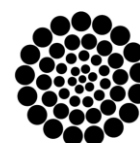
* ✉ [sfigueroa@pampano.unacar.mx]

Handbook shelf URL: <https://www.ecorfan.org/handbooks.php>



ISBN 978-607-8948-50-5/©2009 The Authors. Published by ECORFAN-Mexico, S.C. for its Holding Mexico on behalf of Handbook HRPG. This is an open access chapter under the CC BY-NC-ND license [<http://creativecommons.org/licenses/by-nc-nd/4.0/>]

Peer Review under the responsibility of the Scientific Committee MARVID®- in contribution to the scientific, technological and innovation Peer Review Process by training Human Resources for the continuity in the Critical Analysis of International Research.



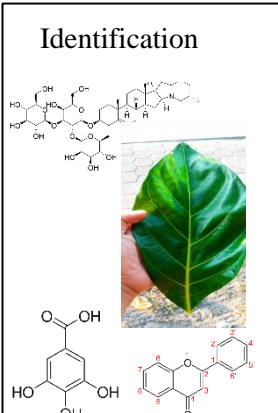

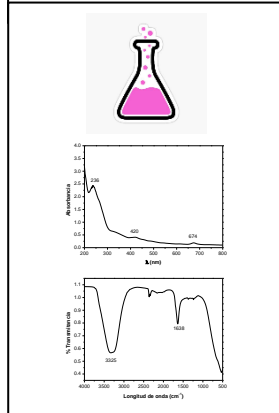
RENIECYT

Registro Nacional de Instituciones y
Empresas Científicas y Tecnológicas

1702902 CONAHCYT

Abstract

Metals suffer corrosion due to the presence of different corrosive media. One way to prevent corrosion is to develop and use corrosion inhibitors that are effective and environmentally friendly. Plant extracts are good candidates because they do not contain toxic substances. In the present work, extracts of *Morinda citrifolia* leaves were obtained and characterized in acetone and ethyl acetate. The extracts were obtained by maceration for 72 hours. Subsequently, they were characterized by spectroscopic and phytochemical techniques. The spectroscopic techniques showed the presence of anthocyanins and phenolic compounds and aromatic compounds. The phytochemical tests showed flavones, saponins and tannins. Studies showed that acetone and ethyl acetate extracts of *Morinda Citrifolia* leaves contain a mixture of organic compounds and their extraction depends on the solvent used.

Spectroscopic and Phytochemical Characterization of extracts from the leaves of the <i>Morinda Citrifolia</i> plant		
Objetivo	Methodology	Contribution
<p>Identification</p> 	<p>Characterization</p> 	<p>Contribution</p> 

Spectroscopy, Phytochemical Test, *Morinda citrifolia*

Resumen

Los metales sufren corrosión debido a la presencia de diferentes medios corrosivos. Una forma de prevenirla es desarrollando y empleando inhibidores de corrosión que sean eficaces y amigables con el ambiente. Los extractos de plantas son buenos candidatos debido a que no contiene sustancias tóxicas. En presente trabajo se obtienen y caracterizan extractos de hojas de la *Morinda citrifolia* en acetona y acetato de etilo. La obtención de los extractos se realizó mediante el proceso de maceración durante 72 horas. Posteriormente, se caracterizaron mediante técnicas espectroscópicas y fitoquímicas. Las técnicas espectroscópicas mostraron la presencia de antocianinas y compuestos fenólicos y compuestos aromáticos. Las pruebas fitoquímicas flavonas, saponinas y taninos. Los estudios realizados mostraron que los extractos de acetona y acetato de etilo de las hojas de *Morinda citrifolia* contienen una mezcla de compuestos orgánicos y su extracción depende de disolvente empleado.

Caracterización Espectroscópica y Fitoquímica de extractos de las hojas de la planta <i>Morinda citrifolia</i>		
Objetivo	Metodología	Contribución
<p>Identificación</p> 	<p>Caracterización</p> 	<p>Contribución</p> 

Espectroscopia, Pruebas Fitoquímicas, *Morinda citrifolia*

Introduction

Corrosion is one of the main problems affecting various industries, due to the use of metallic materials and alloys exposed to different aggressive media such as: acids (H_2SO_4), basic (CaCO_3 , NaOH , NaHCO_3), gases (NH_4 , H_2S , CH_2O), salts (NaCl) and chemicals. To mitigate this phenomenon, different methods have been developed, including protective coatings, cathodic and anodic protection, as well as corrosion inhibitors. The latter are a key alternative, as they can act through different mechanisms such as passivation, film formation and adsorption. However, the main problem with these inhibitors is that they have a high content of heavy metals and are therefore polluting and hazardous. Therefore, plants (leaf, stem, root, fruit) with high phytochemical content have started to be studied, which makes them promising candidates for the development of green corrosion inhibitors.

In southeastern Mexico, there is a great diversity of flora. In particular, the *Morinda citrifolia* tree, commonly known as Noni, belongs to the *Rubiaceae* family. This tree can reach a height of 5 m and its leaves are over 30 cm long, elliptical, large and shiny. In addition, it contains various organic compounds such as iridoids, terpenes, triterpenes, sterols, flavonoids, lignans, steroids, fatty acid esters with sugar, vitamins and minerals. The authors Franco and Ulloa have reported the use of this plant in the medical area. In addition, the fruit is consumed in the form of juice, the leaves are used in the form of tea for different ailments. Considering that *Morinda citrifolia* has antioxidant properties, it is a good candidate to be studied as a green corrosion inhibitor. For this reason, it is of interest to obtain and characterise the organic compounds present in the extracts of its leaves, using solvents such as acetone and ethyl acetate in the extraction process.

Methodology

Preparation and obtaining the extracts

The leaves of *Morinda citrifolia* were collected at the main campus of the Universidad Autónoma del Carmen (see **Figure 1**). They were then rinsed with tap water, distilled water and drained for 1 hour. The leaves were then dried in a Hamilton Beach dehydrator at 60°C for 12 hr. At the end of this time, they were crushed in a Y series mill and sieved with an ELE International No. 60 sieve.

Box 1



Figure 1

Morinda citrifolia tree located on the main campus of the Universidad Autónoma del Carmen

Source: Own elaboration

Morinda citrifolia leaf extract was obtained by the maceration process. Acetone and ethyl acetate were used as solvent. Twenty-five g of leaf powder was used in 250 mL of solvent and the solution was left to stir for 72 hours. Subsequently, the extract was filtered and taken to the rotary evaporator at 60°C and 40 RPM. The concentrate obtained was placed in a convection oven at 60°C for 72 hours and finally the standard solution was prepared in 250 mL (see **Figure 2**).

Box 2

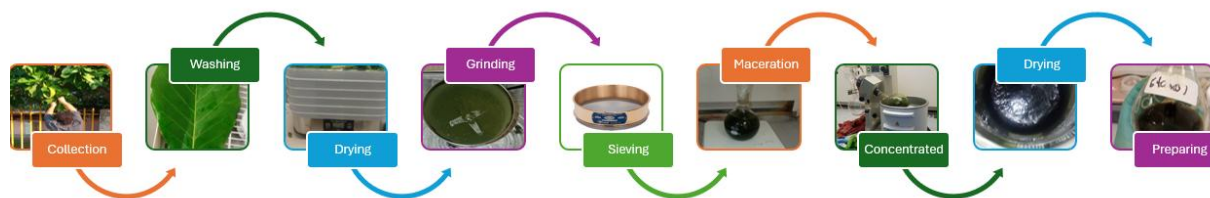


Figure 2

Obtaining and preparing *Morinda citrifolia* leaf extract

Source: *Own elaboration*

Characterisation of plant leaf extracts

The following techniques were used to identify the compounds contained in the *Morinda citrifolia* leaf extracts:

- Spectroscopic Techniques: The extracts were diluted in 10% water for subsequent measurement in UV-Vis spectrophotometer (HACH brand, model DR500). Measurements were made in the range of 200 to 800 nm. The samples were also measured in the FTIR spectrophotometer (Tensor II, Bruker brand) at a resolution of 4 cm^{-1} , 32 scans in the range 4000 to 500 cm^{-1} using a diamond-tipped ATR.
- Phytochemical tests: The methodologies proposed by the authors were used to identify flavonoids, saponins and tannins present in the extract. The phytochemical tests used were: Shinoda reaction and reaction with 10% NaOH (flavonoids), reaction with ferric chloride, reaction with grenetin and lead acetate reaction (tannins) and the foam test (saponins). Figure 3 shows some images obtained from the phytochemical tests performed on the extracts.

Box 3



Figure 3

Images of phytochemical tests

Source: *Own elaboration*

Results

In order to know the extraction percentage of the organic compounds contained in the leaves of the *Morinda citrifolia* plant, the yield (% R) of the extract with acetone and ethyl acetate was calculated using the following equation:

$$\% R = \frac{P_s}{P_i} \times 100 \quad [1]$$

Where: P_s is the weight of dry extract of *Morinda citrifolia* leaves (g) and P_i is the initial weight of leaves (g).

Table 1 shows the yields obtained with the two extracts. The extract with acetone had the highest yield. This means that the acetone extract was more efficient in extracting the compounds from the leaves of *Morinda Citrifolia citrifolia*.

Box 4

Table 1

Percentage yield values of *Morinda citrifolia* leaf extracts obtained with different solvents

Solvents	Dry extract (g)	% Performance
Acetone	3.60	14.4
Ethyl acetate	1.56	6.24

Source: own elaboration

Figure 4 shows the UV-VIS spectra obtained from the extract with acetone and ethyl acetate in the range from 200 to 800 nm. The spectrum corresponding to the extract with acetone presents two maximum peaks, the first at 236 nm which corresponds to flavonoids, since in this absorbance range the aromatic compounds are present and flavonoids belong to this group of chemical compounds. The peak at 420 nm and 674 nm is associated with anthocyanins, which belong to the group of flavonoids and provide the pigment (chlorophyll) to the leaves, flowers or fruits of plants. On the other hand, the response of the extract with ethyl acetate does not show the formation of a maximum peak. As can be seen, the solvent used in the extraction process has an effect on obtaining the components from the plant leaves.

Box 5

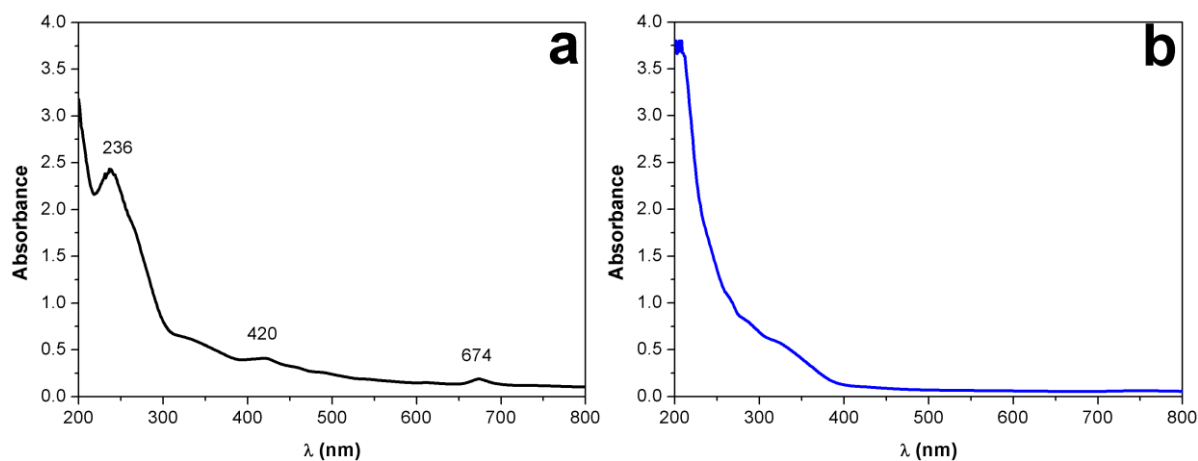


Figure 4

UV-Vis spectra obtained from (a) acetone and (b) ethyl acetate extract of *Morinda citrifolia* leaves

Source: Own elaboration

To identify the presence of organic compounds (secondary metabolites) in the extracts, the FTIR spectroscopy technique was used. **Figure 4** shows the FTIR spectra obtained from *Morinda Citrifolia* leaf extracts with different solvents in the range of 4000 to 500 cm^{-1} . In both cases, different adsorption peaks are observed. An adsorption peak is observed at 3325-3320 cm^{-1} and 1638 cm^{-1} , which can be associated with the O-H and C-H bond of the phenolic group. The stretching vibration of the C=O bond is also observed at 1613 cm^{-1} . In addition, the stretching peak at 1044-1019 cm^{-1} associated with the C-O bond is described

Box 6

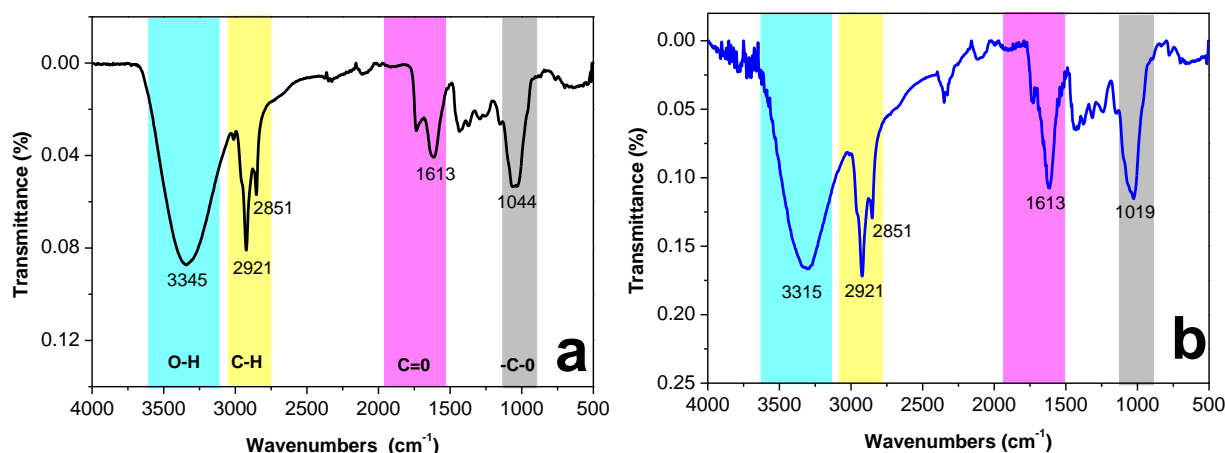


Figure 4

FTIR spectra obtained from (a) acetone and (b) ethyl acetate extract of *Morinda citrifolia* leaves

Source: Own elaboration

Table 2 shows the results obtained from the phytochemical tests used for the two extracts. It can be observed in both extracts the presence of tannins, saponins and flavonoids.

Box 7

Table 2

Results of phytochemical tests obtained with extracts of *Morinda citrifolia* leaves with different solvents

Phytochemicals/solvents	Colouring	Acetone	Ethyl acetate
Flavonoids	Yellow precipitate	-	-
Tannins	Light yellow	+	+
Saponins	N/A	+	+
Flavones	Light green	+	+
Tannins Catechol	Dark green	-	-

Source: own elaboration

Conclusions

Acetone is widely recognised as an effective solvent for extracting phytochemicals from plant materials, and offers several advantages as well as certain disadvantages. Its ability to produce high concentrations of bioactive compounds makes it a popular choice in phytochemical research. The acetonitrile extract is a better candidate for use as a corrosion inhibitor, because a greater variety of phytochemicals were identified compared to the other extracts. The absorbance of these extracts is higher because it contains more compounds absorbing in the UV-Vis spectrum (420 nm and 674 nm), although the phytochemical tests showed the same results compared to the ethyl acetate inhibitor, its UV-Vis spectrum showed more peaks.

Declarations

Conflict of interest

The authors declare that they have no conflicts of interest. They have no financial interests or personal relationships that could have influenced this book.

Authors' contribution

Sánchez Martínez, Víctor Alberto: Supported the experimental development and writing of the paper.

Figuroa Ramírez, Sandra Jazmín: Contributed to the analysis of the results.

Benavides, Olena: Reviewed the work.

Sierra Grajeda, Juan Manuel: Contributed to the review of the results.

Availability of data and materials

Data are available on request at: sfigueroa@pampano.unacar.mx

Funding

This research work was carried out with own resources.

Abbreviations

UV-Vis	Ultraviolet-visible
FTIR	Fourier Transform Infrared
ATR	Attenuated Total Reflectance

Acknowledgements

Victor Alberto Sánchez Martínez is grateful to CONAHACYT for the grant awarded to him for his doctoral studies. The authors would like to thank Dr. Beatriz Escobar Morales and M.C. Martín Bass López of the Centro de Investigación Científica de Yucatán (CICY) for their support with the spectroscopic techniques through the infrastructure project 2015-253986 and 2018-294697. Also, M.C. César Cima Mukul from the Centro de Excelencia de Investigación en Servicios Petroleros y Protección Ambiental (CEISPPA)-Facultad de Ingeniería de la UNACAR for providing the means to carry out the synthesis of the extract.

References

Background

Cárdenas Pinzón, L. K., & López Cárdenas, D. (2020). *Analysis of the Use of Inhibitors to Mitigate Internal Corrosion in Oil Formation Water Pipelines* [Thesis]. Fundación Universidad de América.

Franco, M., Herrera-Hernández, H., García-Orozco, I., & Herrasti, P. (2018). Natural aqueous extract of *Morinda Citrifolia* as a corrosion inhibitor of AISI-1045 steel in acidic HCl environments. *Journal of Metallurgy*, 54(4).

Madu, J. O., Ifeakachukwu, C., Okorodudu, U., Adams, F. V., & Joseph, I. V. (2019). Corrosion Inhibition Efficiency of Terminalia Catappa Leaves Extracts on Stainless Steel in Hydrochloric Acid. *Journal of Physics: Conference Series*, 1378(2).

Razafimandimbison, S. G., McDowell, T. D., Halford, D. A., & Bremer, B. (2010). Origin of the pantropical and nutraceutical *Morinda citrifolia* L. (Rubiaceae): Comments on its distribution range and circumscription. *Journal of Biogeography*, 37(3), 520-529.

Royani, A., Hanafi, M., Haldhar, R., & Manaf, A. (2024). Evaluation of *Morinda citrifolia* extract as sustainable inhibitor for mild steel in saline environment. *Journal of Engineering Research (Kuwait)*.

Ulloa, J. A., Rosas Ulloa, P., Carmen Ramírez Ramírez, J., Estela, B., & Rangel, U. (2012). Noni: properties, uses and potential applications. In *Revista Fuente Año* (Vol. 4, Issue 10). ISSN: 2007-7521.

Basics

C, R. U., & Mala Nair, V. (2013). Phytochemical analysis of successive reextracts of the leaves of moringa ISSN- 0975-1491. oleifera lam.

Royani, A., Hanafi, M., Haldhar, R., & Manaf, A. (2024). Evaluation of *Morinda citrifolia* extract as sustainable inhibitor for mild steel in saline environment. *Journal of Engineering Research (Kuwait)*.

Shaibu Auwal, M., Saka, S., Alhaji Mairiga, I., Abba Sanda, K., Shuaibu, A., Ibrahim, A., & Shaibu Auwal DVM, M. (2014). [Preliminary phytochemical and elemental analysis of aqueous and fractionated pod extracts of *Acacia nilotica* \(Thorn mimosa\)](#). In *ARTICLE Veterinary Research Forum* (Vol. 5, Issue 2).

Support

Benítez-Benítez, R., Sarria-Villa, R. A., Gallo-Corredor, J. A., Pérez Pacheco, N. O., Álvarez Sandoval, J. H., & Giraldo Aristizabal, C. I. (2020). [Obtaining and yield of ethanolic extract of two medicinal plants](#). *Revista Facultad de Ciencias Básicas*, 15(1), 31-40.




Fleming, I., & Williams, D. (2019). [Ultraviolet and Visible Spectra](#). In *Spectroscopic Methods in Organic Chemistry* (pp. 55-83). Springer International Publishing.




Mamudu, U., Santos, J. H., Umoren, S. A., Alnarabiji, M. S., & Lim, R. C. (2024). [Investigations of corrosion inhibition of ethanolic extract of *Dillenia suffruticosa* leaves as a green corrosion inhibitor of mild steel in hydrochloric acid medium](#). *Corrosion Communications*, 15, 52-62.




DFT study on the interaction between carbon dioxide and doped fullerene C₃₀




Estudio computacional de la interacción entre dióxido de carbono y fullereno C₃₀ dopado

Toxqui-De La Torre, Ana Paulina^{*a}, Mandujano-Ramirez, Humberto Julián^b, Martinez-Vargas, Sergio^c and Patiño-Carachure, Cristóbal^d

^a  Universidad Autónoma del Carmen •  0009-0002-1103-2406 •  1322390

^b  Universidad Autónoma del Carmen •  0000-0003-3714-5564 •  266189

^c  Universidad Autónoma del Carmen •  0000-0002-2499-3970 •  100782

^d  Universidad Autónoma del Carmen •  0000-0002-1436-1259 •  226327

CONAHCYT classification:

DOI: <https://doi.org/10.35429/H.2024.14.9.18>

Area: Engineering

Field: Engineering

Discipline: Materials Science and Technology

Subdiscipline: Materials Properties

Key Handbooks

The main contribution of this research involves the computational study of the nanostructure of Boron and Nitrogen doped C₃₀ fullerene. Evaluating its adsorption energy, using density functional theory (DFT), by means of the PBE functional and the 6-31G(d,p) basis set. This study also obtains the HOMO and LUMO of each optimised doped nanostructure, as these can be used to determine the applications of a nanomaterial in both optical and electronic devices. The different doping sites influence the nanostructure of the fullerene, and see how it reacts with two family groups of different elements, and its adsorption energy in each of its doped and optimised nanostructures and how its geometric shape changes once it has been calculated. The adsorption energy of C₃₀ and C₂₉X (X=B, N) in the presence of CO₂ indicates that the doping site with some element is relevant in the optimisation process.

Citation: Toxqui-De La Torre, Ana Paulina, Mandujano-Ramirez, Humberto Julián, Martinez-Vargas, Sergio and Patiño-Carachure, Cristóbal. 2024. DFT study on the interaction between carbon dioxide and doped fullerene C₃₀. 9-18. ECORFAN.

* ✉ (153508@mail.unacar.mx)

Handbook shelf URL: <https://www.ecorfan.org/handbooks.php>



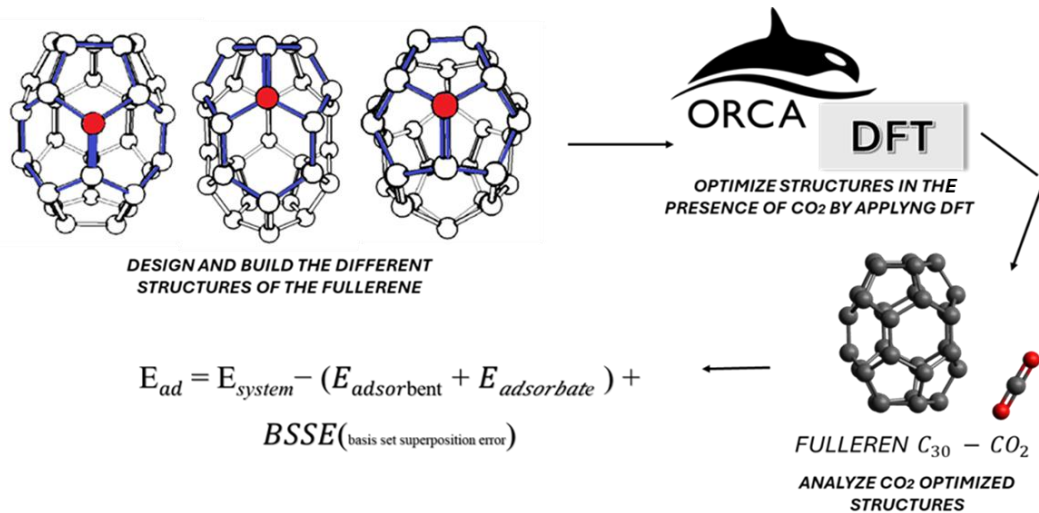
ISBN 978-607-8948-50-5/©2009 The Authors. Published by ECORFAN-Mexico, S.C. for its Holding Mexico on behalf of Handbook HRP. This is an open access chapter under the CC BY-NC-ND license [<http://creativecommons.org/licenses/by-nc-nd/4.0/>]

Peer Review under the responsibility of the Scientific Committee **MARVID**[®] in contribution to the scientific, technological and innovation Peer Review Process by training Human Resources for the continuity in the Critical Analysis of International Research.



Abstract

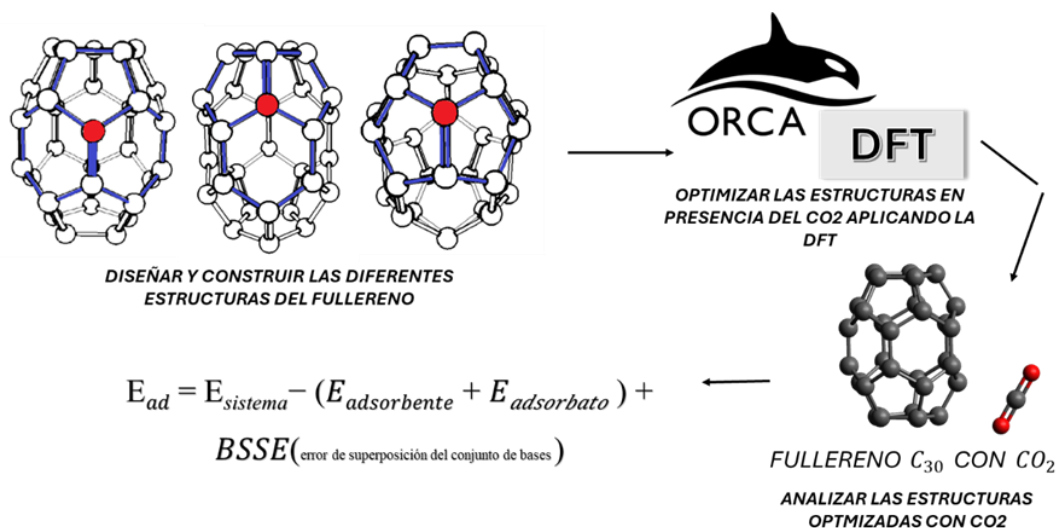
Fullerenes are symmetrical carbon nanostructures zero dimensional with hybridation sp^2 -bonded carbon atoms (with four valence electrons) arranged in pentagonal and hexagonal rings that form a hollow closed-cage structure. Fullerene C_{30} is not symmetrical, specifically has 12 pentagonal and 5 hexagonal rings that form a barrel-like shape where the 5 hexagons form the body of the barrel, and the 12 pentagons are located in the bases of the barrel. Doped fullerenes were built by placing a heteroatom (as a boron or a nitrogen atom, with three or five valence electrons, respectively) at different doping sites. Doped fullerenes were optimized in presence of CO_2 using density functional theory (DFT) through PBE functional and 6-31G(d,p) basis set. The CO_2 adsorption energy on doped fullerenes were determined.



Fullerene doped, Carbon nanostructure, Adsorption energy

Resumen

Los fullerenos son nanoestructuras de carbono simétricas de dimensión cero con átomos de carbono de enlace sp^2 de hibridación (con cuatro electrones de valencia) dispuestos en anillos pentagonales y hexagonales que forman una estructura hueca de jaula cerrada. El fullereno C_{30} no es específicamente simétrico tiene 12 anillos pentagonales y 5 hexagonales que forman una forma parecida a un barril donde los 5 hexágonos son el cuerpo del barril y los 12 pentágonos están situados en las bases del barril. Los fullerenos dopados se construyeron colocando un heteroátomo (como un átomo de boro o de nitrógeno, con tres o cinco electrones de valencia, respectivamente) en diferentes sitios de dopaje. Los fullerenos dopados se optimizaron en presencia de CO_2 utilizando la teoría funcional de la densidad (DFT) mediante el funcional PBE y el conjunto de bases 6-31G(d,p). Se determinó la energía de adsorción de CO_2 en los fullerenos dopados.



Fullereno dopado, Nanoestructura de carbono, Energía de adsorción

Introduction

One of the materials that is of considerable interest at present is buckminsterfuller or better known as fullerene. C_{60} (fullerene) is a mainstay of research due to its physicochemical properties, making it the most studied fullerene. These characteristics make it particularly suitable for exploration in the fields of materials science and engineering.

In fullerenes there are σ bonds, formed by overlapping, where the electron density is concentrated between the nuclei of the atoms, and π bonds, resulting from the lateral overlapping of the orbitals, with the electron density distributed above and below the plane of the nuclei linked at the front of the orbitals. For this reason, fullerenes have a spherical shape called Bucky sphere (Tománek David, 2014). There is a greater diversity of fullerene structures, but not all of them have a spherical structure, such as C_{30} , which is smaller in size (Tománek David, 2014). (ver fig. 1).

Box 1

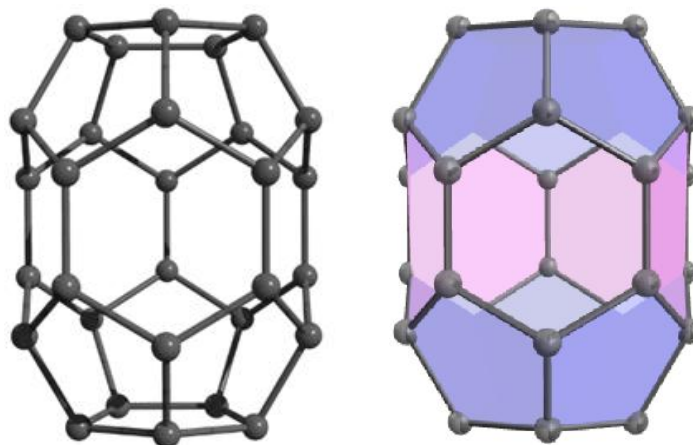


Figure 1

Modelling of the structure of C_{30} fullerene which is made up of 12 pentagons and 5 hexagons

Source: Own elaboration

Smaller fullerenes currently have more impact in the scientific literature due to their high potential in the development of advanced applications in key areas of nanotechnology and theoretical chemistry, and are an area of interest for the study of their properties and possible applications.

On the other hand, CO_2 adsorption on fullerenes is a very important area of study at present. Previously, adsorption of toxic gases has been studied with carbon nanostructures; nanotubes, graphene etc.

Most of the work reported in the scientific literature on doped fullerenes uses Density *Functional Theory* (DFT). DFT is a theory widely used to study molecular systems, nanostructures, solids and surfaces by solving approximate versions of the Schrödinger equation. Its origin dates back to an article by Hohenberg and Kohn in 1964 in *Physical Review*, entitled ‘Inhomogeneous Electron Gas’. Its methodology is used in a variety of fields and problems, with the study of electronic structure in the ground state being one of the most common. In this work, CO_2 adsorption on C_{30} and $C_{29}X$ ($X = B, N$) fullerenes at different doping sites was studied to obtain its adsorption energy (E_{Ad}), including the basis set error correction (BSSE).

Methodology

Design and construction of the different molecular structures

The fullerene structures were designed by constructing a barrel composed of carbon atoms, with single and double bonds. Unlike a common fullerene which has a spherical shape, C_{30} is composed of 12 pentagons and 5 hexagons.

The design has been made by forming the C_{30} fullerene structures, then replacing a carbon atom at different doping sites (*see fig. 2*) with Boron and Nitrogen to form the $C_{29}B$ and $C_{29}N$ structure. The CO_2 molecule was also constructed and each of them was optimised with the PBE functional, with the 6-31G(d,p) basis set.

Box 2

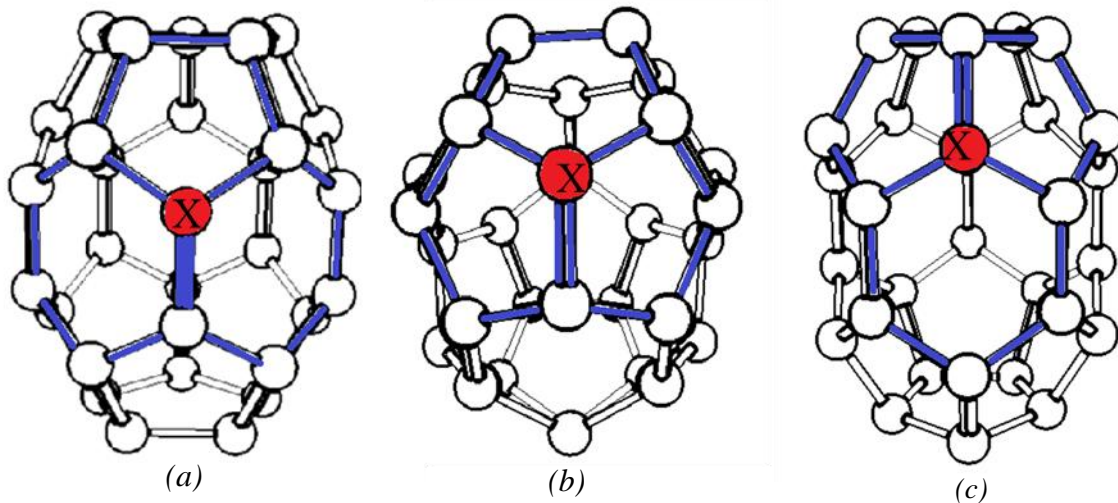


Figure 2

Doping sites. Element X is: (a) surrounded by 2 hexagonal rings and a pentagonal ring (PHH), (b) surrounded by three pentagonal rings (PPP) and (c) surrounded by 2 pentagonal rings and a hexagonal ring (PPH)

Source: *Own elaboration*

Optimisation of the structures in the presence of CO_2 by applying DFT.

The calculations were performed using ORCA 4.2.1 (Neese, F. 2022), as a first step the optimisation of the designed structures of C_{30} and $C_{29}X$ ($X = B, N$) was performed to determine the minimum energy of the most stable geometries, then the minimum energy of the interaction of the fullerenes with CO_2 was calculated, finally the adsorption energy was calculated. Figure 3 shows the optimised structure and the optimised structure with CO_2 .

Box 3

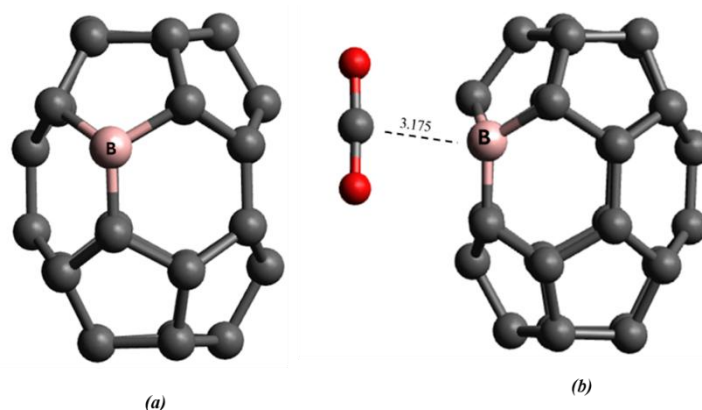


Figure 3

Optimised structure of boron-doped C_{30} fullerene (a)
Optimised structure of CO_2 -doped $C_{29}B$ (b)

Source: *Own elaboration*

The adsorption energies are calculated with the following equation. (Kahn, Ahmad, et al., 2021)

$$E_{Ad} = E_{sistema} - (E_{adsorbente} + E_{adsorbato}) + BSSE \quad [1]$$

Where ($E_{sistema}$) is the system energy of the system corresponding to the minimum energy of the interaction of the C_{30} ó $C_{29}X$ ($X=B, N$) With the CO_2 , ($E_{adsorbente}$) is the adsorbent energy which corresponds to the basal state energy of the adsorbent. C_{30} y $C_{29}X$ ($X= B, N$), ($E_{adsorbato}$) is the minimum energy of the molecule of the CO_2 .

The term BSSE is the basis set superposition error, this calculation arises from molecular interactions. The calculation of the BSSE is of utmost importance because during the molecular interaction there are variations in the energy of each molecule due to the superposition of the wave functions of each molecule (Boys & Bernardi, 1970). We used the BSSE calculation methodology implemented in the ORCA software to calculate the interaction energy of C_{30} , $C_{29}X$ ($X=B, N$) and CO_2 which is obtained by the following equation:

$$BSSE = [E_{C_{30}}^{C_{30}-CO_2}(C_{30}) + E_{CO_2}^{C_{30}-CO_2}(CO_2)] - [E_{C_{30}}^{C_{30}-CO_2}(C_{30} - CO_2) + E_{CO_2}^{C_{30}-CO_2}(C_{30}-CO_2)] \quad [2]$$

Where, $E_{C_{30}}^{C_{30}-CO_2}(C_{30})$ is the energy of the C_{30} , obtained from the geometrical optimisation of the system $C_{30}-CO_2$ calculated on the basis of C_{30} , $E_{CO_2}^{C_{30}-CO_2}(CO_2)$ is the energy of the CO_2 , obtained from the geometrical optimisation of the system $C_{30}-CO_2$, calculated on the basis of CO_2 , $E_{C_{30}}^{C_{30}-CO_2}(C_{30} - CO_2)$ is the energy of the CO_2 obtained from the geometrical optimisation of the system $C_{30}-CO_2$ y $E_{CO_2}^{C_{30}-CO_2}(C_{30}-CO_2)$ is the energy of the CO_2 calculated from the optimisation of the system $C_{30}-CO_2$ obtained from the base of $C_{30}-CO_2$. Similarly, the basis set superposition error (BSSE) is computed for $C_{29}B-CO_2$ and $C_{29}N-CO_2$

Finally, the band gap energy is calculated from the energy of the highest occupied molecular orbital (*HOMO*) and the energy of the lowest unoccupied molecular orbital (*LUMO*).

Results

Minimum energies of C_{30} , $C_{29}X$ ($X=B, N$) interacting with CO_2

Table | shows the minimum energies of each of the C_{30} , $C_{29}X$ ($X=B, N$) structures interacting with CO_2 at different doping sites. Observing that the minimum energies at the different doping sites vary for each structure.

Box 4

Table 1

Doping sites and minimum energy of each of the systems C_{30} y $C_{29}X$ ($X=B, N$)

DOPING SITES	$C_{29}X-CO_2$	SYSTEM ENERGY (eV)
PHH	$C_{30}-CO_2$	-1329.69006
	$C_{29}B-CO_2$	-1316.562063
	$C_{29}N-CO_2$	-1346.407651
PPH	$C_{30}-CO_2$	-1329.690815
	$C_{29}B-CO_2$	-1316.584383
	$C_{29}N-CO_2$	-1346.427076
PPP	$C_{30}-CO_2$	-1329.689821
	$C_{29}B-CO_2$	-1316.584383
	$C_{29}N-CO_2$	-1346.432648

Source: Own elaboration

System $C_{30}-CO_2$

The energy of the $C_{30}-CO_0-CO_2$ system was calculated after optimisation. Figure 4 shows its adsorption energy at the doping sites from lowest to highest; two pentagonal rings and one hexagonal ring (*PPH*), two hexagonal rings and one pentagonal ring (*PHH*), three pentagonal rings (*PPP*). Observing that as the adsorption energy becomes more negative, the distance to the CO_2 molecule becomes shorter. This behaviour has an impact on the doping site.

Box 5

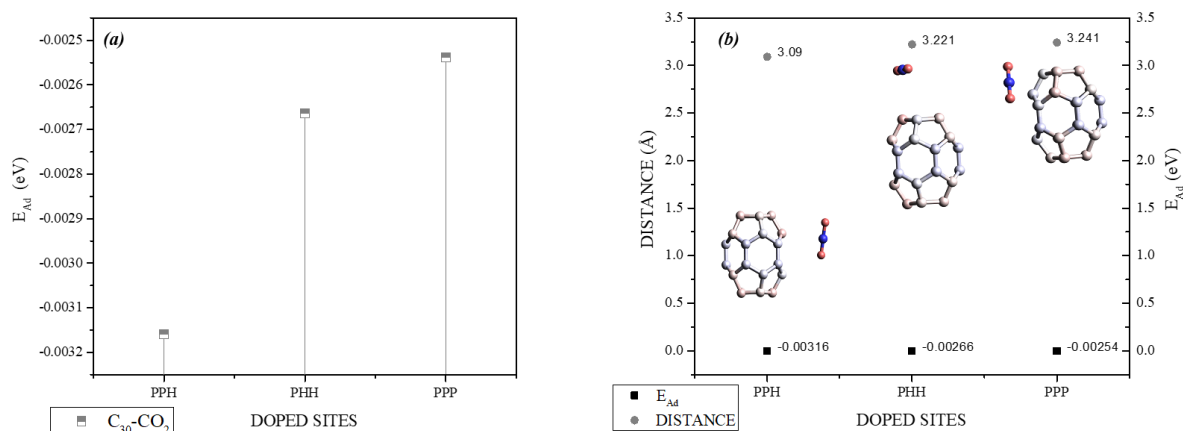


Figure 4

System $C_{30}-CO_2$: Adsorption energy (a), Ratio of adsorption energy to distance (b)

Source: *Own elaboration*

Table 2 presents the adsorption energy (E_{Ad}), the BSSE superposition error, the HOMO energy, the LUMO energy and the energy of the forbidden band (E_{Gap}).

Box 6

Table 2

system variables $C_{30}-CO_2$

DOPING SITES	$C_{29}X-CO_2$ (eV)	E_{Ad} TOTAL (eV)	BSSE (eV)	HOMO (eV)	LUMO (eV)	E_{gap} (eV)
PPH	$C_{30}-CO_2$	-0.003159	0.002494	-4.669	-4.236	0.433
PHH	$C_{30}-CO_2$	-0.002664	0.002234	-4.673	-4.244	0.429
PPP	$C_{30}-CO_2$	-0.0025384	0.002121	-4.686	-4.244	0.442

Source: *Own elaboration*

In the fullerene C_{30} , Carbon atoms have sp^2 hybridisation, which allows the formation of molecular orbitals that are distributed throughout the structure. According to band theory, the electrons in these orbitals move freely within bands formed by the overlap of these orbitals. The bonding molecular orbitals contribute to the formation of the conduction band. In materials such as metals, the valence band and conduction band can overlap, facilitating electrical conduction. In other materials, the separation between these bands is marked by a band gap, which limits electrical conductivity.

Figure 5 shows the optimised HOMO and LUMO boundary orbitals for the $C_{30}-CO_2$ system, which is related to Fukui's theory, plays a fundamental role in determining the chemical reactivity of a molecule in interaction with other molecules. The energy difference between the HOMO and LUMO, known as the HOMO-LUMO gap, corresponds to the lowest excitation energy. In the boundary orbitals, two regions with opposite signs are displayed in the wave function: a positive phase (shown in blue) and a negative phase (shown in red). These phases correspond to the electron density distribution in the molecules, where the colours indicate the alternating signs of the wave function.

Box 7

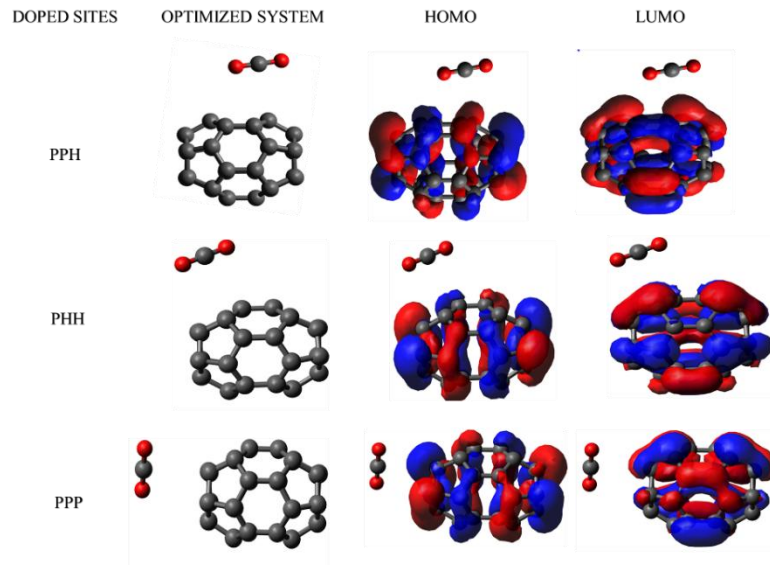


Figure 5

HOMO and LUMO boundary orbitals of the C₃₀-CO₂ system at different doping sites

Source: *Own elaboration*

System C₂₉B-CO₂ and C₂₉N-CO₂

The system was calculated C₂₉B-CO₂ and C₂₉N-CO₂ after optimisation. In figure 3.3, it shows the adsorption energy of C₂₉B and CO₂, reflecting a lower to higher adsorption energy with respect to the doping sites; double pentagon ring and a hexagon ring (PPH), triple pentagon ring (PPP), double hexagon ring and a pentagonal ring (PHH). The relationship between distance and adsorption energy of the C₂₉B-CO₂ system. A carbon bond of the CO₂-doped fullerene structure is observed at the PPH doping site.

Box 8

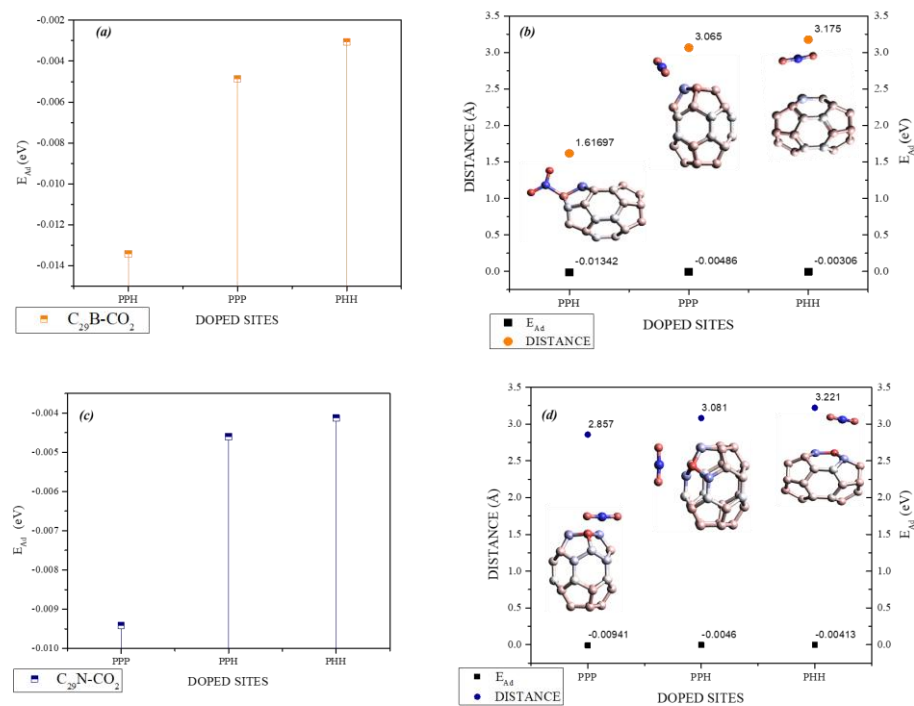


Figure 6

System C₂₉B-CO₂: Adsorption energy (a), Adsorption energy and distance ratio (b).
System C₂₉N-CO₂: Adsorption energy (c), Adsorption energy and distance ratio (d).

Source: *Own elaboration*

In the $C_{29}N-CO_2$ system, the interaction of $C_{29}N$ and CO_2 is shown, reflecting a lower to higher adsorption energy with respect to the doping sites; triple pentagon ring (*PPH*), triple pentagon ring (*PPP*), double hexagonal ring and a pentagonal ring (*PHH*). (see figure 6). The relationship between distance interaction and adsorption energy of the $C_{29}N$ and CO_2 system decreases, but at different doping site compared to the $C_{29}B-CO_2$ system in figure 3.3 (see figure 6). Table 3 presents the results obtained for the $C_{29}B-CO_2$ and $C_{29}N-CO_2$ systems: Adsorption Energy, HOMO, LUMO and E_{gap} (energy gap between HOMO and LUMO). These variables have been calculated for the optimised systems at their different doping sites.

Box 9

Table 3.3

System variables $C_{29}B-CO_2$ y $C_{29}N-CO_2$

DOPING SITES	$C_{29}X-CO_2$	E_{Ad} TOTAL (eV)	BSSE (eV)	HOMO (eV)	LUMO (eV)	E_{gap} (eV)
PHH	$C_{29}B-CO_2$	-0.003060846	0.002283154	-0.584	-0.083	0.501
	$C_{29}N-CO_2$	-0.004128	0.002689	-0.594	-0.112	0.482
PPH	$C_{29}B-CO_2$	-0.013416	0.007284	-1.374	-0.887	0.487
	$C_{29}N-CO_2$	-0.004601	0.003458	-0.626	-0.081	0.545
PPP	$C_{29}B-CO_2$	-0.004862	0.003166	-0.593	-0.096	0.497
	$C_{29}N-CO_2$	-0.009413	0.003001	-0.568	-0.109	0.459

Source: Own elaboration

Figure 7 shows the optimised geometry of each of the systems, showing the distributions of the HOMO and LUMO orbitals corresponding to each doped structure.

Box 10

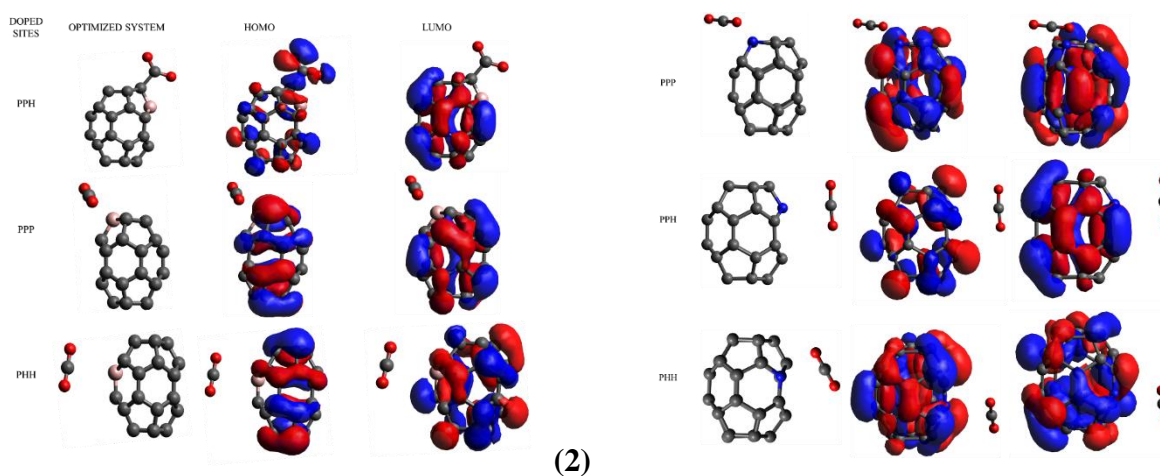


Figure 7

HOMO and LUMO boundary orbitals of the $C_{29}B-CO_2$ system at different doping sites (1)
HOMO and LUMO boundary orbitals of the $C_{29}N-CO_2$ system at different doping sites (2)

Source: Own elaboration

Conclusions

The results obtained for the adsorption energy of C_{30} and $C_{29}X$ ($X=B, N$) in the presence of CO_2 indicate that the doping site with some element has an impact on the optimisation process. However, it was observed that depending on the family group to which the element belongs, the doping site and its properties will not always be in the same order for all of them. These are due to the electronegativity, atomic size and orbital properties of the elements, which affect both the polarity and charge distribution in the system, thus modifying the CO_2 adsorption capacity in the molecular structure.

Declarations

Conflict of interest

The authors declare that they have no conflicts of interest. They have no financial interests or personal relationships that could have influenced this book.

Authors' contribution

Toxqui-De La Torre, Ana Paulina: Drafting, data analysis, figure production.

Mandujano-Ramirez, Humberto Julián: Proofreading, editing, revising results and proofreading.

Martinez-Vargas, Sergio: Spelling check, editing, proofreading, proofreading, output review and correction.

Patiño-Carachure, Cristóbal: Proofreading and editing.

Availability of data and materials

The information contained in this document is not available, prior to the data being worked on.

Funding

No funding was received.

Acknowledgements

I thank the core of the Master in Materials and Energy Engineering and my Drs. for supporting me in this research work, as well as the support received from CONAHCYT to continue contributing to the advancement of science and technology in our country.

Abbreviations

DFT	DENSITY FUNCTIONAL
GAP	THEORY BANDGAP
HOMO	HIGHEST OCCUPIED MOLECULAR
LUMO	LOWEST UNOCCUPIED MOLECULAR ORBITAL

References

Background

Adjizian, J. J., Vlandas, A., Rio, J., Charlier, J. C., & Ewels, C. P. (2016). [Ab initio infrared vibrational modes for neutral and charged small fullerenes \(C20, C24, C26, C28, C30 and C60\)](#). *Philosophical Transactions of the Royal Society A: Mathematical, Physical and Engineering Sciences*, 374(2076).

Baei, M. T., Koochi, M., & Shariati, M. (2018). [Structure, stability, and electronic properties of AIP nanocages evolved from the world's smallest caged fullerene C20: A computational study at DFT](#). *Journal of Molecular Structure*, 1159, 118–134.

Bhakta, P., & Barthunia, B. (2020). [Fullerene and its applications: A review](#). *Journal of Indian Academy of Oral Medicine and Radiology*, 32(2), 159.

Fekri, M. H., Bazvand, R., Solymani, M., & Mehr, M. R. (2020). [Adsorption Behavior, Electronical and Thermodynamic Properties of Ornidazole Drug on C60 Fullerene Doped with Si, B and Al: A Quantum Mechanical Simulation](#). *Physical Chemistry Research*, 9(1), 151–164.

Grądzka, E., Wysocka-Żołopa, M., & Winkler, K. (2020). [Fullerene-Based Conducting Polymers: n - Dopable Materials for Charge Storage Application](#). *Advanced Energy Materials*, 10(40).

- Hasanah, D., . W., Mulyani, S., & Widhiyanti, T. (2024). [Multiple Representations Analysis of Chemical Bonding Concepts in General Chemistry Books](#). KnE Social Sciences.
- Paul, D., Mane, P., Sarkar, U., & Chakraborty, B. (2023). [Yttrium decorated fullerene C30 as potential hydrogen storage material: Perspectives from DFT simulations](#).
- Shetti, N. P., Mishra, A., Basu, S., & Aminabhavi, T. M. (2021). [Versatile fullerenes as sensor materials](#). In *Materials Today Chemistry* (Vol. 20). Elsevier Ltd.
- Tománek, D. (2014). [Guide Through the Nanocarbon Jungle](#). Morgan & Claypool Publishers.
- Yang, Y., Sun, A., & Gu, W. (2021). [Sensing behavior of pristine and doped C70 fullerenes to mercaptopurine drug: a DFT/TDDFT investigation](#). *Structural Chemistry*, 32(1), 457–468.

Basics

- Apebende, C. G., Ogunwale, G. J., Louis, H., Benjamin, I., Kadiri, M. T., Owen, A. E., & Manicum, A.-L. E. (2023). [Density functional theory \(DFT\) computation of pristine and metal-doped MC59 \(M = Au, Hf, Hg, Ir\) fullerenes as nitrosourea drug delivery systems](#). *Materials Science in Semiconductor Processing*, 158, 107362.
- Babu, D. J., Bruns, M., Schneider, R., Gerthsen, D., & Schneider, J. J. (2017). [Understanding the influence of N-doping on the CO₂ adsorption characteristics in carbon nanomaterials](#). *Journal of Physical Chemistry C*, 121(1), 616–626.
- Bai, H., Ji, W., Liu, X., Wang, L., Yuan, N., & Ji, Y. (2013). [Doping the buckminsterfullerene by substitution: Density functional theory studies of C59X \(X = B, N, Al, Si, P, Ga, Ge, and As\)](#). *Journal of Chemistry*.
- Canales, M., Ramírez-de-Arellano, J. M., & Magana, L. F. (2016). [Interaction of a Ti-doped semi-fullerene \(TiC30\) with molecules of CO and CO₂](#). *Journal of Molecular Modeling*, 22(9).
- Giustino, F. (2014). *Materials modelling using density functional theory: properties and predictions*. Oxford University Press.
- Harismah, K., Hassan, A., Nassar, M. F., Hamid, O. T., & Zandi, H. (2023). [Carbon Dioxide Uptake by a Polonium-Doped Fullerene: Computational Analyses](#). *Biointerface Research in Applied Chemistry*, 13(5).
- Khan, A. A., Ahmad, R., Ahmad, I., & Su, X. (2021). [Selective adsorption of CO₂ from gas mixture by P-decorated C24N24 fullerene assisted by an electric field: A DFT approach](#). *Journal of Molecular Graphics and Modelling*, 103.

Support




- Boys, S. F., & Bernardi, F. (1970). [The calculation of small molecular interactions by the differences of separate total energies](#). Some procedures with reduced errors. *Molecular Physics*, 19(4), 553–566.
- Burke, K. (2007). [The ABC of DFT](#).
- Neese, F. (2018). [Software update: the ORCA program system, version 4.0](#). *WIREs Computational Molecular Science*, 8(1).
- Khan, A. A., Ahmad, R., Ahmad, I., & Su, X. (2021). [Selective adsorption of CO₂ from gas mixture by P-decorated C24N24 fullerene assisted by an electric field: A DFT approach](#). *Journal of Molecular Graphics and Modelling*, 103.
- Seeman, J. I. (2022). [Kenichi Fukui, Frontier Molecular Orbital Theory, and the Woodward-Hoffmann Rules. Part III. Fukui's Science and Technology, 1918–1965†*](#). *The Chemical Record*, 22(4).

Analysis of the mechanism of formation and growth of carbon nanostructures produced through the mechanical milling of graphite





Análisis del mecanismo de formación y crecimiento de nanoestructuras de carbono obtenidas por molienda mecánica de grafito

Aguilar-Cruz, Felix^a, Flores-Gil, Aaron^b, Álvarez-García, Emilio^c and Patiño-Carachure, Cristóbal*^d

^a  Universidad Autónoma del Carmen •  0009-0004-5488-4240 •  767614

^b  Universidad Autónoma del Carmen •  0000-0002-2302-2056 •  121166

^c  Universidad Tecnológica de Campeche •  LRC-9320-2024 •  0000-0002-8046-0124

^d  Universidad Autónoma del Carmen •  AGZ-9935-2022 •  0000-0002-1436-1259 •  226327

CONAHCYT classification:

DOI: <https://doi.org/10.35429/H.2024.14.19.26>

Area: Engineering

Field: Engineering

Discipline: Chemical engineering

Sub-discipline: Materials science

Key Handbooks

The research presented here contributes significantly to the field of nanotechnology by offering a simple and versatile method for the production of carbon nanostructures. This chapter compares two mechanisms for the formation of carbon nanostructures, both using mechanical milling (MM) and heat treatment (HT). X-ray diffraction (XRD), Raman spectroscopy and high-resolution transmission electron microscopy (HRTEM) characterisation techniques were employed. By varying the milling times of crystalline graphite with AlCuFe quasicrystals and amorphous graphite, nanostructures are defined as the milling time increases. The quasicrystal acts as an accelerating agent in the reduction of the crystal size during the process and often assists in the generation of carbon nanostructures. Heat treatment between 200 °C and 450 °C best defines onion-type nanostructures (nano-onions) and curved rolls.

Citation: Aguilar-Cruz, Felix, Flores-Gil, Aaron, Álvarez-García, Emilio, Patiño-Carachure, Cristóbal. 2024. Analysis of the mechanism of formation and growth of carbon nanostructures produced through the mechanical milling of graphite. 19-26. ECORFAN.

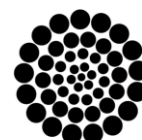
* ✉ [cpatino@pampano.unacar.mx]

Handbook shelf URL: <https://www.ecorfan.org/handbooks.php>



ISBN 978-607-8948-50-5/©2009 The Authors. Published by ECORFAN-Mexico, S.C. for its Holding Mexico on behalf of Handbook HRP. This is an open access chapter under the CC BY-NC-ND license [<http://creativecommons.org/licenses/by-nc-nd/4.0/>]

Peer Review under the responsibility of the Scientific Committee MARVID®- in contribution to the scientific, technological and innovation Peer Review Process by training Human Resources for the continuity in the Critical Analysis of International Research.





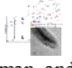
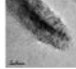
RENIECYT

Registro Nacional de Instituciones y
Empresas Científicas y Tecnológicas

1702902 CONAHCYT

Abstract

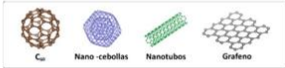

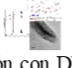

A microstructural analysis was conducted to investigate the formation mechanism of carbon nanostructures produced through mechanical milling crystalline and amorphous graphite, followed by thermal treatments at various temperatures. A unidirectional ball mill operating at 1700 rpm was employed for the synthesis. Different milling times (3, 6, and 12 hours) and heat treatments were used at 200 °C, 300 °C, and 450 °C. Results obtained by X-ray diffraction, Raman spectroscopy, and high-resolution transmission electron microscopy revealed the formation of curved concentric nuclei composed of carbon layers for milling times of 6 and 12 hours. The thermal treatment at 450°C promoted the growth and definition of carbon nano-onions.

Analysis of the mechanism of formation and growth of carbon nanostructures produced through the mechanical milling of graphite		
Objectives	Methodology	Contribution
 <p>Study the growth of carbon nanostructures through thermal processing.</p>	 <p>Crystalline graphite with quasicrystals and amorphous graphite are subjected to different milling times and temperatures.</p>  <p>XRD, Raman, and HRTEM characterization.</p>	<p>$Al_{64}Cu_{24}Fe_{12}$</p> <p>The quasicrystal acts as an accelerator in the creation of nanostructures.</p>  <p>Applying TT between 200°C and 450°C helps to better define the nanostructures.</p>

Microstructural, nanostructures, synthesis

Resumen

Se realizó el análisis microestructural del mecanismo de formación de nanoestructuras de carbono obtenidas por molienda mecánica de grafito cristalino y amorfo, las cuales fueron crecidas por tratamiento térmico a diferentes temperaturas. Para la síntesis de nanoestructuras de carbono se empleó un molino mecánico unidireccional que oscila a 1700 rpm. Las variables de experimentación fueron los diferentes tiempos de molienda (3, 6 y 12 h) y los tratamientos térmicos a 200 °C, 300 °C y 450 °C. Las técnicas de caracterización de difracción de rayos X, espectroscopía Raman y la microscopía electrónica de transmisión de alta resolución indican la formación de núcleos concéntricos curvados de láminas de carbono para tiempos de molienda de 6 y 12 h. Con el tratamiento térmico a 450 o C se apreció un crecimiento y definición de nano-onions de carbono (nanocebollas).

Análisis del mecanismo de formación y crecimiento de nanoestructuras de carbono obtenidas por molienda mecánica de grafito		
Objetivos	Metodología	Contribución
 <p>Determinar el crecimiento de nanoestructuras de carbono al aplicar tratamiento térmico.</p>	 <p>Se someten grafito cristalino con cuasicristales y grafito amorfo a distintos tiempos de molienda y temperaturas.</p>  <p>Caracterización con DRX, Raman y HRTEM.</p>	<p>$Al_{64}Cu_{24}Fe_{12}$</p> <p>El cuasicristal actúa como un acelerador en la creación de las nanoestructuras</p>  <p>Aplicar TT a 200 °C a 450 °C logra definir mejor las nanoestructuras</p>

Microestructural, nanoestructuras, síntesis

Introduction

Since the discoveries of fullerenes, carbon nanotubes, graphene and other allotropic forms of carbon, the search for an increasingly simple and economically viable process has been a challenge for science today. The synthesis of carbon nanostructures by mechanical methods has been novel in recent years because of its versatility and ease of designing mechanical mills at different speeds. High-energy ball milling (spex milling) of graphite in an air atmosphere leads to forming time-dependent carbon nanostructures through mechanical deformation (Patiño et al. 2020). Mechanical crushing facilitates the synthesis of carbon nanostructures and inducing high temperatures with controlled atmospheres enables gas-phase reactions that produce unique shapes such as carbon nanotubes and carbon nanobeads. (Satoshi et al. 2011).

Heat treatment significantly influences the properties and performance of carbon nanostructures, improving their properties. Several studies show that heat treatment can improve the structural uniformity and overall performance of carbon nanomaterials (Carneiro and Simões, 2021; Villacorta et al. 2013; Srikanth et al. 2016).

Therefore, in this research the formation of carbon nanostructures from the mechanical milling of crystalline and amorphous graphite is exposed, employing a unidirectional mill where, subsequently, from this process, a heat treatment is applied.

Methodology

Hexagonal and amorphous graphite powders were subjected to mechanical deformation by high energy mechanical milling. The mill comprises a one-way oscillating mechanical system connected to a Siemens electric motor (1750 rpm at a speed of 5 m/s). The operation varies according to the time and ratio between the balls and the sample's weights, as shown in table 1.

Box 1

Table 1

Ratio of media weight to sample weight, varying the grinding time

	Graph		
	Crystalline	Amorphous	
Ratio	20:1	8:1	16:1
Milling hours	3	3	3
	6	6	6
	12	12	

Source: *Own elaboration*

Martínez González (2018) employed a hexagonal graphite together with quasicrystalline icosahedral Al-Cu-Fe particles for their synthesis by milling at a weight ratio of 20:1 for the milling times of 3, 6 and 12 hours. While Valladares Gómez (2018), an amorphous graphite with ratios of 8:1 for 3, 6 and 12 hours of milling; and another ratio of 16:1, for 3 and 6 hours of milling. The heat treatment included placing the previously ground powders in hardened steel crucibles. They were then placed in a muffle-type electric furnace in an air atmosphere at temperatures, as shown in table 2, with an exposure time of 5-6 hours, after which they were allowed to cool to room temperature.

Box 2

Table 2

Heat treatment temperatures of the samples in an air atmosphere

Graph	Temperatures (° C)		
Crystalline (6 h of HT)	200	350	450
Amorphous (5 h of TT)	250	300	450

Source: *Own elaboration*

To determine the main characteristics of the formation and growth of carbon nanostructures in each process, the samples were characterised using X-ray diffraction (XRD), Raman spectroscopy, and transmission electron microscopy (TEM).

Results

Figure 1a shows the X-ray diffraction patterns of the samples subjected to 0, 3 and 6 h of mechanical milling of crystalline graphite (C) with the quasicrystalline phase i-Al-Cu-Fe (both i+C phases) at a 20:1 ball to sample weight ratio. Pattern 1a) shows the mixing of the powders (0 hours) where the typical quasicrystalline i-phase with the hexagonal graphite (C) phase can be seen. A very intense peak located around $2\theta \approx 26.55^\circ$ is observed, which corresponds to the crystallographic plane (002) of the hexagonal graphite, a weaker peak is also observed at $2\theta \approx 54.68^\circ$ corresponding to the plane (004). In the diffractograms corresponding to (b) and (c) with milling times 3 and 6 hours, respectively, a decrease in intensity and broadening of the main graphite peak (002) can be seen, thus indicating a significant decrease in crystal size. From this result, it can be deduced that the graphite is being crushed to smaller and smaller crystal dimensions as a function of milling time. Figure 1b) shows a 2θ magnification of the main peak (002) to observe a shift to the left as a function of milling time. This result shows a growth in the interplanar distance of the graphite, so it is deduced that the material tends to have a distortion of the structural conforms to it. Thus, these results of decreasing crystal size and distortion of the graphitic planes suggest the formation of new distorted carbon structures. On the other hand, the quasicrystal i remains stable, indicating that it functions as a cutting medium.

Box 3

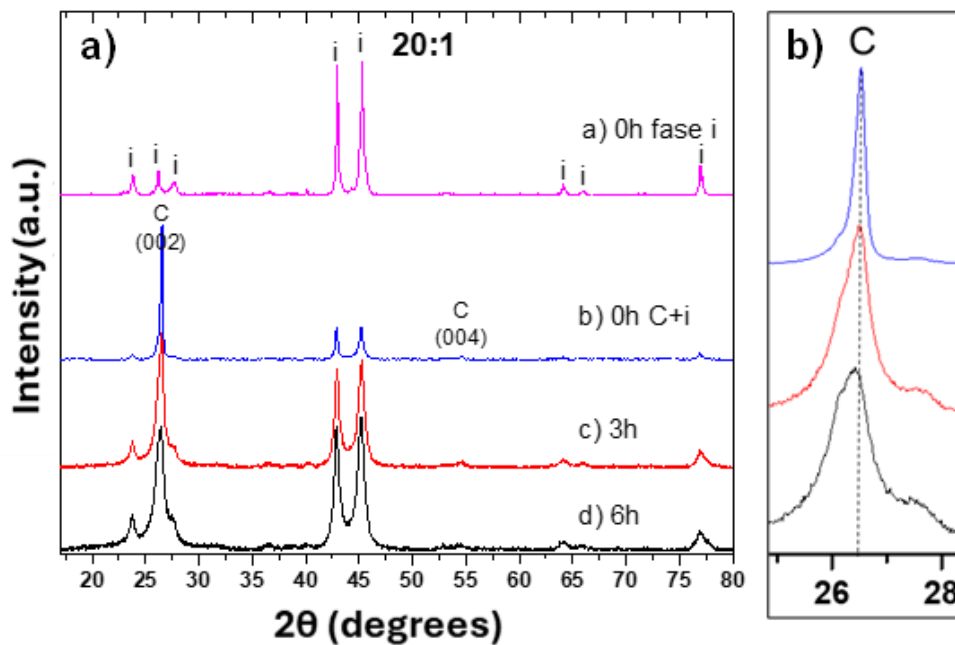


Figure 1

XRD patterns of crystalline graphite C samples with i-phase subjected to different mechanical milling times, a) with a 20:1 ratio, b) enlargement of the 2θ region from 26 to 28 degrees

Source: Own elaboration

Figure 2 shows the XRD patterns of amorphous graphite samples subjected to different grinding times with a ball to sample weight ratio of 16:1 and 8:1. For both ball to sample weight ratios, the position of $2\theta \approx 24^\circ$ of the main peak of the hexagonal graphite (002) of the initial amorphous graphite samples can be seen. It is important to mention that graphite has a tiny particle size and a distortion of its structure, as explained above. For the 3 and 6 hours milled samples with a 16:1 ratio, a thinning of the peaks can be observed (002), thus inferring that the mechanical milling promotes the formation or growth of the graphitic planes. However, for the 8:1 ratio, a widening of the peaks occurs, indicating a more significant decrease in crystal size and a shift of the peaks to the right, indicating a slight decrease in the interplanar distance. From these results it can be deduced that mechanical grinding promotes the formation and growth of distorted graphitic planes.

Box 4

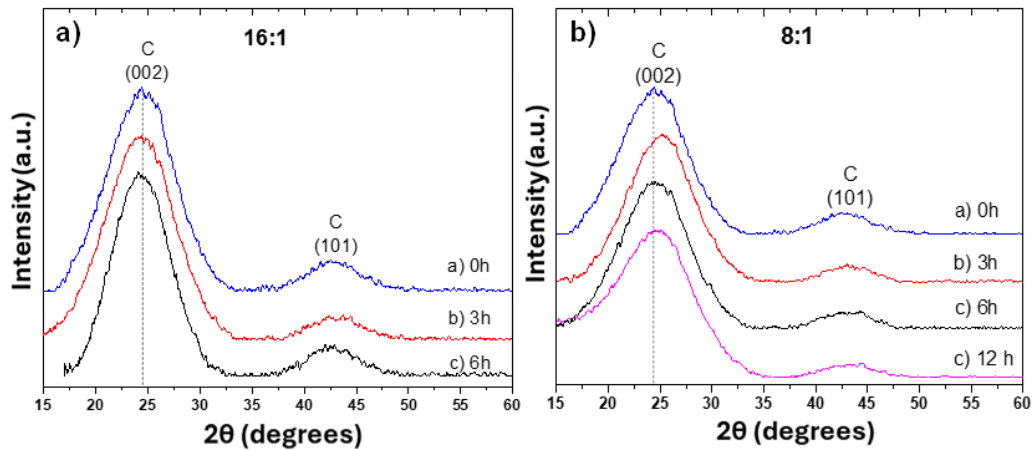


Figure 2

XRD patterns of amorphous graphite samples subjected to different mechanical grinding times with a) 16:1 and b) 8:1 ball to sample weight ratio

Source: *Own elaboration*

The D and G bands are characteristic in graphite and carbon nanostructures for Raman spectroscopy. The D band arises due to defects and disorder in sp^2 carbon hybridization and breathing-type vibrational modes of aromatic ring structures. It is located in the range of 1250 cm^{-1} to 1450 cm^{-1} . G originates from the stretching vibrations of the C-C bonds corresponding to the sp^2 hybridization typical of hexagonal graphite, located between 1500 cm^{-1} and 1600 cm^{-1} . Figure 3 shows the Raman spectra of the samples subjected to mechanical milling, which correspond to a) crystalline graphite milled at a ratio of 20:1, b) amorphous graphite milled at a ratio of 16:1 and c) amorphous graphite milled at a ratio of 8:1. In the spectra a) it can be seen the growth in intensity of the D-band as a function of the milling time, associated with a distortion of the graphitic planes according to the X-ray diffraction results (fig. 1). For the amorphous graphite milling shown in spectra b) and c), a weak growth in intensity of the D-band can be appreciated, however, for the 16:1 milled samples its growth is higher concerning the 8:1. In these results it can be deduced that the quasicrystals together with the balls acted as crushers of the crystalline graphite promoting distortion of the D band, while for the grinding of the amorphous graphite changes are slightly not so noticeable with this technique.

Box 5

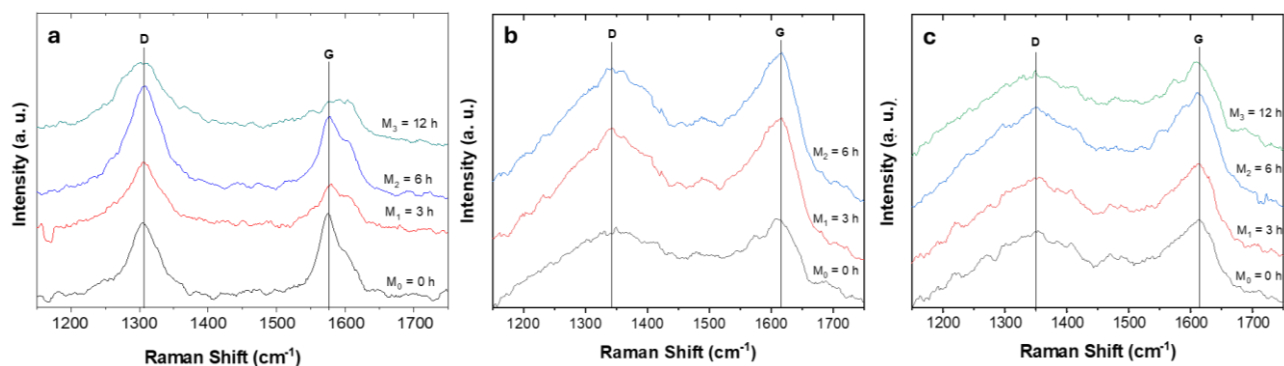


Figure 3

Raman spectra of graphites at different mechanical milling times: a) crystalline + quasicrystalline graphite with a 20:1 ratio, b) amorphous graphite with a 16:1 ratio, and c) amorphous graphite with an 8:1 ratio

Source: *Own elaboration*

Different thermal treatments were carried out to analyse the growth of these nanostructures, using the sample ground for 3 hours of crystalline graphite (20:1 ratio) and amorphous graphite (8:1 ratio). Figure 4 shows the results of each of the spectra and shows an increase in the intensities and a broadening of the D and G bands in the first treated samples. However, when reaching the annealing temperatures of $450\text{ }^\circ\text{C}$, the intensities of the Raman profiles tend to decrease for crystalline graphite since an annealing time of 6 hours has been used while that of amorphous graphite was used for 5 hours.

In both spectra, the growth of the D-band can be significantly noticed, indicating the growth and definition of the carbon nanostructures promoted by the mechanical milling.

Box 6

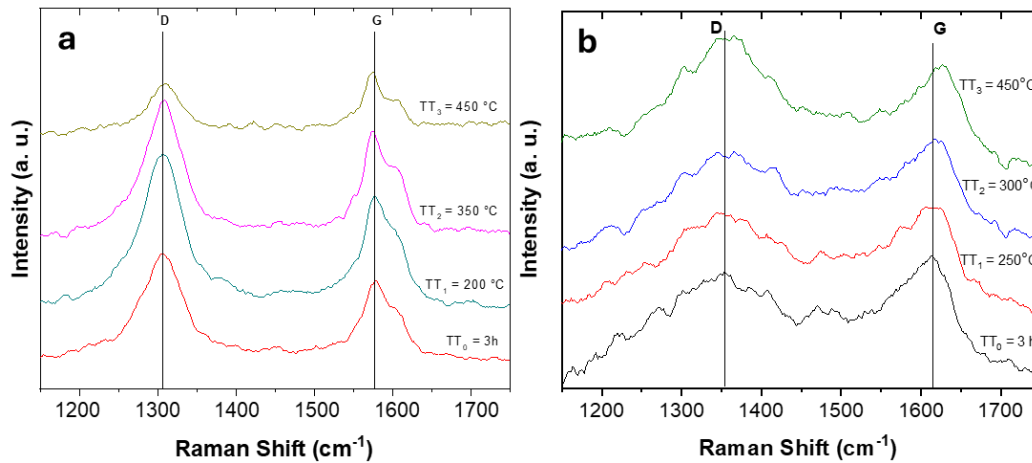


Figure 4

Raman spectra of graphite samples at 3 hours of mechanical milling subjected to different heat treatment temperatures: a) crystalline graphite + i-phase with a 20:1 ratio, b) amorphous graphite with an 8:1 ratio

Source: *Own elaboration*

Table 1 shows the calculated crystal size measurements using the Debye Scherrer formula and the experimental parameters of the XRD profiles. A drastic decrease in the crystal size of the mechanical milling of crystalline graphite can be noticed, thus inferring once again that the milling with the quasicrystalline i-phase has the function of a milling medium. Also, in this table, it is possible to appreciate the effect of the thermal treatment for the milled samples of amorphous and heat treated graphite, where it is possible to find that the thermal treatment temperature of 300 °C has the highest growth percentages and that the samples milled for six h (8:1) and three h (16:1) heat treated at 300 °C achieve 29 and 24 % growth respectively.

Box 7

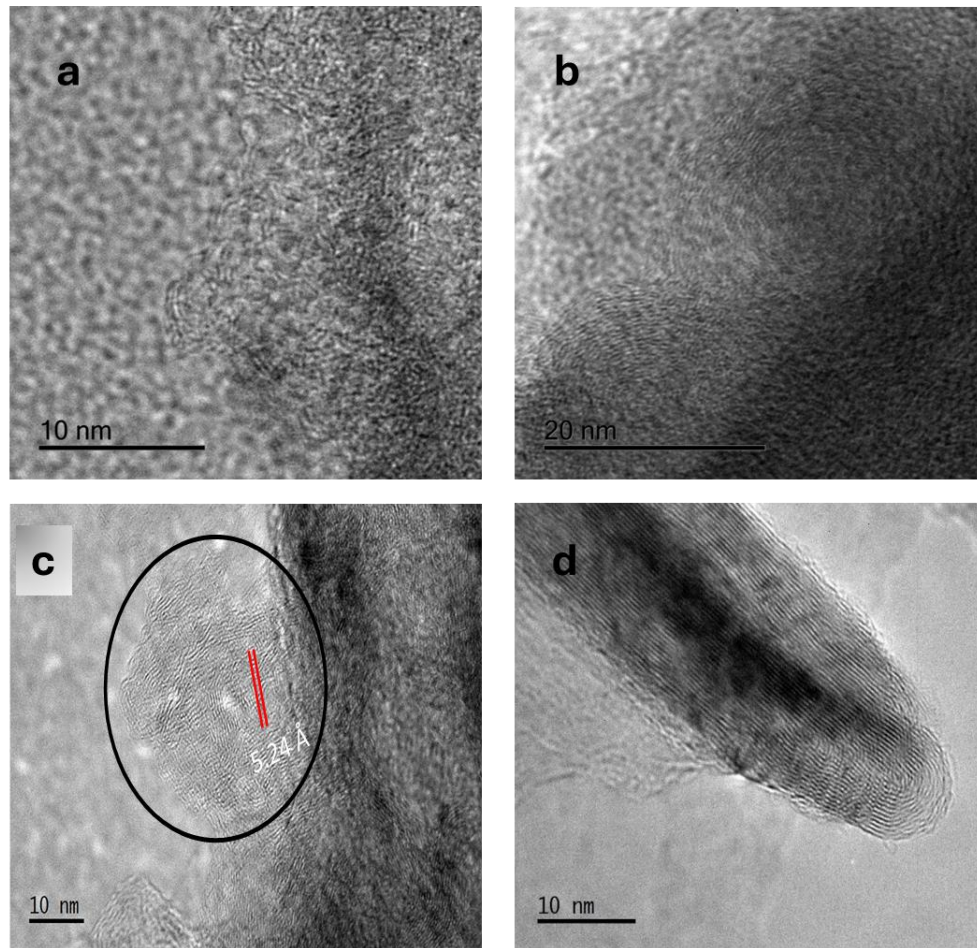
Table 3

Crystal size according to the Debye-Scherrer formula

Crystalline graphite		Amorphous graphite					
Samples	Crystal sizes (nm) a MM	Samples	Crystal sizes (nm) a MM	Crystal sizes (nm) a HT 300 °C	% growth	Crystal sizes (nm) a HT 400 °C	% growth
0h	40.84	0h	0.892	NA	NA	NA	NA
3h, 20:1	11.84	3 h, 8:1	1.039	1.21187	16	1.21648	17
6h, 20:1	11.03	6 h, 8:1	0.9806	1.26601	29	1.14433	16
NA	NA	12 h, 8:1	1.0531	1.2111	15	1.17832	11
NA	NA	3 h, 16:1	0.9838	1.22927	24	1.13429	15
NA	NA	6 h, 16:1	1.275	1.20558	3	1.20924	3

Source: *Own elaboration*

High-resolution transmission electron microscopy has been used to analyse the dimensions and shapes of these nanostructures (figure 5). In these images, it is possible to observe the initial formation of curved nanostructures with a certain degree of distortion, shown in figure 5a), which corresponds to the amorphous graphite sample with an 8:1 ratio and 12 hours of milling. Figure 5b) shows the sample heat-treated at 450 °C, where the formation of well-defined nano-blades with sizes around 20 nm can be observed. In the same way, the crystalline graphite samples with the i-phase milled for 3 hours are presented, where distorted and curved graphitic planes are formed. However, with the heat treatment at 200 °C, the growth of elongated nanostructures in the form of rollers is observed.

Box 8**Figure 5**

HRTEM of: (a) 12 hours grinding at an 8:1 ratio, (b) 12 hours grinding at an 8:1 ratio and heat treatment at 450 °C, (c) 12 hours grinding at a 20:1 ratio, and (d) 3 hours grinding at a 20:1 ratio and heat treatment at 200 °C

Source: *Own elaboration*

Conclusions

Carbon nanostructures have been formed using a mechanical mill that oscillates in one direction, achieving the formation of carbon nanostructures from crystalline and amorphous graphite.

Mechanical milling under these conditions for crystalline graphite tends to reduce its particle size to nanometric orders, and mechanical milling of amorphous graphite promotes the formation of small curved shapes, giving rise to nanoballs smaller than 10 nm.

The grinding time and the ball weight ratio to sample weight are determining factors in forming carbon nanostructures. This is because, as the duration of the process increases, more nanostructures are generated and tend to adopt a single morphology.

The quasicrystal remained stable and acted as a further milling medium, accelerating crystalline graphite's crystal size reduction process.

The heat treatments could define the nanostructures better, and the optimum temperatures ranged around 300 °C under an air atmosphere.

Declarations**Conflict of interest**

The authors declare that they have no conflicts of interest. They have no financial interests or personal relationships that could have influenced this book.

Authors' contribution

Aguilar-Cruz, Felix: contributed to the methodology and writing of the work.

Flores-Gil, Aaron: contributed to the interpretation of the Raman spectra.

Álvarez-García, Emilio: performed the microstructural analysis and methodology.

Patiño-Carachure, Cristóbal: contributed to the XRD and HRTEM characterization analyses.

Availability of data and materials

Data are available on request at: cpatino@pampano.unacar.mx

Abbreviations

XRD	X-Ray Diffraction
HRTEM	High Resolution Transmission Electron Microscopy
TEM	Transmission Electron Microscopy
MM	Mechanical Milling
HT	Heat Treatment

References

Background

Patiño-Carachure, C., Martínez-Vargas, S., Flores-Chan, J. E., & Rosas, G. (2020). [Síntesis de nanoestructuras de carbono por deformación de grafito durante molienda mecánica en aire](#). *Fullerenes, Nanotubes and Carbon Nanostructures*, 28(11), 869-876.

Basics and support

Martínez González, J. (2018). *Análisis de bandas Raman de nanoestructuras de carbono obtenidas por mecano-síntesis de cuasicristales de Al-Cu-Fe* (Tesis de maestría). Universidad Autónoma del Carmen, Facultad de Ingeniería, Ciudad del Carmen, México.

Valladares Gómez, A. J. (2018). *Nanoestructuras de carbono obtenidas por mecano-síntesis y crecidas por tratamiento térmico* (Tesis de maestría). Universidad Autónoma del Carmen, Facultad de Ingeniería, Ciudad del Carmen, México.

Differences and discussions

Ohara, S., Tan, Z., & Abe, H. (2011). [Novel Mechanochemical Synthesis of Carbon Nanomaterials by a High-Speed Ball-Milling](#). *Advanced Materials Research*, 284-286, 755-758.

Carneiro, Í., & Simões, S. (2021). [Heat-Treated Ni-CNT Nanocomposites Produced by Powder Metallurgy Route](#). *Materials*, 14(18), 5458.





Villacorta, B.S., Ogale, A.A. and Hubing, T.H. (2013), [Effect of heat treatment of carbon nanofibers on the electromagnetic shielding effectiveness of linear low density polyethylene nanocomposites](#). *Polym Eng Sci*, 53: 417-423.




SRIKANTH, I., PADMAVATHI, N., PRASAD, P.S.R. et al. [Effect of high-temperature heat treatment duration on the purity and microstructure of MWCNTs](#). *Bull Mater Sci* 39, 41-46 (2016).





Analysis of channel sample in thin section by Raman spectroscopy images





Análisis de muestra de canal en lámina delgada por medio de imágenes de espectroscopía Raman

Castelán-Antúnez, Citli Celeste^a, Flores-Gil, Aarón^b, Patiño-Carachure, Cristobal^c and Urrieta-Almeida, Edgar^d

^a  Universidad Autónoma del Carmen •  LRT-4685-2024 •  0009-0007-4571-8429 •  1318400

^b  Universidad Autónoma del Carmen •  0000-0002-2302-2056 •  121166

^c  Universidad Autónoma del Carmen •  AGZ-9935-2022 •  0000-0002-1436-1259 •  226327

^d  Universidad Autónoma del Carmen •  LRT-5700-2024 •  0000-0003-1668-1966 •  785442

CONAHCYT classification:

DOI: <https://doi.org/10.35429/H.2024.14.27.35>

Area: Physics-Mathematics and Earth Sciences

Field: Physics

Discipline: Molecular physics

Subdiscipline: Molecular spectroscopy

Key Handbooks

This research contributes to the science and technology of materials characterization for the analysis of channel samples from the oil industry, currently using thin films for detailed description with petrographic microscopy, our work is based on using Raman spectroscopy techniques to create images of Raman spectra. Key aspects include understanding the Raman spectroscopy method and the use of thin films in studies of hydrocarbon-bearing rocks. The use of petrographic microscopy and Raman spectroscopy simultaneously allowed detailed spectra of the channel sample to be obtained.

Citation: Castelán-Antúnez, Citli Celeste, Flores-Gil, Aarón, Patiño-Carachure, Cristobal and Urrieta-Almeida, Edgar. 2024. Analysis of channel sample in thin section by Raman spectroscopy images. 27-35. ECORFAN.

* ✉ [\[ccastelan@pampano.unacar.mx\]](mailto:ccastelan@pampano.unacar.mx)

Handbook shelf URL: <https://www.ecorfan.org/handbooks.php>



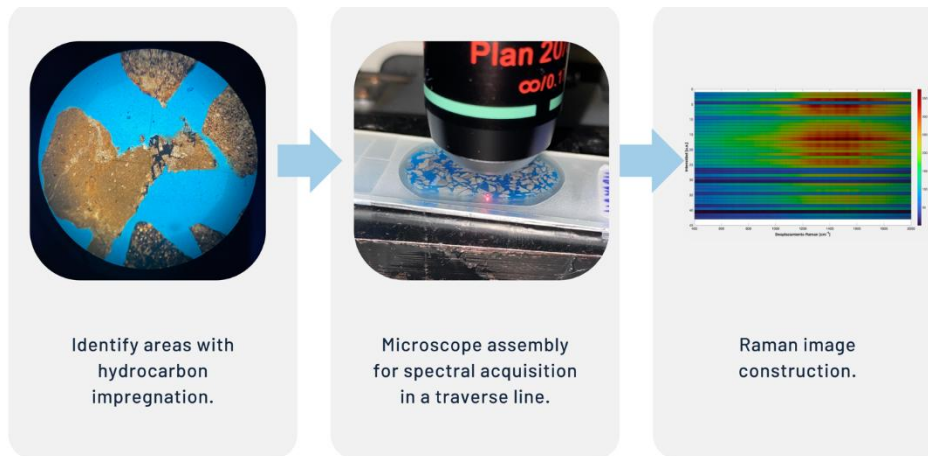
ISBN 978-607-8948-50-5/©2009 The Authors. Published by ECORFAN-Mexico, S.C. for its Holding Mexico on behalf of Handbook HESPCU. This is an open access chapter under the CC BY-NC-ND license [<http://creativecommons.org/licenses/by-nc-nd/4.0/>]

Peer Review under the responsibility of the Scientific Committee MARVID®- in contribution to the scientific, technological and innovation Peer Review Process by training Human Resources for the continuity in the Critical Analysis of International Research.



Abstract

Micro-Raman spectroscopy is an innovative technique for the characterization of hydrocarbon source rocks, specifically in the analysis of core samples in thin sections. This methodology employs an infrared laser that interacts with the molecules of minerals and organic matter, allowing for simultaneous optical imaging with the petrographic microscope and Raman spectrum. In this work, preliminary results of Raman spectra recorded along a line drawn on a thin sheet of a channel sample are presented, using a QE65000-Ocean Optics spectrometer with a spectral resolution of 4 cm^{-1} and a 785 nm laser as the excitation source. To prepare the thin section, the sample is immersed in epoxy resin, cured, and polished in a specialized laboratory until a thickness of $30\text{ }\mu\text{m}$ is reached, where the Raman spectra of the G, D bands, and a carbon double bond, which is related to the organic matter and the resin of the thin section, were analyzed.



Raman Spectroscopy, Petrographic microscope, Thin section

Resumen

La espectroscopía micro-Raman es una técnica innovadora para la caracterización de rocas generadoras de hidrocarburos, específicamente en el análisis de muestras de canal en láminas delgadas. Esta metodología emplea un láser infrarrojo que interactúa con las moléculas de minerales y materia orgánica, permitiendo obtener imagen óptica con el microscopio petrográfico y espectro Raman de manera simultánea. En este trabajo se presentan resultados preliminares de espectros Raman registrados a lo largo de una línea trazada sobre una lámina delgada de una muestra de canal, utilizando un espectrómetro QE65000-Ocean Optics con una resolución espectral de 4 cm^{-1} y un láser de 785 nm como fuente de excitación. Para preparar la lámina delgada, la muestra es inmersa en resina epóxica, fraguada y desbastada en un laboratorio especializado hasta alcanzar un espesor de $30\text{ }\mu\text{m}$, en donde se analizaron los espectros Raman de las bandas G, D y un doble enlace C=C el cual está relaciona con la materia orgánica y la resina de la lámina delgada.



Espectroscopía Raman, Microscopio Petrográfico, Lámina delgada

Introduction

The characterisation of hydrocarbon-bearing rocks requires advanced techniques to study their composition and structure at micrometric scales. In this context, the use of thin films in petrographic microscopy is a traditional technique used in the oil industry to identify the type of lithology and to analyse the chronostratigraphic age through microfossils. Raman spectroscopy instead provides an alternative to obtain detailed information on the mineral components and organic matter present in these rocks. Channel samples, especially prepared in thin films, allow the textures and mineralogical phases of the rocks to be observed under a petrographic microscope, which is crucial for identifying petrographic features that influence their hydrocarbon generation and retention capacity (Fries, M., & Steele, A., 2010).

Raman spectroscopy complements this characterisation by providing accurate chemical and structural analysis at the micrometre level. Using a laser that interacts with the molecules of the materials present, this technique detects specific vibrations that reveal the composition and internal organisation of minerals and organic matter (Ferrari & Robertson, 2000). Raman spectroscopy is a useful tool for the identification of minerals and the study of carbonaceous material, which is difficult to characterise with optical microscopy and electron beam techniques. For example, it allows differentiation between carbonaceous matter present in primary fluid inclusions, which formed when a rock first cooled from its parent material, and other carbonaceous matter located in late-phase alteration veins within the same rock (Figure 1).

Box 1

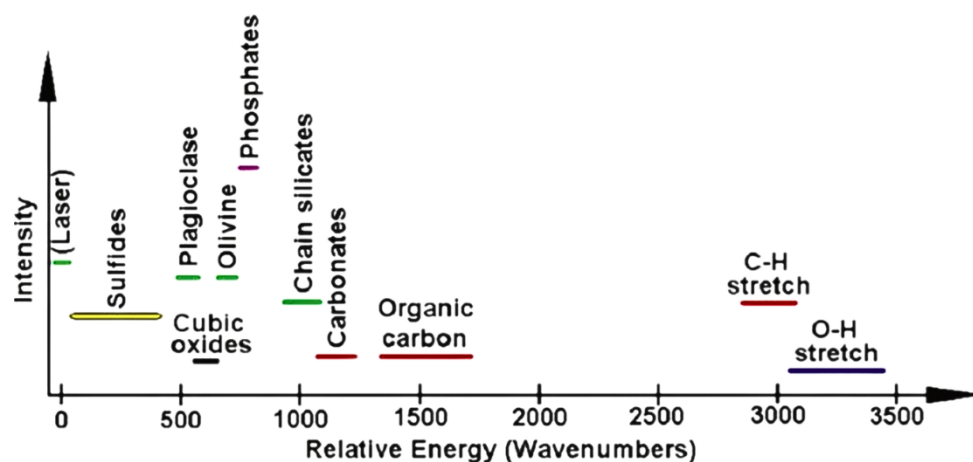


Figure 1

Simplified diagram showing the general positions of prominent Raman peaks for a variety of common rock-forming minerals and compounds

Source: [Fries, M., & Steele, A., 2010]

In this study, both microscopic techniques are combined to analyse channel samples prepared in thin films, assessing both their petrographic characteristics using a petrographic microscope and their molecular composition using a laser Raman microscopy system design. This integrated approach facilitates the analysis of hydrocarbon source rocks, providing essential information for understanding their reservoir potential and key geological properties (Marshall et al., 2007). The results obtained will contribute to a better understanding of the composition and structure of these complex geological systems, enhancing their analysis and evaluation in the context of hydrocarbon exploration and production.

Thin films

Thin sections or thin sections are rock samples used in petrography to study the optical properties of minerals. They are made in such a way that they are polished on both sides to allow light to pass through to observe the optical characteristics of the minerals. The film is fixed to a glass slide. According to Fries, M., & Steele, A., 2010, surface irregularities on thin sections and contamination, such as polymer mounting particles, can interfere with Raman analyses.

Surface imperfections, caused by minerals such as pyroxenes or clays, can scatter the laser excitation beam, and the materials used to create the slices can be confused with materials in the rock or sediment. To avoid this, it is recommended to examine the thin section in reflected light prior to analysis. In addition, the mounting polymer, especially in brittle materials, can be trapped in the cracks, which can make it difficult to interpret the spectra, although it can be differentiated by its spectral signature in the C-H stretching region.

Raman spectroscopy

Raman spectroscopy is a non-destructive analytical technique that provides information about the molecular structure and internal vibrations of the bonds of a material, whether liquid, solid or gas, by inelastic light scattering (Smith & Dent, 2004). When monochromatic radiation of minimum frequency passes through a transparent medium, most of it is transmitted, a fraction is absorbed and a small amount is scattered (less than 10^{-5} of the intensity of the exciting source). Most of the scattered light maintains the same frequency as the incident radiation (known as elastic or Rayleigh scattering), while a very small amount (on the order of 10^{-3} to 10^{-4} of the Rayleigh intensity) is scattered at a frequency slightly higher or lower than the incident radiation. This inelastic scattering is called Raman scattering (Jawhari, 2012).

Optical imaging with microscopy and Raman spectra

Mineralogy and petrography techniques have traditionally relied on thin-sheet optical microscopy to identify minerals and study their arrangement, which allows interpretation of the formation and alteration of these minerals and the source rock. This helps to understand the evolution of geological formations and their relationship to larger units, even inferring events such as the movement of continents. Raman spectroscopy is a useful tool in these analyses, especially for identifying minerals and studying carbonaceous matter, which is difficult to characterise with optical microscopy and electron beam techniques with SEM or EDX (Fries, M., & Steele, A., 2010).

Methodology

The methodology is presented in two parts, the first part covers the creation of the thin film at the Centro Regional de Estudios de Laboratorio Cd del Carmen of Pemex Exploración y Producción KM 4+500. And the second part is the analysis by Raman spectroscopy coupled to a Best Scope BS-5070TTR petrographic microscope adapting the Raman probe to measure the thin film of the channel sample.

Thin film of source rock

The channel sample or drill cuttings are subjected to a cleaning process in the laboratory, as they may contain water, drilling mud and/or plugs. A sample is selected at a stratigraphic level from an exploration well. For channel samples, the following steps are performed (Figure 2):

1. A representative sample of hydrocarbon-bearing rock is selected, washed until any drilling mud and pluggers it may contain are removed, oven dried at a temperature of less than 80°C.
2. It is then sieved with a 40 and 10 mesh to obtain a homogeneous granulometry.
3. It is agglutinated in an epoxy resin to facilitate its handling. The mixing ratio of the resin and catalyst must comply with the standards to guarantee the preservation of the characteristics of the sample (3:1 ratio), it is left to set until the following day.
4. Once the resin has set, the sample is cut into a rectangular shape with a diamond saw to obtain a preliminary sheet, ensuring that the surface is flat and suitable for polishing.
5. The roughened sample is adhered to a glass slide using an adhesive that reacts with UV light. This ensures that it is firmly adhered (Solis Correa, 2023).
6. To reduce the thickness of the sample and approach the final thickness (30 μm), different grains of silicon carbide paper, usually 120, 220 and 400, are used, wetting the surface to avoid excessive heat and maintain the integrity of the sample (Casique et al., 2018).

7. For final polishing, a 600 grit aluminium oxide or silicon carbide powder is used to obtain a thickness of 30 μ m, ensuring optimal light transmission through the thin film during petrographic observation.
8. Finally, the thickness of the foil is checked with the BestScope BS -5070TTR petrographic microscope to ensure that it meets the 30 μ m standard required for petrographic analysis (Casique et al., 2018).

Box 2

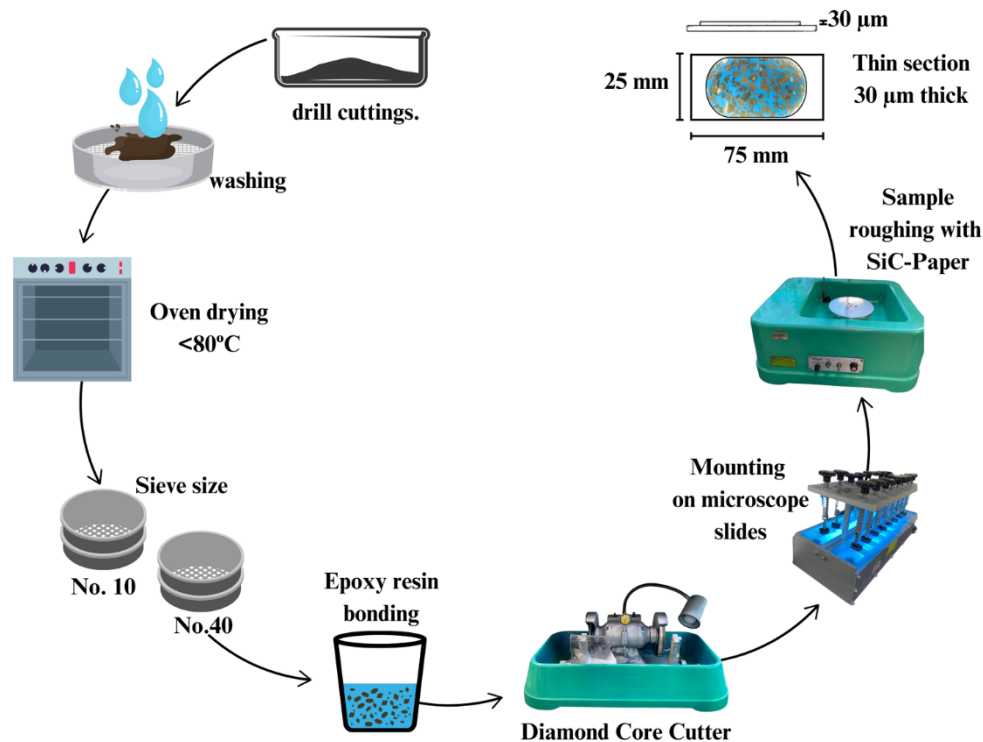


Figure 2

Methodology for the creation of a 30 μ m thick, thin film: Washing and drying of the sample. Sieved and impregnated in epoxy resin. Cut and mounted on slides. Deburring with SiC (Silicon Carbide) paper 120, 220 and 400 grit; final polishing with 600 grit Silicon Carbide powder

Source: [Own elaboration]

Design of the laser Raman microscopy system

The Raman equipment was mounted on the BestScope BS petrographic microscope of the UNACAR Optics Laboratory, as shown in Figure 3. The optical system consists of a 785 nm infrared laser module, connected to a bifurcated optical fibre, coupled to the laser and the spectrograph.

A path was delimited on the Y axis of the sample surface and the Raman spectrum was measured every 1 mm, obtaining a total of 43 spectra, the purpose of adapting the HD camera is to observe that the laser does not hit the epoxy resin. The signal is captured with the Ocean Optics QE 65000 spectrometer. The data is captured with SpectraSuite software for Windows operating systems, then the data is saved in .txt format for graphing in Matlab.

The processing was done by trimming the spectral band selection from 400 to 2000 cm^{-1} , for all the spectra obtained. A surface plot was made in Matlab to evaluate the maximum peaks using a colour scale.

Box 3

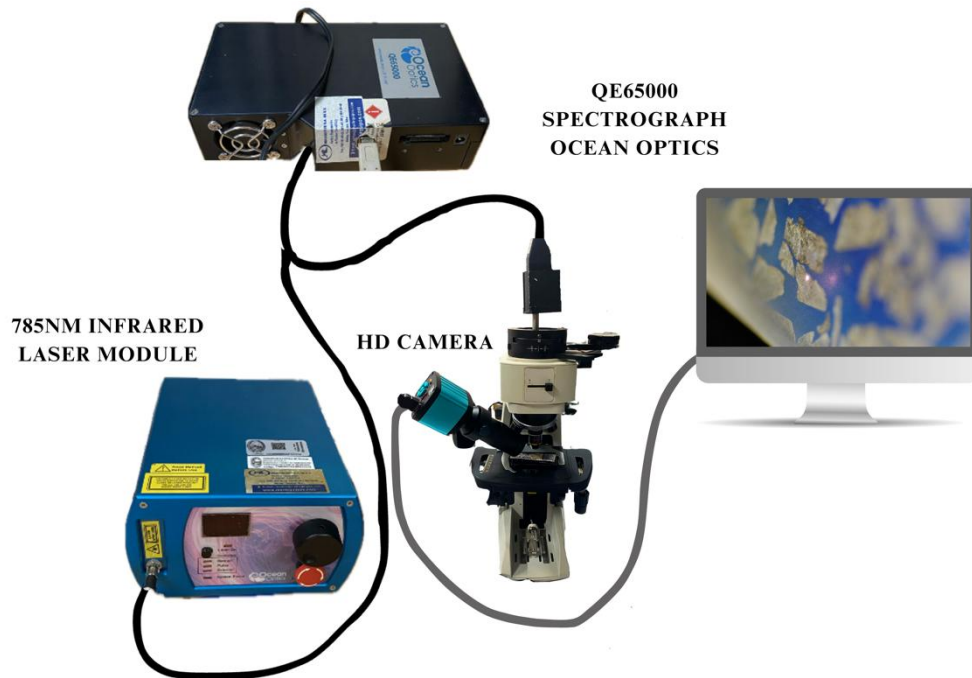


Figure 3

Adaptation of the QE65000 spectrograph to the Best Scope BS-5070TTR petrographic microscope, using a 785 nm infrared laser module with 20x objective as excitation source, and an HD camera with 4x objective to verify the laser path

Source: [Own elaboration]

Results

Raman spectra of a thin-film scan of the sample

The optical Raman microscopy system was developed for the simultaneous acquisition of images with the petrographic microscope and the Raman probe, which allows the reading of the data where there is no presence of epoxy resin. The data presented are from a single run of the sample, since, having a heterogeneous sample, the data are shown with high fluorescence. It is known that when analysing low concentration materials (below 1%) and materials that fluoresce or samples with fluorescent impurities, they raise the fluorescence background and interfere considerably with the Raman signal (Jawhari, 2012). This phenomenon commonly occurs in organic materials and certain compounds.

The Raman bands identified were as follows:

Quartz: $\sim 450\text{-}462\text{cm}^{-1}$ (Rutt, H. N., & Nicola, J. H., 1974), (Ostroumov et al., 2002).

Carbonate: $\sim 1415\text{-}1437\text{cm}^{-1}$ (Band C) (Hernando Alonso et al., 1937).

Carbon: ~ 1350 (Band D) and $\sim 1600\text{ cm}^{-1}$ (Band G) (Myers, G. A., Kehoe, K. K., & Hackley, P., 2017), (Lambrecht et al. 2021).

Silicon: 520.4 cm^{-1} (S-band) (Myers, G. A., Kehoe, K. K., & Hackley, P., 2017).

Carbon-carbon double bonds: 1540cm^{-1} , 1500 cm^{-1} (La Rosa-Toro Gómez, A., & D'Arrigo, D. V., 2022), (Fries, M., & Steele, A., 2010).

It is important to mention that carbon is a relevant material in the area of materials and energy engineering, for example graphene is also characterised by its D and G bands, since due to its two-dimensional structure and its high thermal and electrical conductivity, they are key in technological innovation (Madrigal Rodríguez, 2024), (Vargas Henao, 2024).

Box 4

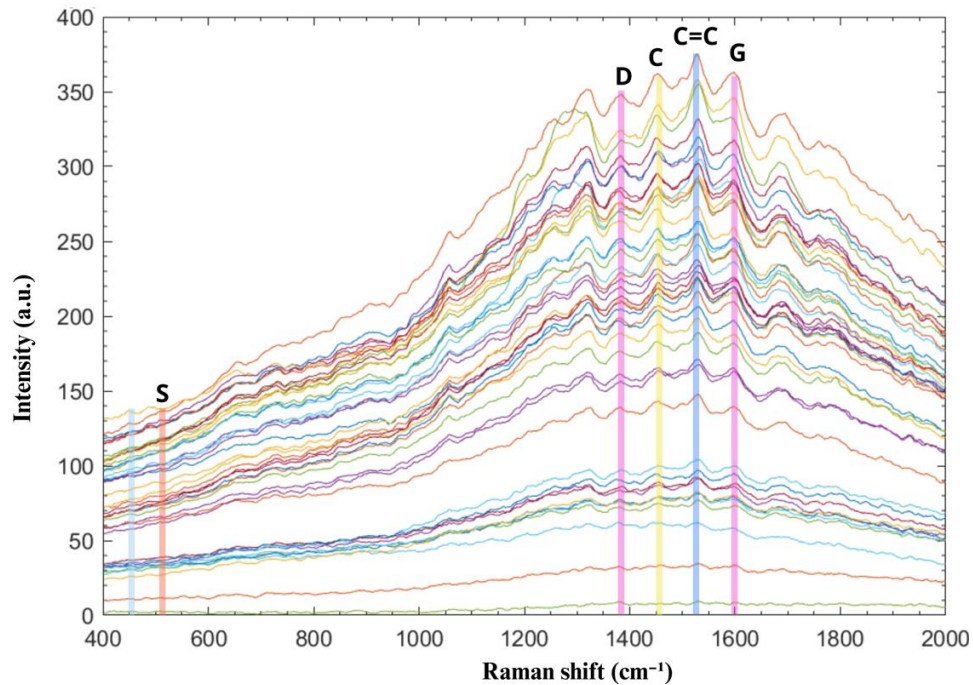


Figure 4

Shown are 43 Raman spectra of a Y-path of a thin film of channel sample, Raman shift from 400 to 2000 cm^{-1}

Source: [Own elaboration]

Surface map of Raman spectra

A graph is presented in figure 5, as a start for the creation of a Raman image for a channel sample. For a qualitative analysis it is important to identify the bands of higher intensity (warm colours) with a colour map that allows to delimit the regions with presence of organic matter, or with presence of carbon double bonds.

Box 5

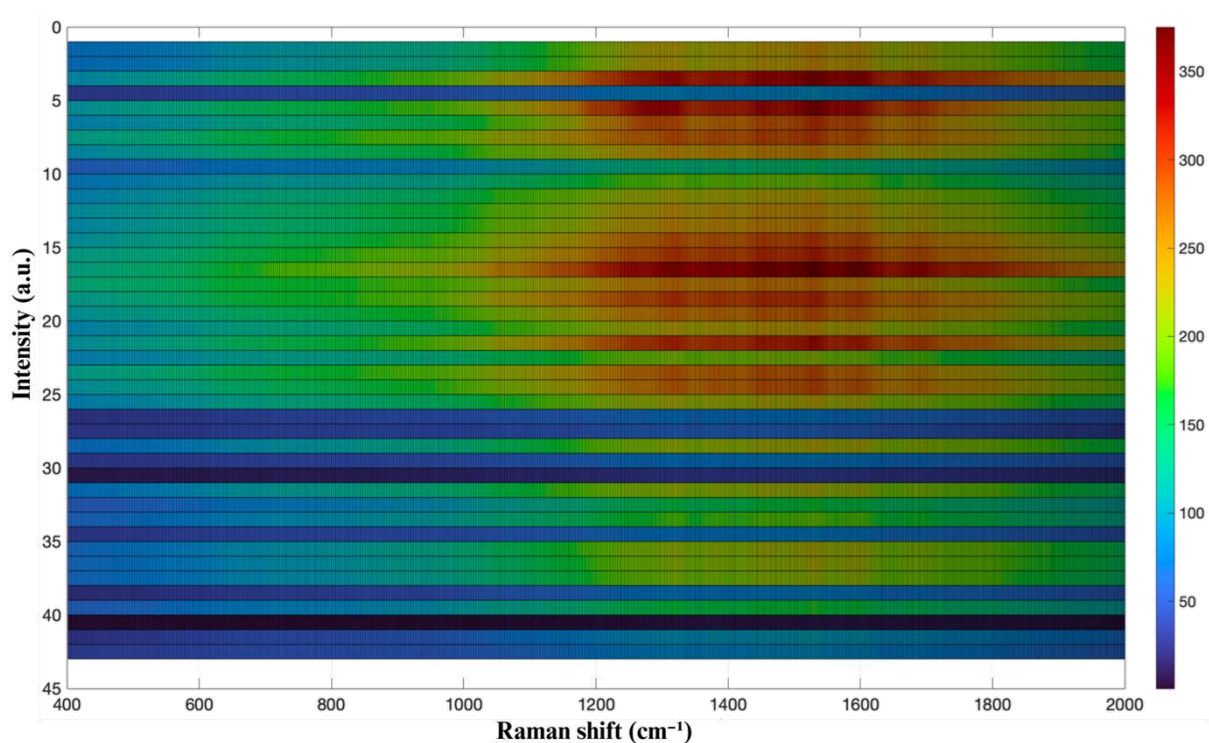


Figure 5

Surface map of 43 spectra on a y-axis path of a thin sheet of channel sample. The warmer colours are seen for high intensities and cooler colours for low intensities

Source: [Own elaboration]

Statements

Conflict of Interest

The author declares that he has no conflicts of interest. He has no known competing financial interests or personal relationships that might have appeared to influence the article reported in this chapter.

Authors' contributions

Citli Celeste Castelán Antúnez, Preparation of this document; Flores Gil Aarón, Patiño Carachure, Cristobal and Urrieta Almeida, Edgar, Support in the development of the project and writing of the document.

Availability of data and materials

The information contained in this document is available upon request from the principal author.

Funding

No funding was received.

Acknowledgments

Thanks are due to the Master's program in Materials and Energy Engineering of the Universidad Autónoma del Carmen and to the CONAHCYT Scholarship program, and to the professors for their advice in the development of the project. The support of the Centro Regional de Estudios de Laboratorio Cd. del Carmen de Pemex Exploración y Producción KM 4+500 for the realization of the thin films is gratefully acknowledged.

Conclusion

In conclusion, the simultaneous use of petrographic microscopy and Raman spectroscopy allowed us to obtain detailed spectra of the channel sample. The spectra obtained from the thin film channel sample show the presence of minerals such as quartz, carbon and silicon, among others that are yet to be identified; in addition to other bands such as those associated with polymers with the carbon double bond. The bands D 1360 cm⁻¹ and G 1600 cm⁻¹ of carbon structures were identified, as well as the band associated with carbonate 1450 cm⁻¹. The analysis revealed a high fluorescence in the spectra, due to the heterogeneity of the sample and the presence of organic matter associated with rock with high clay content.

References

Background

Ferrari, A. C., & Robertson, J. (2000). *Interpretation of Raman spectra of disordered and amorphous carbon*. Physical Review B, 61(20), 14095.

Casique, E. M., Arce Saldaña, J. L., & Lezama Campos, J. L. (2018). *Analysis of the stratigraphy and hydrogeological characteristics of the deep strata that make up the subsurface of the Mexico Basin from the drilling of two deep wells, one at 2000 m and the other at 1570 m called Agricola Oriental*. Bulletin of the Institute of Geology of the National Autonomous University of Mexico, 17-21.

Rutt, H. N., & Nicola, J. H. (1974). *Raman spectra of carbonates of calcite structure*. Journal Of Physics C Solid State Physics, 7(24), 4522-4528.

Hernando Alonso, I., Fesharaki, O., Sánchez-Pastor, N., Casado, A. I., Astilleros, J. M., Lobato, Á., Tarabilla, M., & Fernández-Díaz, L. (1937). *Raman spectroscopic analysis of fossil bones of micromammals from the palaeontological site of Húmera (Madrid)*. Spanish Society of Mineralogy, 21, 56-58.

Myers, G. A., Kehoe, K. K., & Hackley, P. (2017). *Analysis of Artificially Matured Shales with Confocal Laser Scanning Raman Microscopy: Applications to Organic Matter Characterization*. Unconventional Resources Technology Conference, 1683-1698.

Ostroumov, M., Faulques, E., & Lounejeva, E. (2002). *Raman spectroscopy of natural silica in Chicxulub impactite, Mexico*. Comptes Rendus Géoscience, 334(1), 21-26.

La Rosa-Toro Gómez, A., & D'Arrigo, D. V. (2022). *Electropolymerization of pyrrole on copper and its evaluation as a corrosion inhibitor*. Journal of the Chemical Society of Peru, 88(2).

Lambrecht, G., De Vera, C. R., Jambrina-Enríquez, M., Crevecoeur, I., Gonzalez-Urquijo, J., Lazuen, T., Monnier, G., Pajović, G., Tostevin, G., & Mallol, C. (2021). *Characterisation of charred organic matter in micromorphological thin sections by means of Raman spectroscopy*. Archaeological And Anthropological Sciences, 13(1).

Solís Correa, N. (2023). *Petrographic and Petrophysical Characterization of Bituminous Sandstones of the Mesón Formation, Tampico-Misantla Basin*. Universidad Autónoma de Nuevo León.

Marshall, C. P., Leuko, S., Coyle, C. M., Walter, M. R., Burns, B. P., & Neilan, B. A. (2007). *Carotenoid Analysis of Halophilic Archaea by Resonance Raman Spectroscopy*. Astrobiology, 7(4), 631- 643.

Basic

Smith, E., & Dent, G. (2004). *Modern Raman spectroscopy: A practical approach*. J. Wiley.

Jawhari, T. (2012). *Raman spectroscopy as a powerful analytical tool: probing the structure of matter*. Centres Científics i Tecnològics. Universitat de Barcelona eBooks.

Support

Fries, M., & Steele, A. (2010). *Raman Spectroscopy and Confocal Raman Imaging in Mineralogy and Petrography*. Springer Series in Optical Sciences, 111-135.

Discussions




Madrigal Rodríguez, H. (2024). *Graphene: properties and applications in Engineering*. University of Valladolid.





Vargas Henao, M. (2024). *Design of processing parameters for the injection moulding of alumina and graphene powders*. Universidad de los Andes.




Manufacturing and mechanical characterization of eco-friendly blocks using organic waste as aggregate

Fabricación y caracterización mecánica de bloque ecológico empleando desechos orgánicos como agregado

Muñoz-Talango, Dayana G.*^a, Abatal, Mohamed^b and Santiago-de la Cruz, Arlette A.^c

^a  Universidad Autónoma del Carmen •  0009-0003-5781-7150 •  1322115

^b  Universidad Autónoma del Carmen •  G-6047-2018 •  0000-0003-2479-8769 •  203026

^c  Escuela Nacional de Estudios Superiores Unidad Morelia •  0000-0003-4020-9936 •  48364

CONAHCYT classification

DOI: <https://doi.org/10.35429/H.2024.14.36.47>

Area: Physics - Mathematics and Earth Sciences

Field: Physics

Discipline: Solid state physics

Sub-discipline: Composite Materials

Key Handbooks

Propose a new composite material using organic waste for the construction of ecological block with low environmental impact. The properties of the material, including its composition and mechanical characteristics, are fundamental. It is also crucial to consider construction norms and standards, ensuring that the test methods and parameters evaluated comply with applicable national standards. On the other hand, the manufacturing method, process design, material selection and optimisation play a key role. These aspects form the basis for generating and consolidating knowledge to foster future research in the development of environmentally friendly materials. The results of the compression tests indicate that the evaluated samples do not meet the minimum simple compressive strength requirement of 2 MPa (equivalent to 20.39 kg/cm²). Samples with 2.5% fibre content have a compressive strength range of 11.1 to 18.74 kg/cm², which is below the minimum required value. The base sample, without fibre content, shows a slightly higher compressive strength, reaching 19.01 kg/cm².

Citation: Muñoz-Talango, Dayana G., Abatal, Mohamed and Santiago-de la Cruz, Arlette A. 2024. Manufacturing and mechanical characterization of eco-friendly blocks using organic waste as aggregate. 36-47. ECORFAN.

* ✉ [\[100489@mail.unacar.mx\]](mailto:100489@mail.unacar.mx)

Handbook shelf URL: <https://www.ecorfan.org/handbooks.php>



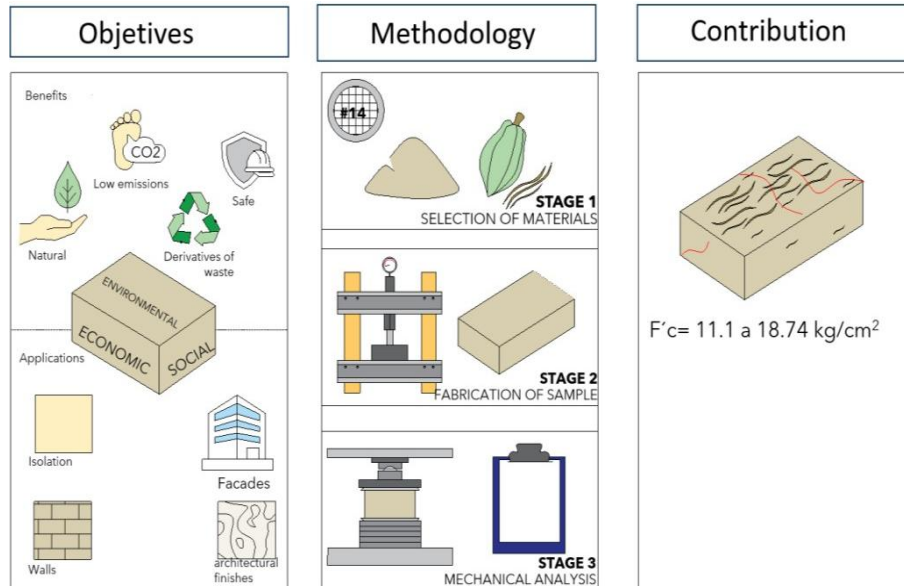
ISBN 978-607-8948-51-2/©2009 The Authors. Published by ECORFAN-Mexico, S.C. for its Holding Mexico on behalf of Handbook HRPG. This is an open access chapter under the CC BY-NC-ND license [<http://creativecommons.org/licenses/by-nc-nd/4.0/>]

Peer Review under the responsibility of the Scientific Committee **MARVID**[®] in contribution to the scientific, technological and innovation Peer Review Process by training Human Resources for the continuity in the Critical Analysis of International Research.



Abstract

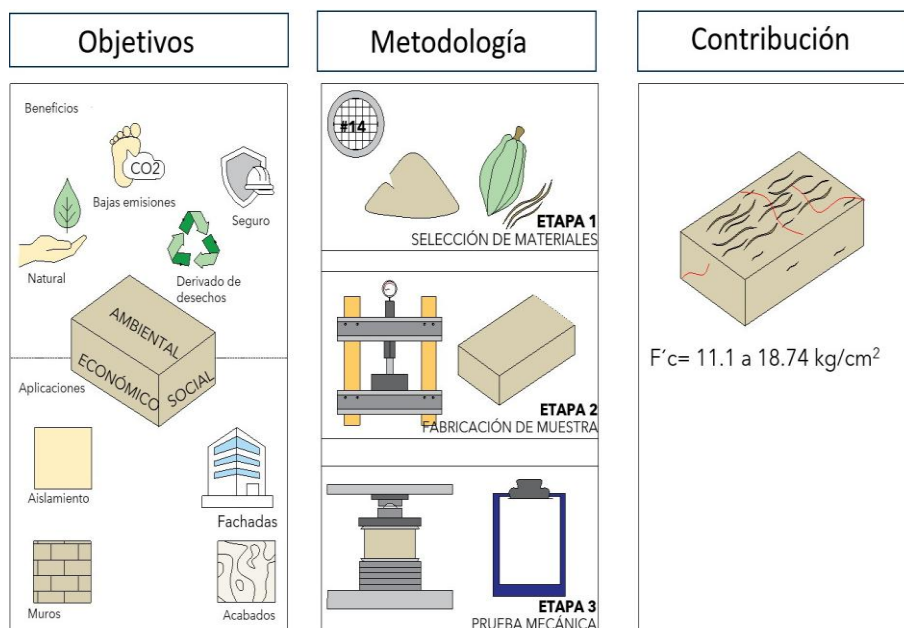
Population growth and the demand for habitable spaces have turned construction into a critical challenge for environmental sustainability. This industry, characterized by its high dependence on raw materials, not only depletes natural resources but also leads to ecosystem degradation and pollutant emissions. Therefore, it is essential to research new materials that not only comply with industry regulations but also reduce environmental impact and promote more sustainable practices. Currently, eco-blocks are emerging as a viable alternative with significant environmental benefits. This work establishes the methodology for manufacturing an ecological block using natural fibers considered as waste as aggregate and determines its mechanical properties. Additionally, the compressive strength obtained is compared with other materials available on the market and those reported in the literature to assess its potential.



Mechanical properties, natural fibers, eco-blocks

Resumen

El crecimiento de la población y la demanda de espacios habitables han convertido la construcción en un desafío crítico para la sostenibilidad ambiental. Esta industria, marcada por su elevada dependencia de materias primas, no solo agota los recursos naturales, sino que también provoca la degradación de los ecosistemas y emisiones contaminantes. Por ello, es fundamental investigar nuevos materiales que no solo cumplan con las normativas del sector, sino que también disminuyan el impacto ambiental y fomenten prácticas más sostenibles. Actualmente, los eco-bloques se presentan como una alternativa viable con significativos beneficios medioambientales. En este trabajo, se establece la metodología para la fabricación de un bloque ecológico empleando fibras naturales consideradas desecho como agregado y se determinan sus propiedades mecánicas. Además, se comparan fuerza de compresión obtenida con otros materiales disponibles en el mercado y aquellos reportados en la literatura, con el fin de identificar su potencialidad.



Propiedades mecánicas, Fibras naturales, Eco-bloques

Introduction

The environmental impact of the construction industry is alarming, as it originates mainly from the massive extraction of natural materials, greenhouse gas emissions, excessive primary energy consumption and the production of unmanaged waste (Aghimien et al., 2019). This sector is a major source of greenhouse gas emissions, mainly due to the industrial processes required for the production of cement and other building materials. These processes, which include extraction, transportation and manufacturing, generate a significant amount of emissions, and, perhaps most critically, waste generation (López Ruiz et al., 2020).

Cement is used to make concrete and mortar, and is the second most consumed compound on the planet (Scrivener et al., 2018). Concrete is used to build homes, schools, hospitals, workplaces and infrastructure for human development. The raw materials used in the manufacture of cement are obtained mainly through quarrying for the extraction of hard rocks such as limestone, slate and certain shales. In some cases, the deposits are exploited by underground methods (International Energy Agency, 2018; Scrivener et al., 2018).

The process of making cement is well established and has hardly changed since it was first developed almost 200 years ago (Hart, 2022). The process is shown in Figure 1 and consists of three stages: the first is extraction of raw materials and their preparation, the second stage can be defined as hot cycle or Clinker production and finally cold cycle, where Clinker is mixed with other components such as gypsum for cement production (Hart, 2022). Clinker is normally a mixture of limestone (calcium carbonate) and siliceous materials (clays) which are heated in a kiln to temperatures of around 1450 °C, this phase releases direct_{CO2} emissions. Between 30% and 40% of emissions are produced by burning fuels and 60-70% come from chemical reactions (Fayomi et al., 2019).

Box

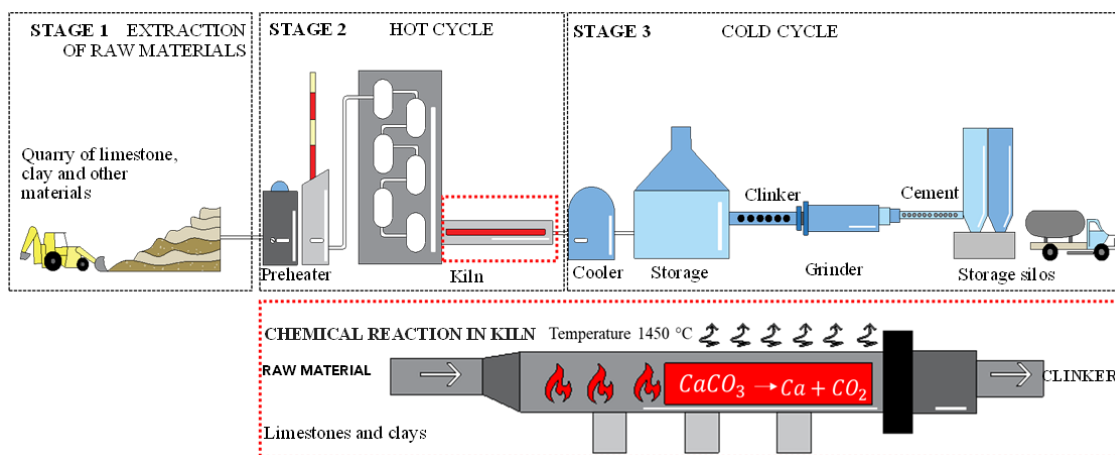


Figure 1

Cement production process and chemical reaction

Source: Own elaboration

The cement sector is the third largest energy consumer in the industry, more than 90% of the energy required for cement manufacturing is obtained from fossil fuels, while the remaining 10% is obtained from electricity (Aghimien et al., 2019). The industry's energy consumption is accounting for 7% of global energy consumption, equivalent to 10.7 exajoules (1EJ= 10^{18} J). The concern for energy alternatives and more efficient production processes stems from the fact that 30% to 40% of total emissions come from fuel combustion (International Energy Agency, 2018). The most commonly used fuels in the cement industry were coal, coke or heavy oils (Müller et al., 2008).

Global population growth and urbanisation patterns, together with increasing demand for infrastructure, will drive an increase in demand for cement and concrete. Currently, the production of one tonne of cement generates between 0.65 and 0.95 tonnes of_{CO2}, depending on the efficiency of the process (Müller et al., 2008). By 2050, global cement production is estimated to increase by 12-23% from the current level (International Energy Agency, 2018).

The global cement industry faces the challenge of ensuring its commercial viability while reducing its carbon intensity. This requires transformations in production processes, optimising fuel use and developing new materials that minimise environmental impact.

Actions taken in the building industry can have an immediate impact on global climate change, as well as on energy consumption and economic and social consequences (Chen et al., 2024; Oberle et al., 2019). While these strategies can help the building sector move towards sustainability by promoting innovative solutions that integrate environmental awareness, such as smart concrete, it is critical to recognise that emissions are linked to the production process (Tian et al., 2024). Advances in materials can be integrated with innovative production methods and technologies as well as old construction methods that often offer environmental benefits.

The incorporation of sustainable building materials in projects worldwide aims not only to combat climate change, but also to promote awareness in construction. It can also generate significant economic savings by improving the methodology and application of life cycle costing (LCC), particularly in the construction, maintenance and operation sections (Liu et al., 2022).

Until the mid-19th century, buildings were mainly constructed with natural materials such as wood, adobe, earth and local fibres. Subsoil construction is one of the oldest techniques, being the basis of early dwellings and cities, which used raw earth to create simple shelters from easily accessible materials (Touré et al., 2017). Even today, in many parts of the world, earthen buildings can still be found, often combining this material with other materials to improve their resistance (Jesudass et al., 2020; Pacheco-Torgal & Jalali, 2012). Natural fibres, in particular, offer great potential in the field of civil construction, as they can contribute to more sustainable architecture in the future (Balasubramanian et al., 2024). This would not only allow for a greater diversity of building materials, but also encourage design innovation and the improvement of conventional materials (Steffens et al., 2017). Fibres act as mechanical reinforcement, especially in terms of tensile and flexural strength in concrete (Hamada et al., 2023).

Methodology

In Figure 2, the three stages that make up the research methodology applied in this study are illustrated in detail. Each stage reflects a key step in the fabrication, characterisation, analysis and interpretation of data, ensuring that the results obtained are relevant and reliable for the context of the study.

Box 2

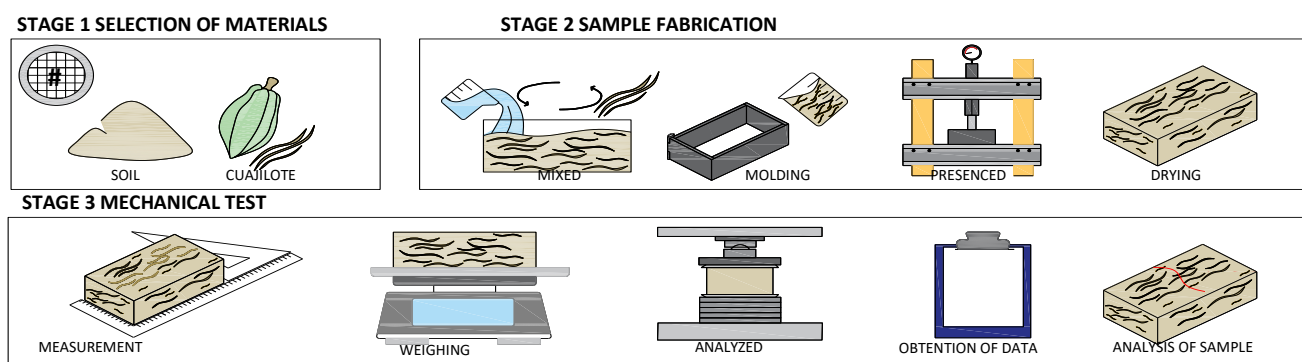


Figure 2
Methodology applied

Source: Own elaboration

Stage 1 Selection of materials

Choice of soil

Sahcab or saskab was used as a base material, which is considered an abundant limestone soil in the Yucatan peninsula, and is one of the most widely used materials in construction. This soil can be in the form of gravel or silty sand, it is of sedimentary origin and its chemical composition consists mainly of calcium carbonate (Alonzo et al., 2006). The material was sieved on a #14 stainless steel mesh with an aperture of 1.40mm (0.0555").

Choice of aggregate

Parmentiera aculeata, also known as cuajilote or tree cucumber, was used as an aggregate for the ecological block. This species is widely distributed in southern Mexico and is found in Chiapas, Tabasco and Campeche. The ‘cuajilote’ tree can produce more than 600 fruits in a single year (Hellmuth, 2023). The cuajilote produces fibrous fruits with a high content of lignocellulosic compounds, based on the ‘Study of the cellular architecture and micromechanical properties of cuajilote fruits. Using different microscopy techniques’, where the micromechanical properties of the fruit were analysed, demonstrating that the orientation of the fibrils can help to improve mechanical properties for future applications (Vicente et al., 2021). Previously dried and separated into strands ≤ 30 cm.

Stage 2. Sample fabrication

The design of the block was stipulated under the standard N-CMT-2-01-001/02, which defines the standardised parameters for working the sample. This standard contains the quality requirements for bricks and ceramic blocks that are used in ceramic bricks and blocks used in masonry structural elements. Table 1 presents the specifications applicable in this research.

Box 3

Table 1

Applicable block specifications under N-CMT-2-01-001/02- Standard N-CMT-2-01-001/02- Standard N-CMT-2-01-001/02- Standard N-CMT-2-01-001/02

Ranking	Manufacturing	by hand
	Subtypes	Massifs: Usually do not develop ceramic bonds and are only massive..
	Quality grades	E
Dimensions	Length	28-18
	Width	13.5 - 18.5
	Perch height	6 - 8.5
Use	Structural requirements [1].	Suitable for simple or reinforced non-supporting masonry with low axial compressive loads.
	Climatological requirements	Suitable only for mild climates with low rainfall
	Functional requirements	Not acceptable for externally visible walls without cladding.
Physical characteristics	Simple compressive strength; MPa, minimum	2
	Adhesion; MPa, minimum	0.15
	Water absorption %, maximum	24

For the execution of the mixture it will be manually weighed, with a proportion in percentage of 2.5% of fibre, with 30% of water, placed in a steel mould of 8x14x22 cm and subjected to pressure by means of a hydraulic press. It was demoulded and dried in the ambient conditions of the laboratory.

Stage 3. Mechanical test

This test was stipulated under the NMX-C-404-ONNCCE-2012 standard and was complemented with the Mexican standard NMX-C-036-ONNCCE which establishes the test method for the determination of compressive strength, which is based on the ASTM C-140-75 standard.

Sample analysis

The sample or specimen is tested in a universal testing machine (Figure 3), which must have sufficient capacity to operate at the specified loading rate without impact or loss of load. One of the blocks of the machine should have a hemispherical seat resting on the top of the specimen, while the other block should be rigid and provide a stable base for the specimen. It is essential to incorporate clamping or compression fittings that are rigid and correctly aligned. The centre of the sphere must coincide with the centre of the bearing surface with an appropriate tolerance to the radius of the sphere. The compression surfaces of the specimens must be flat, complying with a tolerance of 0,05 mm over a length of 150 mm taken in two orthogonal directions.

Box 4

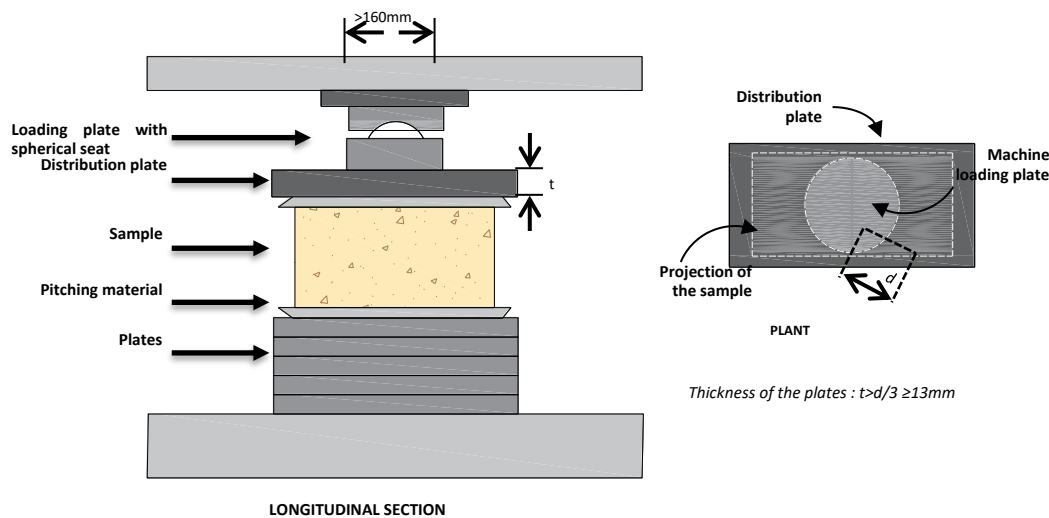


Figure 3

Compression test preparation Source: Own elaboration

Calculations

$$R = \frac{F}{A} \quad [1]$$

Where:

R Is the compressive strength in MPa (Kgf/cm^2)

F is the maximum load in N (Kgf)

A Is the cross-sectional area of the specimen (cm^2)

Results

XRD soil characterisation

Figure 4 presents the characterisation of the soil carried out by means of an X-Ray Diffraction (XRD) equipment using a copper X-ray source (Cu-K α), with an energy of 8.04 keV and an X-ray wavelength of 1.5406 Å. This technique allows detailed information to be obtained on the crystalline structure, composition and various physical properties of the analysed soil. In this case, the data obtained in the analysis show a 99% agreement with the CaCO₃ reference standard, which confirms that the sample is mainly calcium carbonate. This result indicates that the Ca²⁺ and CO₃²⁻ ions are in a 1:1 ratio, linked by an ionic interaction. From the database, it indicates that its crystalline structure is hexagonal, whose plane with the highest intensity corresponds to the 10

Box 5

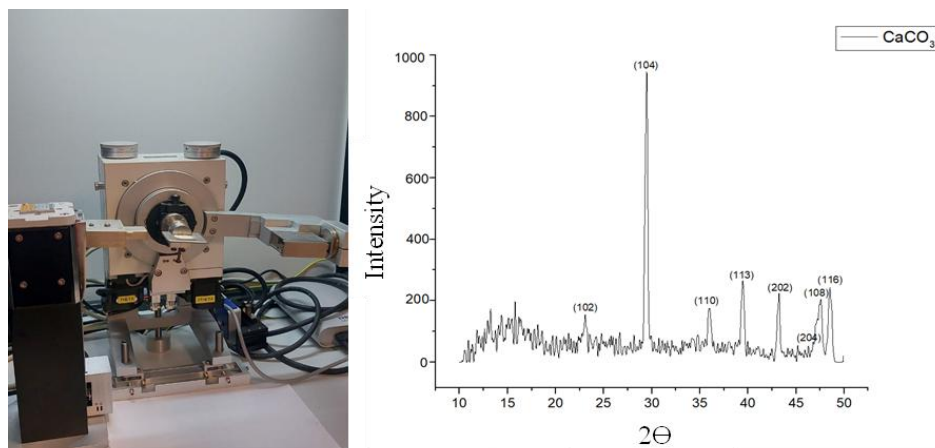


Figure 4

Characterisation by XRD

Source: *Own elaboration*

Sample

Prior to the mechanical compression test, the samples with 2.5% curd fibre content (figure 5) were analysed after 28 days, obtaining data such as: length, width, height and dry weight (table 2). The Mexican standard NMX-C-038- ONNCCE was used to obtain specific data for the block.

Box 6



Figure 5

Sample with 2.5% fibre

Source: *Own elaboration*

In table 2 we present the data of the analysed blocks, categorised as BASE, block or blank whose fibre percentage is equal to zero, while F1B1 2.5% refers to the block whose base is the sahcab and B1 the curd fibre, with 2.5% we refer to the percentage of aggregate. The pieces called F1B1 2.5% A, B, C, D are the sectioned pieces of a block.

Box 7

Table 2

Data obtained from samples under the NMX-C-038-ONNCCE standard

DATES	BASE	F1B1 2.5%	F1B1 2.5% A	F1B1 2.5% B	F1B1 2.5% C	F1B1 2.5% D
Length:	21.4cm	21.3cm	5.87cm	8.75cm	5.71cm	5.5cm
Width:	7.5cm	7.4cm	5.5cm	4.16cm	4.27cm	4.32cm
Height:	13.62	13.62	4.09	5.32	4.71cm	4.82cm
Weight:	3.950 kg	3.4 kg	.205 kg	.295 kg	.175 kg	.180 kg

Mechanical compression test

The samples are subjected to compression analysis in a universal machine, where the strength of the blocks is evaluated when they are compressed under a load. Because of the dimensions, the BASE and F1B1 2.5% samples are subjected to the preparation shown in figure 3, while the F1B1 2.5% A, B, C and D samples are tested directly from the spherical bearing plate. It is important to note that specimens A and B will be tested under the force of one direction of compression, while specimens C and D under another direction.

Box 8



Figure 4

Mechanical compression test

Source: *Own elaboration*

In table 3, we obtain the capacity of the blocks to withstand the compressive forces, the gross area was obtained from the data obtained in table 2, and the maximum load is the data obtained from the universal machine, which gives us a detailed report. With equation 1, we obtain the data on the compressive strength of the samples.

Box 9

Table 3

Data obtained from the mechanical test

Sample	Long (mm)	Width (mm)	Gross area (cm ²)	Carga Max. (Kg)	Kgf/cm ²
BASE	214	75	160.5	3070.91	19.1
F1B1 2.5%	213	74	157.6	2183.35	13.9
F1B1 2.5% A	58.7	55	32.3	360	11.1
F1B1 2.5% B	87.5	41.6	36.4	426.57	11.7
F1B1 2.5% C	57.1	42.7	24.38	396	16.2
F1B1 2.5% D	55	43.2	23.76	445.395	18.74

It is important to understand that each specimen was loaded to failure and showed unique behaviour during the test (figure 6). For example, sample BASE shows medium-sized cracks distributed throughout the block; as it does not contain fibre as an aggregate, the piece tends to fragment. In contrast, sample F1B1 with 2.5% fibre presents cracks in several parts of the block, but thanks to the addition of fibre, the block maintains its cohesion, avoiding a total detachment of the parts. In samples A, B, C and D, the cracks are larger; however, the fibre present in the mix prevents the sections from detaching, which reinforces the integrity of the material even after the appearance of cracks.

Box 10

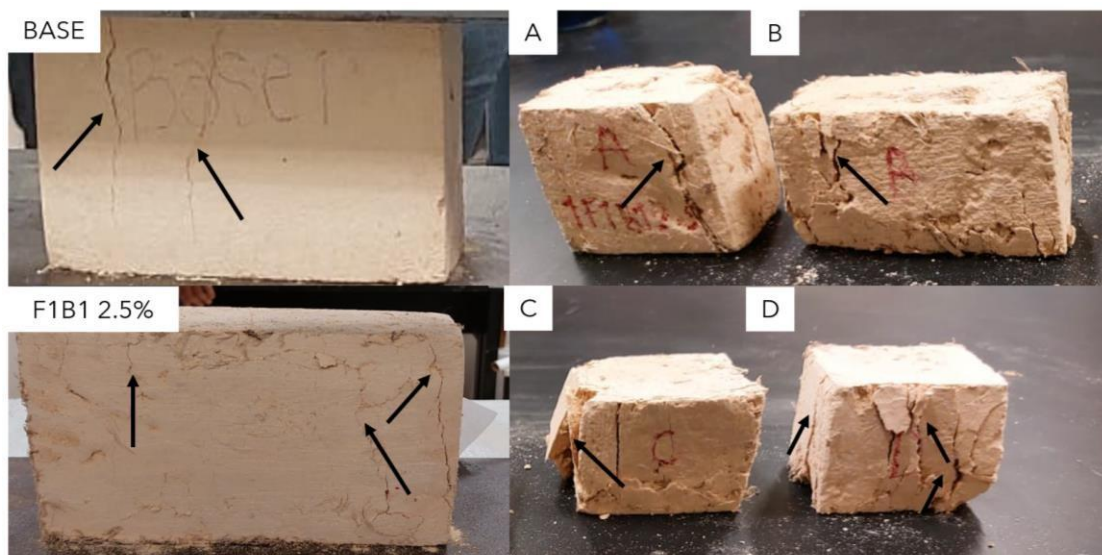


Figure 6

Samples after the failure

Source: *Own elaboration*

Conclusions

In conclusion, the results of this investigation and the data obtained from the compression tests reveal that the samples evaluated do not reach the minimum simple compressive strength parameter stipulated at 2 MPa (equivalent to 20.39 kg/cm²). The samples with a fibre content of 2.5% have a compressive strength range of 11.1 to 18.74 kg/cm², lower than the minimum required. In comparison, the base sample, without fibre content, achieves a slightly higher compressive strength of 19.01 kg/cm².

The compression test also reveals that the addition of fibre in the samples improves the cohesion of the material and its resistance to splitting, even after the appearance of cracks. This suggests that the use of fibre not only contributes to controlling the size and distribution of cracks, but also strengthens the material's ability to withstand loads and resist crumbling, holding together structurally in the face of failure.

The weight difference between the BASE specimen and the F1B1 specimen with 2.5% fibre is approximately 13.92%. This indicates that the incorporation of fibre at this rate contributes to a small reduction in raw material usage. These results suggest the addition of a percentage of cement for future research to meet the parameters set by the standard.

Statements

This chapter focuses on the manufacture and mechanical characterisation of the ecoblock, in compliance with the applicable national regulations. This research represents a key step towards reducing the environmental impact generated by the construction industry. The adoption of eco-friendly materials in this sector poses a significant challenge, as it requires the integration of technical, regulatory and scientific expertise to ensure their performance.

Conflict of interest

The authors declare that they have no conflicts of interest. They have no financial interests or personal relationships that could have influenced this book.

Authors' contribution

Muñoz-Talango, Dayana G.: conducted the experimental tests, interpreted the results and wrote the manuscript.

Abatal, Mohamed.: Conceptualisation of the research topic and review of results.

Santiago- de la Cruz, Arlette A.: Revision of the hand-written manuscript.

Availability of data and materials

Data are available on request from the lead author.

Funding

This research is not funded.

Acknowledgements

D. G. Muñoz thanks the Consejo Nacional de Humanidades, Ciencias y Tecnologías CONAHCYT for the national scholarship provided during the Master in Materials and Energy Engineering (MIME) at the Faculty of Engineering of the Universidad Autónoma del Carmen (UNACAR). To Dr. Mohamed Abatal for his guidance and help during this research. Also, to Dr. Juan Antonio Álvarez Arellano and Ing. Benjamín Mendoza Zavala, for their support in carrying out the compressive strength tests of this research.

Abbreviations

Ca	Calcium
CaCO ₃	Calcium carbonate
CO ₂	Carbon dioxide
CO ₃	Carbonate
cm ²	Square centimetres
EJ	Exajoules
Kgf	Kilogram-force
Kgf/cm ²	Kilogram-force per square centimetre

References

Background

Aghimien, D. O., Oke, A. E., & Aigbavboa, C. (2019). [Environmental Sustainability: Impact of Construction Activities.](#)

Fayomi, G. U., Mini, S. E., Fayomi, O. S. I., & Ayoola, A. A. (2019). [Perspectives on environmental CO₂ emission and energy factor in Cement Industry.](#) IOP Conference Series: Earth and Environmental Science, 331(1).

Hart, J. (2022). [Cement: Raising ambitions, reducing emissions.](#)

International Energy Agency, I. (2018). [Technology Roadmap - Low-Carbon Transition in the Cement Industry.](#)

López Ruiz, L. A., Roca Ramón, X., & Gassó Domingo, S. (2020). [The circular economy in the construction and demolition waste sector - A review and an integrative model approach.](#) In *Journal of Cleaner Production* (Vol. 248). Elsevier Ltd.

Müller, N., Harnisch, J., & Mesguen, J.-P. (2008). [A report prepared for the WWF-Lafarge Conservation Partnership On behalf of: WWF International Gland Switzerland How to Turn Around the Trend of Cement Related Emissions in the Developing World.](#)

Oberle, B., Bringezu, S., Hatfield Dodds, S., Hellwig, S., Schandl, H., Clement, J., & United Nations Environment Programme (2019). [Global resources outlook 2019 natural resources for the future we want.](#)

Basic fundamentals

Alonzo, S. L., Vinajera, R. C., & Rodríguez, R. G. (2006). [Granulometry of two predominant soil types in the state of Yucatán.](#)

Chen, L., Yang, M., Chen, Z., Xie, Z., Huang, L., Osman, A. I., Farghali, M., Sandanayake, M., Liu, E., Ahn, Y. H., Al-Muhtaseb, A. H., Rooney, D. W., & Yap, P. S. (2024). [Conversion of waste into sustainable construction materials: A review of recent developments and prospects.](#) In *Materials Today Sustainability* (Vol. 27). Elsevier Ltd.

Hellmuth, N. (2023). [Quajilote, \(Parmentiera acuelata\).](#)

Liu, T., Chen, L., Yang, M., Sandanayake, M., Miao, P., Shi, Y., & Yap, P. S. (2022). [Sustainability Considerations of Green Buildings: A Detailed Overview on Current Advancements and Future Considerations.](#) In *Sustainability (Switzerland)* (Vol. 14, Issue 21). MDPI.

Pacheco-Torgal, F., & Jalali, S. (2012). [Earth construction: Lessons from the past for future eco-efficient construction.](#) In *Construction and Building Materials* (Vol. 29, pp. 512-519).

Touré, P. M., Sambou, V., Faye, M., Thiam, A., Adj, M., & Azilinson, D. (2017). [Mechanical and hygrothermal properties of compressed stabilized earth bricks \(CSEB\).](#) *Journal of Building Engineering*, 13, 266-271.

Vicente, F. M., Güemes, V. N., Chanona, P. J. J., Perea, F. M. de J., Arzate, V. I., Quintero, L. A., & Sánchez, F. C. E. (2021). [Study of cellular architecture and micromechanical properties of cuajilote fruits \(Parmentiera edulis D.C.\) using different microscopy techniques.](#) *Microscopy Research and Technique*, 84(1), 12-27.

Supports

Scrivener, K. L., John, V. M., & Gartner, E. M. (2018). [Eco-efficient cements: Potential economically viable solutions for a low-CO₂ cement-based materials industry.](#) *Cement and Concrete Research*, 114, 2-26. <https://doi.org/10.1016/j.cemconres.2018.03.015>.

Steffens, F., Steffens, H., & Oliveira, F. R. (2017). [Applications of Natural Fibers on Architecture.](#) *Procedia Engineering*, 200, 317-324.

Tian, Q., Zhou, J., Hou, J., Zhou, Z., Liang, Z., Sun, M., Hu, J., & Huang, J. (2024). [Building the future: Smart concrete as a key element in next-generation construction.](#) In *Construction and Building Materials* (Vol. 429). Elsevier Ltd.

Differences

Hamada, H. M., Shi, J., Al Jawahery, M. S., Majdi, A., Yousif, S. T., & Kaplan, G. (2023). [Application of natural fibres in cement concrete: A critical review](#). *Materials Today Communications*, 35.

Discussion




Balasubramanian, M., Saravanan, R., & T, S. (2024). [Exploring natural plant fiber choices and treatment methods for contemporary composites: A comprehensive review](#). In *Results in Engineering* (Vol. 24). Elsevier B.V.

Jesudass, A., Gayathri, V., Geethan, R., Gobirajan, M., & Venkatesh, M. (2020). [Earthen blocks with natural fibres - A review](#). *Materials Today: Proceedings*, 45, 6979-6986.

Design for laser assembly in confocal Raman spectroscopy for *in-vivo* sample study

Diseño para ensamble láser en espectroscopía Raman confocal para estudio de muestras *in-vivo*

Urrieta-Almeida, Edgar*^a, Flores, Gil Aarón^b, Benavides, Olena^c and Bandala-Garces, Magdalena^d

^a  Universidad Autónoma del Carmen •  0000-0003-1668-1966 •  785442

^b  Universidad Autónoma del Carmen •  0000-0002-2302-2056 •  121166

^c  Universidad Autónoma del Carmen •  0000-0002-8124-0326 •  339830

^d  Universidad Autónoma del Carmen •  0000-0002-3102-3630

CONAHCYT classification:

DOI: <https://doi.org/10.35429/H.2024.13.48.56>

Area: Physics-Mathematics and Earth Sciences

Field: Physics

Discipline: Physical Chemistry

Subdiscipline: Molecular Spectroscopy

Key Handbooks

By visualising that the Raman spectroscopy technique has the versatility to be used to study *in-vivo* samples, such as, for example, the skin and fingernail of the human index finger. Another important fact is that humans have the same molecular conformation, but at different concentrations. This defines that a Raman spectrum is intrinsic to each individual, like a fingerprint. With these facts in mind, a laser assembly was implemented, which allows quality Raman spectra readings to be taken and thus a data bank to be created. The proposed assembly has the characteristics of allowing a sample to be taken in 10 minutes, without causing pain and without causing adverse effects to the skin. The aim is to identify biomarkers that will allow in the future a preventive or conclusive diagnosis in people with or without a diagnosis of chronic diseases through the processing of the database generated for each individual.

Citation: Urrieta-Almeida, Edgar, Flores, Gil Aarón, Benavides, Olena and Bandala-Garces, Magdalena. 2024. Design for laser assembly in confocal Raman spectroscopy for *in-vivo* sample study. 48-56. ECORFAN.

* ✉ [990615@mail.unacar.mx]

Handbook shelf URL: <https://www.ecorfan.org/handbooks.php>



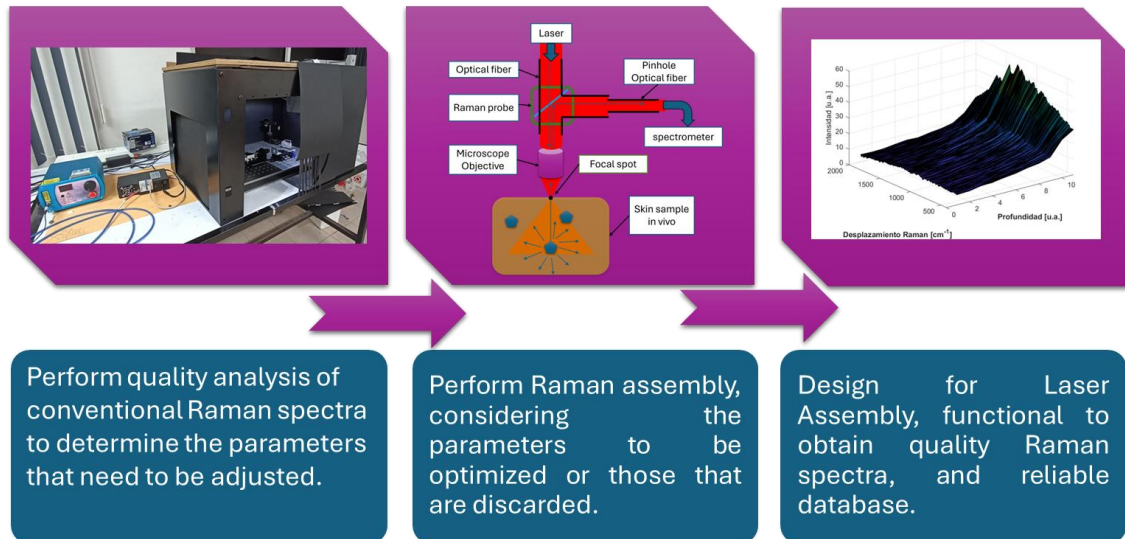
ISBN 978-607-8948-51-2/©2009 The Authors. Published by ECORFAN-Mexico, S.C. for its Holding Mexico on behalf of Handbook HRP. This is an open access chapter under the CC BY-NC-ND license [<http://creativecommons.org/licenses/by-nc-nd/4.0/>]

Peer Review under the responsibility of the Scientific Committee **MARVID**[®] in contribution to the scientific, technological and innovation Peer Review Process by training Human Resources for the continuity in the Critical Analysis of International Research.



Abstract

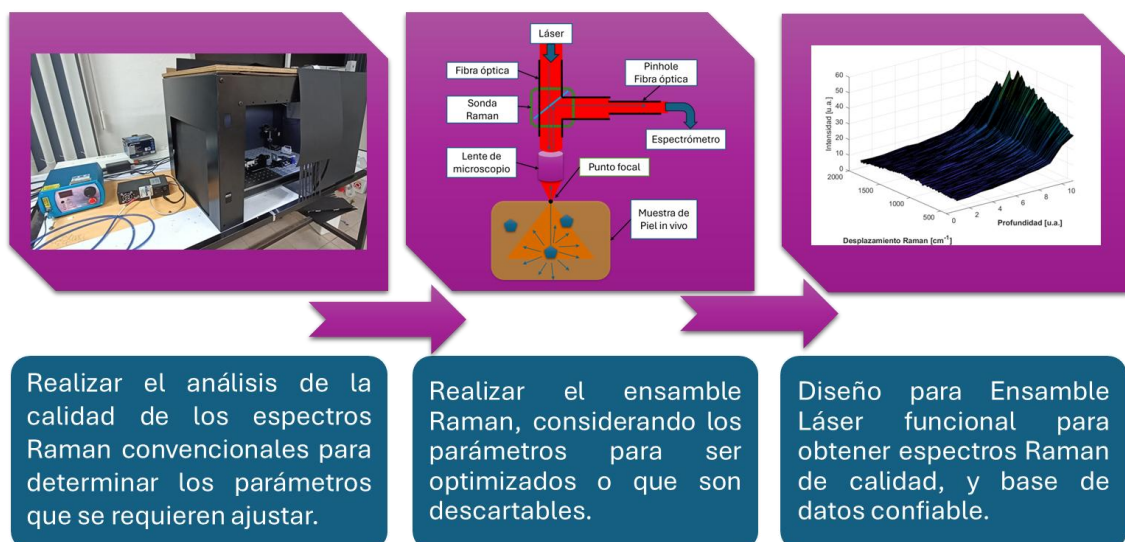
The study of biomarkers is a line of study that allows the early detection of abnormal biochemical processes, focusing on chronic human diseases such as diabetes, obesity, cancer, among others. Raman spectroscopy (RS) technology allows obtaining intrinsic data from a sample at the molecular level. RS allows studying biomarkers in biological samples *in vivo*, without contact, without pain, and in real time. This design for assembling a Confocal RS is presented, with a Raman laser equipment at 785 nm, a spectrometer QE65000 from Ocean-Optics, a microscope-type mount, and an optical fiber as a pin-hole. To validate the design, Raman bands of melanin, lipids and proteins are identified in spectral sampling at different depths, 1000 μm , in the fingerprint and index fingernail of a human volunteer. The design promises to obtain deconvolution spectra directly from the measurement in real time, without the need to apply numerical fitting methods in data processing.



Raman Spectroscopy, biomarcadores, Dedo índice, Muestras *in-vivo*

Resumen

Los biomarcadores son una línea de investigación, sobre la detección temprana de procesos bioquímicos anormales, enfocado a las enfermedades humanas crónicas, como la diabetes, la obesidad, el cáncer, entre otras. La Tecnología de espectroscopía Raman (ER) permite obtener datos intrínsecos de una muestra, al nivel molecular. La ER permite estudiar biomarcadores en muestras biológicas *in-vivo*, sin contacto, sin dolor, y en tiempo real. Se presenta un diseño para ensamble de un ER Confocal, con un equipo láser Raman a 785 nm, un espectrómetro QE65000 de Ocean-Optics, una montura tipo microscopio, y una fibra óptica como pin-hole. Para validar el diseño, se identifican las bandas Raman de melanina, lípidos y proteínas en el muestreo espectral a diferentes profundidades, hasta 1000 μm , en la huella y uña del dedo índice de un voluntario humano. El diseño promete obtener espectros en deconvolución directamente de la medición en tiempo real, sin aplicar métodos de ajuste numérico en el procesamiento de los datos.



Espectroscopia Raman, Biomarcadores, Dedo índice, Muestras *in-vivo*

Introduction

The study of public health problems is important for the Mexican society, especially for people who have problems in their quality of life. Considering the number of sick people and the number of chronic diseases registered, problems are generated in the socio-cultural and socio-economic development of the country. For example, Diabetes (NOM-015-SSA2-2010), Obesity, Cancer, which are known to have a great impact and generate social welfare problems (INEGI Communicated 2023). Chronic diseases such as cardiovascular diseases, hypertension, cancer, diabetes and also new conditions generated by the pandemic such as COVID-19. Each of these conditions represents a field of study for health science researchers in terms of prevention, diagnosis and treatment (INSP. 2023).

Raman spectroscopy (RS) has been used as a non-invasive method to study skin diseases and glucose between the Raman bands 1060 cm^{-1} and 1125 cm^{-1} (Flores A. et al. 2015), as well as haemoglobin 1549 cm^{-1} (Gonzales-Viveros et al. 2022). The methodology may be feasible for the study of blood glucose in vivo, for in vitro cases (N. Gonzales-Viveros et al. 2021). Likewise, with Raman equipment systems coupled to confocal microscopes (Shao. J et al. 2012), frequencies between 1168, 1531, 1463, 1021 cm^{-1} are also reported for diabetic blood samples (Firdous s. et al 2012) and studies in type 2 diabetes in blood samples (Gonzales-Solís et al 2018), under the condition of the American standard (ANSI) for type II lasers, which indicates that lasers with power lower than 100 mW on skin in humans should be used in experiments (American National Standards Institute 1993).

Raman spectroscopy (RS) is a technique that allows molecular information to be obtained from a material, in solid, liquid or gas state, whether organic or inorganic. Performing an ER analysis means shining a monochromatic beam of light on a sample and collecting the scattered light with a spectrograph. The light beam interacts with the molecular structure constituting the sample, causing changes in the vibrational state leading to changes in the frequency of the scattered light. The section of the scattered beam that contains the Raman information is known as inelastic scattering. The importance for analysing materials or substances is that the small frequency changes are specific and individual to each material (Smith, E. et al. 2005). With the proposed system and methodology it is expected to obtain detailed spectra on the molecular structures found on the skin of the fingerprint and the nail of the index finger.

Raman spectroscopy

The monochromatic light beam is incident on the sample, depending on the state of the sample there can be reflection, transmission, absorption and scattering. The scattering can be elastic or inelastic. It is the inelastic scattering that contains the information for ER. See Figure 1.

Box 1

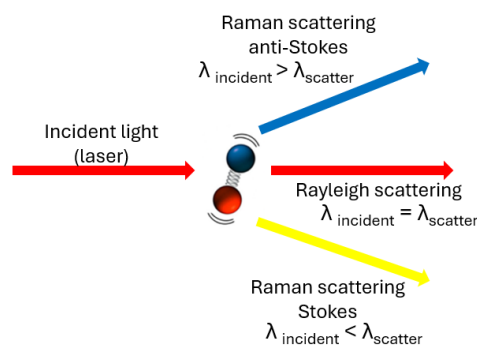


Figure 1

Incidence of a monochromatic light beam on a sample

Source: [Own elaboration]

A beam of light is a collection of photons, photons have energy according to the value of their frequency (where h is Planck's constant), photons interact with the molecular structure of the sample causing vibrational changes, the energy of an absorbed photon supplies that energy to move to a higher energy level which is called excitation. Upon loss of excitation, the molecule gives off a photon with a relatively different frequency from the incident beam (Drake G. et al. 2006).

While a molecule is in its ground state, a photon strikes and is absorbed, which inelastically excites the molecule to a higher virtual energy level. It then recoils to an energy level between the virtual level and the ground state, known as Raman Stokes, releasing a photon with a slightly different frequency and energy from the incident beam. If it returns from the virtual level to the ground state, this is called Rayleigh scattering. On the other hand, if the molecule is not initially in the ground state, when it moves to the excited state and returns to the ground state, it is called Anti-stokes scattering (Toporski, J. et al, 2018).

Raman changes depend on the natural frequency of vibration. The frequency depends on the mass of the molecule. For heavy molecule, it has long wavelength, low frequency and energy. For a light molecule, it has short wavelength, high frequency and energy. Complex molecules have a greater number of vibrational modes. Each molecule has its own natural frequency. The Raman spectrum is a fingerprint of molecules (Smith, E. et al. 2005).

Nail and skin anatomy

The spectra are sampled on the fingerprint and on the nail of the index finger. The epidermis is a compact cellular layer measuring 120-200 μm , with regional differences according to skin function. The dermis is 15-40 times thicker than the epidermis. The nail is 500-600 μm thick. In the present work, readings are being taken from the surface up to 10 internal steps of 127 μm , i.e. up to 1270 μm inside the footprint and nail (Conejo-Mir, J. et al. 2018). See figure 2 and 3.

Box 2

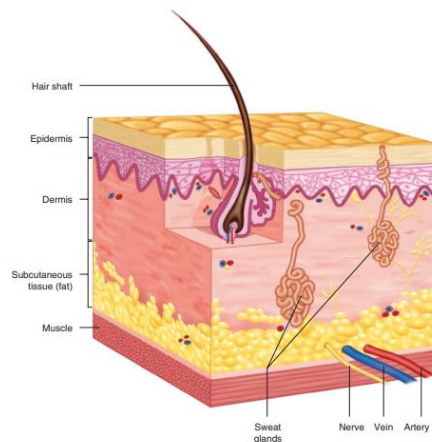


Figure 2

Anatomy of the skin

Source [Manual of Dermatology, ISBN: 978-84-7885-627-5]

Box 3

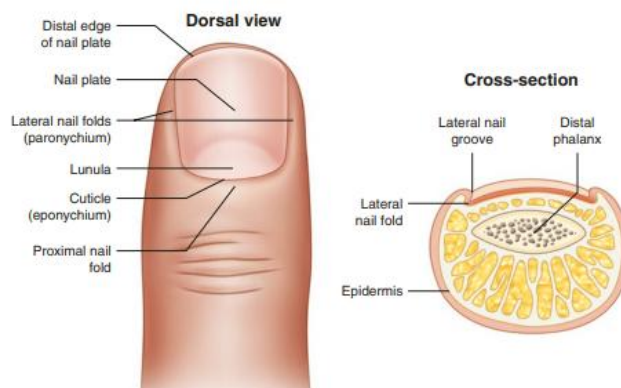


Figure 3

Anatomy of the nail

Source [Manual of Dermatology, ISBN: 978-84-7885-627-5]

Results

Confocal optical system development

In the present work, a unidirectional optical system was assembled to take Raman readings of the fingerprint of the index finger and the fingernail, in a first stage of healthy volunteers. Although it is worth commenting that this system could well be included in a CNC machine, such as the one used for industrial systems (Antonio, V. E., et. al 2023), as in the case of laser welding in the automotive industry (Yepes Mayoral, E. (2024), Thesis). But in our case, we need to take measurements at different depths inside the index finger, either at the front of the finger, or through the fingernail.

The optical system consists of the laser module at 785 nm, connected to a bifurcated optical fibre, with a 100-micron multimode fibre core, coupled to the laser, and a 200-micron multimode fibre coupled to the spectrometer, called a Raman probe whose tip has a focal length of 0.7 cm. The Raman signal is captured with the QE65000 spectrometer through the same probe. The 785 nm laser module is modulable in power, from 1 to 400 mW, and 50 mW was used for this project. The spectrometer allows Raman signals to be recorded in the spectral window of 400 - 2000 cm^{-1} , with a resolution of 4 cm^{-1} . The optical system also consists of an intermediate microscope lens between the probe and the sample, as well as a 50 micron fibre between the 200 μm fibre and the spectrometer. These two complements increase the resolution and reduce the laser spot, which reduces the power required. See Figures 4 and 5.

Principle of operation of the optical system

Figure 5: A schematic of how the focal plane shifts in a sample as it approaches the Raman probe is shown. An ER reading is taken for each displacement which is 127 μm .

Box 4



Figure 4

Raman spectroscopy system assembly

Source: [Own elaboration]

Sampling methodology

Activate the optical system, which are: Laser, spectrograph and computer equipment.

Set the software parameters, acquisition time in 5 s, 5 s average scanning time and level 3 filtering.

Clean the volunteer's index finger with alcohol to remove moisture and other impurities.

Place the area of the index finger, fingerprint or fingernail.

Locate the focal point on the surface of the area.

Collect the spectrum of the surface.

Reduce the distance of the moving base every $0.127\ \mu\text{m}$ to collect spectra for each displacement, up to a total of 11 spectra.

Save the data obtained in SpectraSuite software.

Box 5

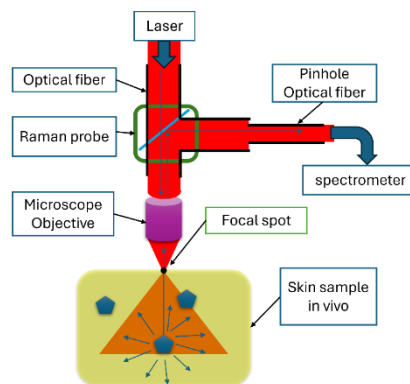


Figure 5

Raman spectroscopy system assembly

Source: [Own elaboration]

Processing of Raman spectra

The spectra obtained by the optical system are captured in digital form in a data file with the SpectraSuite software. The set of spectra is saved in a *.txt text file. The file name has the format date_time_name_region_notes. A comprehensive Matlab code was developed to automate the processing of the set of spectra to generate individual files and graphs in the format required for the comprehensive analysis. In general, the steps that the Matlab code executes are to trim the spectra in the range of 400 to $1800\ \text{cm}^{-1}$. The next step is to generate the attenuation plots, for each band specified in the code, and to perform the flat fitting of the spectra. The output files are, attenuation plot sorted by volunteer name with respect to sampling dates, flat-fit plot of the bands specified in the code, to perform deconvolution band analysis. The qualitative analysis of the bands of the set of Raman spectra is to determine differences in intensity, width, areas, shifts and deconvolution, which are significant for correlation with the inner layers being studied, of the volunteer's footprint and fingernail, see figure 6.

Box 6

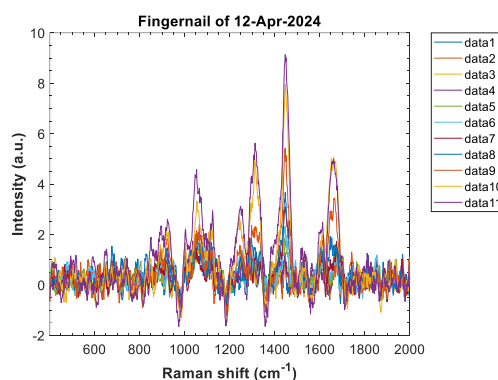


Figure 6

Flat-fit plot of a full spectral set of the nail.

Source: [Own elaboration]

The reliability of the spectral set obtained is qualitatively verified with the surface type graph, see figure 7. With which it is possible to visualise the exponential attenuation, as the focal point moves in the inner layers of the skin.

Box 7

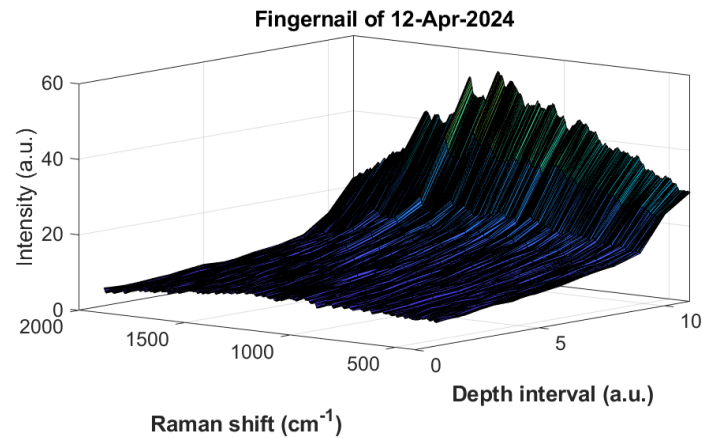


Figure 7

Surface type plot of the attenuation of the spectral array versus focal spot depth

Source: [Own elaboration]

In the spectral range from 1550 to 1750 cm^{-1} it is possible to visualise deconvolution peaks that have been obtained using the proposed methodology. The highest intensity peak measured at shallow levels, which is in the range of 1630 to 1700 cm^{-1} , is interpreted as the sum of the lower intensity peaks obtained at deep levels, which are the peaks at 1650 cm^{-1} , 1675 cm^{-1} , and the peak at 1700 cm^{-1} . See figure 8. This interval corresponds to the vibrations associated with melanin, the molecule that provides skin colouring (Wu et al., 2023).

This is the most substantial advance of the project since we have identified molecular components, it is necessary to continue with the interpretations of the spectral ranges for other species of molecules that are present in human skin.

Box 7

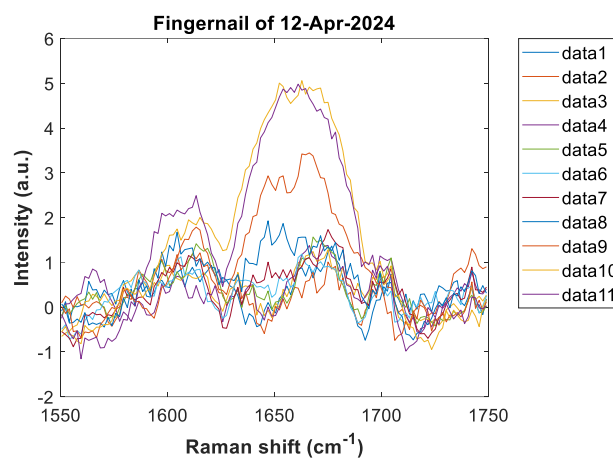


Figure 8

Flat-fit plot of a segment of the nail spectral array, from the range 1550-1750 cm^{-1}

Source: [Own elaboration]

Conclusions

The design of the confocal Raman system allows Raman spectra of the human index finger to be taken from different inner layers of the skin at different depths. This allows the following to be found:

- The integration time and power through the confocal system is reduced compared to standard Raman spectroscopy systems. This allows powers well below the ANSI international standard (100 mW). In our case, with a power of 25 mW and integration times of 25 seconds, spectra of good spectral quality are obtained.

- Systematic recording of Raman spectra of the skin, surface and internal, is possible. With displacements of 127 μm , reaching a depth of 1200 μm .
- The Raman spectra of fingerprint and fingernail show qualitative differences, i.e. there is no coincidence of Raman bands in both parts of the index finger, which implies studies of different molecular components (biomarkers) of the human.
- It was found that the intensity of the main Raman bands decay exponentially with depth, and that these bands actually deconvolute with sub-bands that may well be associated with biomarkers.
- The confocal system allows deconvolution of the spectra obtained for different depths.
- Deconvolution can allow the analysis of biomarkers that are not observable by standard Raman spectroscopy.
- The set of Raman spectra obtained are consistent, reproducible and intrinsic. Therefore, it is feasible to obtain correlations of the diversity of molecular components (biomarkers) with human physiological and pathological conditions.

Declarations

Conflict of interest

The author declares that he has no conflict of interest. He has no known competing financial interests or personal relationships that might have appeared to influence the article reported in this chapter.

Authors' contribution

Urrieta Almeida Edgar: Preparation of this paper.

Flores Gil Aarón, Benavides Olena, Bandala Garces Magdalena: Support in the development of the project and in the writing of the paper.

Availability of data and materials

The information contained in this document is available upon request from the lead author.

Funding

No funding was received.

Acknowledgements

Thanks are due to the PhD programme in engineering sciences of the Universidad Autónoma del Carmen and the CONAHCYT scholarship programme, and to the professors for their advice in the development of the project.

References

Background

Aarón Flores, Magdalena Bandala, Manuel May Olena Benavides, Lelio de la Cruz May, Jorge Luis Díaz López. (2015). Application of Raman spectroscopy to determine the presence of glucose in in vivo samples. SOMI.

Basics

American National Standards Institute ANSI (1993). American National Standards Institute Committee for Safe Use of Lasers Z136.1, New York, United States of America.

Conejo-Mir, J., Jiménez, J. C. M., & Martínez, F. M. C. (2018). Manual of dermatology. Grupo Aula Médica S.L. Vol. 1. 2018. ISBN 978-84-7885-637-4.

Drake, G. (Ed.) (2006). [Springer Handbook of Atomic, Molecular, and Optical Physics](#). Springer New York.

INEGI, Statistics on registered deaths. Press release no. 29/23. January to June 2022. INEGI (2023)

INSP. National Institute of Public Health. Programa Anual de Trabajo 2021. Mexico: INSP; 2023.

Prevention, treatment and control of diabetes mellitus. Norma oficial mexicana NOM-015-SSA2-2010. Diario oficial, Secretaría de Salud, 23 November 2010.

Smith, E., & Dent, G. (2005). [Modern Raman spectroscopy: A practical approach](#). J. Wiley.

Toporski, J., Dieing, T., & Hollricher, O. (Eds.). (2018). [Confocal Raman Microscopy](#) (Vol. 66). Springer International Publishing.

Support

Wu, D., Kukk, A. F., & Roth, B. (2023). [Detection of melanin influence on skin samples based on Raman spectroscopy and optical coherence tomography dual-modal approach](#). Journal of Biophotonics, 16(8), e202300080.

Firdous, S., Nawaz, M., Ahmed, M. et al. [Measurement of diabetic sugar concentration in human blood using Raman spectroscopy](#). Laser Phys. 22, 1090-1094 (2012).

González-Solís, J.L., Villafan-Bernal, J.R., Martínez-Zérega, B.E. et al. [Type 2 diabetes detection based on serum sample Raman spectroscopy](#). Lasers Med Sci 33, 1791-1797 (2018).

González-Viveros, N., Castro-Ramos, J., Gómez-Gil, P. et al. [Quantification of glycated hemoglobin and glucose in vivo using Raman spectroscopy and artificial neural networks](#). Lasers Med Sci 37, 3537-3549 (2022).

Shao, J., Lin, M., Li, Y., Li, X., Liu, J., Liang, J. & Yao, H. (2012). In Vivo Blood Glucose Quantification Using Raman Spectroscopy. PLoS ONE 7(10): e48127, October 25.

Discussions

N. González-Viveros. PhD Thesis, Quantification of glycosylated haemoglobin and glucose in vivo using Raman spectroscopy and artificial neural networks. PhD thesis. National Institute of Astrophysics, Optics and Electronics (2021).




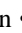
Antonio, V. E., Kimberly, D. T., Daniel, F. V., Guadalupe, S. V. M., & Francelin, D. D. [Construction of a CNC laser machine](#). [Construction of a CNC laser machine](#), Revista de Ingeniería y Tecnologías para el Desarrollo Sustentable 11 (2023) 67 - 71.


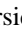
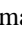
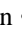
Yepes Mayoral, E. (2024). [Analysis and design of the connection of busbars in automotive inverters](#). Universidad Rey Juan Carlos.


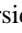
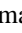
Evaluation of sinkholes in a civil work by capturing digital images using an unmanned aerial vehicle


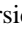
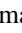
Evaluación de socavones en una obra civil mediante la captura de imágenes digitales utilizando un vehículo aéreo no tripulado

Pavón-Moreno, Julio^a, Escorza-Reyes, Marisol^b, Vergara-Huerta, Filiberto^c and Canto-Pérez, Emily^d

^a  Universidad Autónoma del Carmen •  3401-2024 •  0009-0004-9576-5547 •  376671

^b  Universidad Autónoma del Carmen •  1427-2022 •  0000-0002-7289-1004 •  376684

^c  Universidad Autónoma del Carmen •  0009-0002-3213-7020 •  392763

^d  Universidad Autónoma del Carmen •  6292-2024 •  0009-0001-4278-1971

CONAHCYT classification:

DOI: <https://doi.org/10.35429/H.2024.14.57.68>

Area: Physics - Mathematics and Earth sciences

Field: Mathematics

Discipline: Statistics

Sub-discipline: Data analysis

Key Handbooks

The main contribution of this research lies in the implementation of a drone for the acquisition of high-resolution aerial images and their subsequent processing to identify, quantify and characterise damage to the surface of a civil work with great precision. Particularly, in this study it was used for the study of sinkholes in the perimeter surface of a dock manoeuvring area, however, the method is applicable to the assessment of the state of any infrastructure and the early detection of possible damage, which allows intervention and maintenance plans to be made, reducing costs and study times. Among the key aspects of this study is the definition of the acquisition parameters that control the resolution of the images and their relationship with the size of the objects to be studied. By analysing high-resolution aerial images obtained with an unmanned aerial vehicle, 99 sinkholes in the civil works were identified and quantified, with an acceptable margin of error. The results suggest that the formation of these sinkholes is directly related to inadequate structural design, aggravated by natural factors and human activities.

Citation: Pavón-Moreno, Julio, Escorza-Reyes, Marisol, Vergara-Huerta, Filiberto and Canto-Pérez, Emily. 2024. Evaluation of sinkholes in a civil work by capturing digital images using an unmanned aerial vehicle. 57-68. ECORFAN.

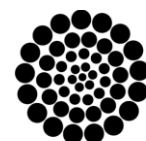
* ✉ [\[lcol@cicy.mx\]](mailto:lcol@cicy.mx)

Handbook shelf URL: <https://www.ecorfan.org/handbooks.php>



ISBN 978-607-8948-50-5/©2009 The Authors. Published by ECORFAN-Mexico, S.C. for its Holding Mexico on behalf of Handbook HRP. This is an open access chapter under the CC BY-NC-ND license [<http://creativecommons.org/licenses/by-nc-nd/4.0/>]

Peer Review under the responsibility of the Scientific Committee **MARVID**[®] in contribution to the scientific, technological and innovation Peer Review Process by training Human Resources for the continuity in the Critical Analysis of International Research.




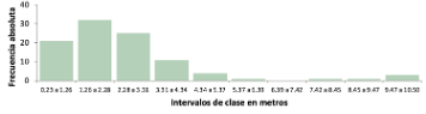

RENIECYT

Registro Nacional de Instituciones y
Empresas Científicas y Tecnológicas

1702902 CONAHCYT

Abstract


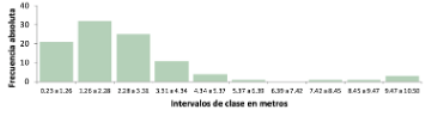

This paper presents the results of a study carried out in a civil work located in a port of Ciudad del Carmen, Campeche, to detect the formation of sinkholes and quantify their dimensions using high-resolution aerial digital images acquired with an unmanned aerial vehicle at 60 m elevation and using 20 control points on site. Digital images were analyzed with ImageJ software to quantify and characterize the shape of the sinkholes in the civil work. Descriptive statistics were performed on the dimensions of the sinkhole structures identified, both in the field and in the digital images, to later compare the results obtained and evaluate the validity of the dimensions obtained from them. Likewise, a calculation of the percentage of damage in the perimeter was performed. The mean square and percentage errors were 0.03 m² and 13%, respectively, which can be attributed to climatic factors during the acquisition of the images and the inherent limitations of the technique. 99 sinkholes were detected in the perimeter of the civil works, whose morphology and distribution suggest an origin related to an inadequate structural design of the retaining wall, aggravated by natural factors such as erosion and marine currents, as well as by anthropogenic activities such as heavy vehicle traffic. This research highlights the importance of implementing long-term monitoring programs based on remote sensing techniques.

<ul style="list-style-type: none"> Quantify and characterize sinkholes in a civil work. Structure damage analysis. 	<ul style="list-style-type: none"> Acquisition of aerial photographs and control points. Descriptive statistics and damage analysis. 	<ul style="list-style-type: none"> Identification of damage in a civil work with digital images. 
---	--	--

Structure, Anthropogenic, Morphology

Resumen

En este trabajo se presentan los resultados de un estudio realizado en una obra civil ubicada en el Puerto Pesquero de Ciudad del Carmen, Campeche, con la finalidad de detectar la formación de socavones y cuantificar sus dimensiones utilizando imágenes digitales aéreas de alta resolución adquiridas con un vehículo aéreo no tripulado a 60 m de elevación y utilizando 20 puntos de control en el sitio. Las imágenes digitales fueron analizadas con el software ImageJ para cuantificar y caracterizar la forma de los socavones en la obra civil. Se realizó la estadística descriptiva de las dimensiones de las estructuras de daño identificadas, tanto en campo como en las imágenes digitales, para posteriormente realizar la comparación entre los resultados obtenidos y evaluar la validez de las dimensiones obtenidas a partir de estas. De igual forma, se realizó el cálculo de porcentaje de daño en el perímetro. Los errores cuadrático medio y porcentual fueron de 0.03 m² y 13%, respectivamente, que pueden atribuirse a factores climáticos durante la adquisición de las imágenes y las limitaciones inherentes de la técnica. Se detectaron 99 socavones en el perímetro de la obra civil, cuya morfología y distribución sugieren un origen relacionado con un diseño estructural inadecuado del muro de contención, agravado por factores naturales como la erosión y las corrientes marinas, así como por actividades antrópicas como el tránsito de vehículos pesados. Esta investigación destaca la importancia de implementar programas de monitoreo a largo plazo basados en técnicas de teledetección.

<ul style="list-style-type: none"> Cuantificar y caracterizar socavones en una obra civil. Análisis de daño de la estructura. 	<ul style="list-style-type: none"> Adquisición de fotografías aéreas y puntos de control. Estadística descriptiva y análisis de daño. 	<ul style="list-style-type: none"> Identificación de daño en una obra civil con imágenes digitales. 
---	---	--

Estructura, Antropogénica, Morfología

Introduction

Sinkholes are geological depressions that occur when cavities in the subsoil collapse and can range in size from small cracks to large craters, and usually occur suddenly. They can arise from both natural processes and anthropogenic activities, including pipeline leaks, urban development, mining, among others.

The formation of sinkholes in karst environments is common and their origin is due to the dissolution of limestone rocks by seepage of fresh water or sewage (. Other natural causes of sinkhole formation are related to tectonic factors, such as fault displacements, fractures and vibrations produced by earthquakes.

The formation of sinkholes in urban areas and the involvement of civil works will depend on the natural and anthropogenic factors that are present, as well as the particular characteristics of the physical infrastructure affected. Sinkholes have been found to be closely related to groundwater overexploitation because the lowering of the water table creates a cone of depression that causes changes in the fluid pressure in the subsoil, leading to elastic and inelastic compaction, the latter causing the formation of voids.

In coastal areas, sinkholes can additionally be formed by the dynamics of sea currents and groundwater, as well as by extreme events such as storm surges, among others, causing damage to civil structures. However, the causes of damage to coastal civil works can also be associated with inadequate design. describes the occurrence of a sinkhole in a harbour due to poor design of the perimeter walls, where a section was shortened to relocate electricity supply cables.

The study of the physical integrity of civil works can be carried out using different techniques. They can be invasive (boreholes, borings, drilling, pitting, trenching, sampling and testing) and non-invasive (geophysical, aerial or satellite remote sensing), the latter being very useful in complex and difficult to access environments. In the context of sinkhole formation, the use of remotely sensed imagery and digital aerial imagery is restricted by its dimensions, making scale a critical factor; the resolution required for the detection of relatively small subsidence features (1.5 ± 3.0 m wide) comes from aerial imagery with scales between 1: 25,000 and 1: 10,000, although digital imagery from unmanned aerial vehicles now achieves high resolutions, making it possible to identify centimetre-sized objects.

In addition, recent studies are using interferometric synthetic aperture radar (InSAR) and photogrammetry for more precise measurements of sinkholes. To study these images, it is possible to use complex algorithms such as convolutional neural networks, including U-net , or more affordable techniques such as image analysis with ImageJ.

This paper analyses the formation of sinkholes in a civil engineering site in the port area of Ciudad del Carmen, Campeche (Figure 1), which represents a particular risk to infrastructure and economic activities in the region. Understanding the formation of sinkholes and their risks is crucial for urban planning and infrastructure safety.

Box 1**Figure 1**

Formation of a sinkhole with collapsed asphalt layer in a port civil works, Ciudad del Carmen, Campeche

Source [Own elaboration]

Furthermore, the study of sinkholes in urban contexts is fundamental in the identification of vulnerable areas and the implementation of preventive measures to protect not only infrastructure but also human lives, contributing to urban planning, land management and avoiding urban development in risk areas. Furthermore, sinkhole research is crucial to understand the natural and anthropogenic processes that trigger their formation and to develop accurate models for the prediction of their occurrence.

The added value of the present research lies in the combination of innovative, easily accessible and lower cost techniques (drones and specialised software) compared to traditional methods, to obtain a detailed characterisation of sinkholes and identify areas of higher risk. This information is essential for informed decision making in terms of management and mitigation of the problem.

Specifically, the study carried out in a dock of the fishing port of Ciudad del Carmen, Campeche, has employed a methodology that combines remote sensing techniques with an unmanned aerial vehicle for the capture of high-resolution digital images and statistical analysis, with the aim of characterising and quantifying the sinkholes present in the area. The results obtained have made it possible to identify critical areas with a higher frequency of sinkhole formation, and although further research is required to establish causality with greater certainty, it is possible to suggest some relevant factors in their formation, both natural and anthropogenic, which have been added to the high traffic and manoeuvres within the civil works. The study also lays the groundwork for more detailed future research, which should include geophysical analysis, numerical modelling and long-term monitoring, with the aim of understanding the mechanisms of sinkhole formation and developing effective mitigation strategies.

Methodology

During May and June 2023, two visits were made to the civil works under study. During the first visit, an inspection of the civil works site was carried out to identify the areas with the greatest presence of sinkholes, as well as to collect information on the dimensions of 20 randomly distributed sinkholes around the perimeter. The first visit mentioned that the shape of the sinkholes is usually conical, where the wide end opens at the surface, and is of variable shape, while the narrow end is located at the bottom (Figure 2). The depth of sinkholes can range from a few centimetres to more than several metres deep, and this parameter is measured from the ground surface, regardless of whether the cover is natural or artificial. In the present study, the dimensions of the selected control points were quantified by approximating an ellipse on the surface, with a major axis (parallel to the perimeter of the civil structure) and a minor axis (perpendicular to the major axis).

Although some voids were similar in shape to those described by the author, for practical purposes, the depth was not estimated in this study due to the variability of this parameter in the same void.

Box 2

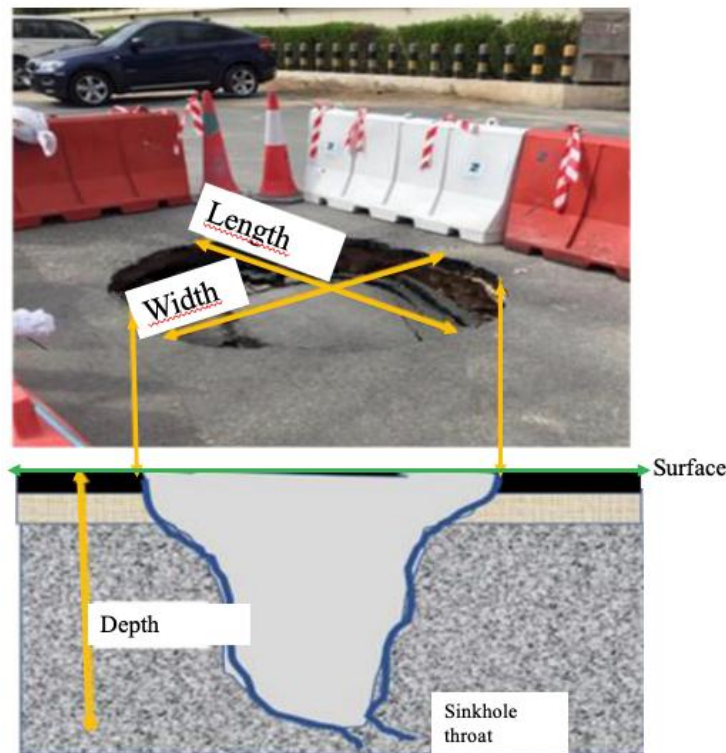


Figure 2

Measurement of the dimensions of an undercut

Source: [Modified from *Essa Al-Ansari et al. (2023)*]

In the second visit to the study site, the acquisition of digital aerial images was carried out, focusing the investigation on the perimeter of the dock due to the initial identification of a greater presence of sinkholes in this area compared to the central area. The acquisition of the digital images was carried out with a DJI Mini 2 commercial drone, without vehicle movement in each shot and at a height of 60 m, taking into consideration that the sinkholes could be identified in at least two different images. The drone's camera has a resolution of 12 megapixels, focal length of 4.49 mm, sensor size 1/2.3 inches and in all shots it was positioned vertically. In addition, the acquisition of the digital images was performed around noon, with moderate cloud conditions and winds reported for the locality between 5.6 and 13 km/h.

The analysis of the undercuts was developed by processing the aerial digital images in ImageJ software (*Schneider et al., 2012*), with the aim of 1) mapping the totality of the surface exposed structures, 2) identifying the areas with the highest number of undercuts and 3) digitally quantifying the surface dimensions of the undercuts and their dimensions were estimated through the approximation of a surface ellipse, extracting the lengths of the major and minor axes of the same structure in two different shots and calculating their average.

In order to carry out a quality control of the measurements obtained in the images, the mean square error and the percentage error were estimated, taking as a reference the measurements obtained from the 20 undercuts of the reconnaissance visit to the site.

On the other hand, the calculation of the eccentricity of the cross-sectional areas of the undercuts and the percentage of structures with eccentricities above different thresholds was carried out.

Subsequently, descriptive statistics of the dimensions of the undercuts were developed and frequency histograms were elaborated. Similarly, the percentage of damage to the perimeter of the study site was estimated, considering the length of the major axis of the structures as the damaged perimeter, given that most of the undercuts are oriented with this axis parallel to the perimeter. In addition, the count of sinkholes per perimeter line (Figure 3) and the assignment of the orientation of the axis that is parallel to the perimeter was carried out, to finally determine the percentage of damage in each line of the perimeter in order to detect areas with greater damage.

Box 3



Figure 3

Location of the perimeter lines of the civil works.

Source [own elaboration]

Results

The results of the comparison between the dimensions of the undercuts obtained in situ and in the aerial images indicate a mean square error of 0.03m^2 and a percentage error of 12.67%, both errors are considered low given the average size of the major axis of the characterised structures. The errors can be associated to different causes, mainly to the resolution of the acquired aerial images, which is related to the flight altitude and weather conditions during the acquisition, which makes it difficult to achieve a correct stability and positioning of the camera, resulting in complications when identifying the edges of the structures to be characterised in some images.

Box 4



Figure 4

Location of the sinkholes on the perimeter of the dock under study

Source [Own elaboration]

The analysis of the digital images identified 99 shallowly exposed sinkholes (Figure 4), whose dimensions for the major axis range from 0.23 to 10.50 m, with an average of 2.56 m and a standard deviation of 1.97 m, while the minor axis measurements show an average of 1.31 m and a standard deviation of 0.70 m (Table 1).

Box 5

Table 1

Descriptive statistics on the dimensions of undercuts

	Minimum	Maximum	Medium	Average	Standard deviation
Major axis (m)	0.23	10.50	2.10	2.56	1.97
Minor axis (m)	0.23	3.68	1.18	1.31	0.70
Surface area (m ²)	0.04	20.62	2.11	3.11	3.42
Eccentricity (A)	0	0.99	0.82	0.75	0.24

Source [Own elaboration]

Likewise, it is identified that the highest frequency of occurrence for the length of the major axis is found in the interval from 1.26 to 3.31 m, with 53% of the total number of sinkholes within this size (Figure 5), and for the length of the minor axis, the most frequent classes are found in the intervals between 0.23 and 1.96 m, grouping 83% of the total number of sinkholes in this range (Figure 6). The areas of the undercuts are in the range of 0.04 and 20.62 m², with an average of 3.11 m² and with a higher occurrence of those with areas smaller than 4.16 m² (79%, Figure 7).

Box 6

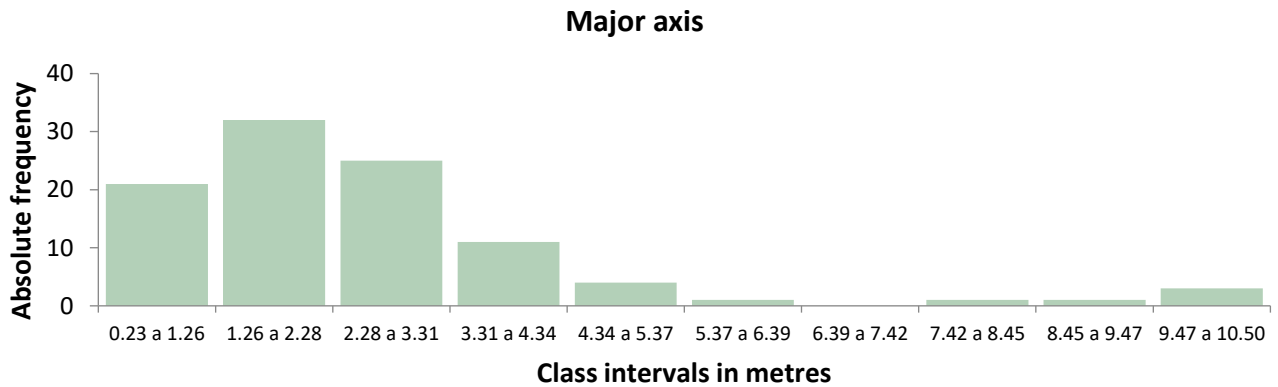


Figure 5

Histogram of absolute frequency of major axis of sinkholes identified in the basin under study

Source [own elaboration]

Box 7

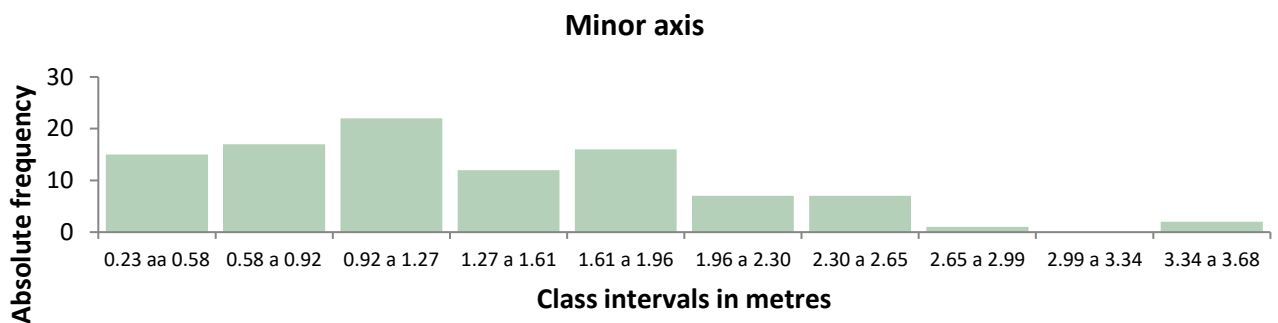


Figure 6

Histogram of absolute frequency of minor axis of sinkholes identified in the basin under study

Source [own elaboration]

Box 8

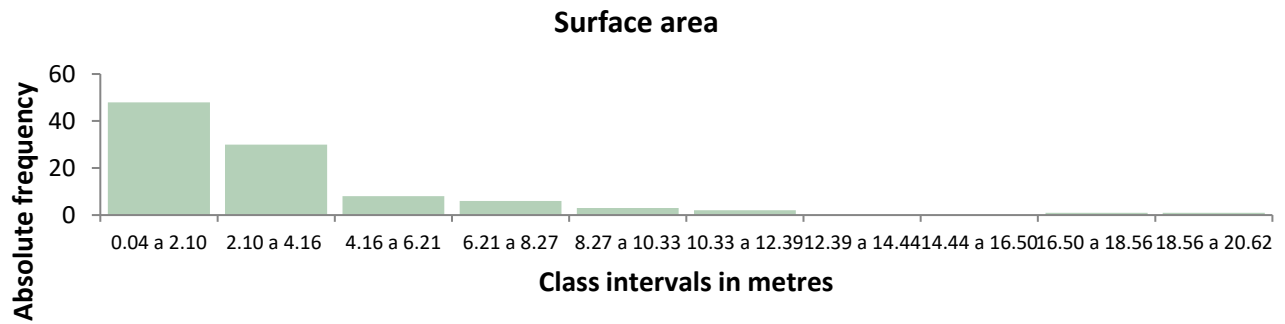


Figure 7

Absolute frequency histogram of the surface area of sinkholes identified in the basin under study

Source [own elaboration]

On the other hand, the analysis of the eccentricities of the surface areas of the undercuts indicates that most of them have highly eccentric shapes. The average for this parameter is 0.75 with a standard deviation of 0.24. In addition, 87% of them were identified as having values equal to or greater than 0.5 and 58% with values greater than 0.7 (Table 2). Similarly, of all the undercuts, 80% are found with the major axis oriented parallel to the perimeter, 9% with the minor axis parallel to the perimeter and 11% have similar lengths between the major and minor axes.

Box 9

Table 2

Percentage of undercuts with eccentricities greater than one value

	Minimum	Maximum	Medium	Average	Standard deviation
Major axis (m)	0.23	10.50	2.10	2.56	1.97
Minor axis (m)	0.23	3.68	1.18	1.31	0.70
Surface area (m ²)	0.04	20.62	2.11	3.11	3.42
Eccentricity (A)	0	0.99	0.82	0.75	0.24

Source [own elaboration]

The analysis of perimeter damage due to the formation of sinkholes indicates that 27.72% of the perimeter was affected. In addition, the analysis of the percentage of damage in each line of the perimeter shows that this is greater in line 1 and 2, with 48.87% and 37.62%, respectively, and with a greater average shaft size than the global average (Table 3).

Box 10

Table 3

Analysis of damage caused by sinkholes in the perimeter of the study basin

Perimeter line no.	Longitud (m)	Rumbo	No. of sinkholes	Average length of major axis	Standard deviation	Percentage of perimeter with damage (%)
1	106.32	N68.4°E	10	5.20	2.82	48.87
2	435.45	N33.6°W	59	2.78	1.69	37.62
3	198.67	N36.7°E	23	1.29	0.62	14.94
4	177	N52.4°W	7	1.10	1.18	4.34

Source [own elaboration]

The causes of the formation of the sinkholes and the damage identified at the site can be associated with various natural and anthropic factors, such as coastal erosion, sea currents and vibrations produced by waves, maritime traffic, heavy machinery and other factors inherent to the structures. At the same time, it is important to point out that the damage to the perimeter of the dock may be aggravated by the high traffic of heavy vehicles and machinery that carry out loading and unloading manoeuvres, together with the vehicles that pass through on a daily basis due to the activities inherent to the port.

The results of the characterisation of the sinkholes, i.e. their size, shape, location, orientation and frequency of occurrence, suggest that the main control of their formation is related to the inadequate design of the civil works, particularly the perimeter retaining wall, and the damage is increased by the natural and anthropic factors to which it is exposed. In this regard, a study of sea currents is recommended in the design of this type of civil structures, in order to estimate the maximum stresses to which they will be subjected, as well as to consider future scenarios of rising sea levels and other effects associated with climate change, given that a rising sea level implies an increase in the magnitude of the stresses on the retaining walls. Similarly, a monitoring of environmental vibrations would provide relevant information for the rethinking of port manoeuvres and activities, in order to avoid further damage to the structure, giving a guideline to carry out the necessary actions to solve the problem of damage faced by the perimeter of the dock.

On the other hand, the high eccentricities found in the shape of the sinkholes indicate that immediate attention is required in terms of the operability of the basin, as there are important implications for the stability of the terrain. Sinkholes with cross-sectional areas with low eccentricity values will allow stresses on the surrounding ground to be more evenly distributed around the cavity, which may suggest greater stability, while those with more eccentric shapes will concentrate stresses at the narrower ends, decreasing stability and increasing the risk of collapse.

Complementary studies are necessary for the identification of unexposed voids, particularly with geophysical methods since, during the reconnaissance visit, voids were identified adjacent to the exposed voids on the surface but still covered by the asphalt layer. In addition, geophysical surveys would provide relevant information on the formation process of the sinkholes. Continuous monitoring of the civil structure, particularly the retaining wall, is also recommended in order to detect any signs of deterioration and take corrective measures in time.

Finally, it should be noted that given the dimension of the problem at the site at the time of the study, the sinkholes were constantly filled with granular materials of different sizes and the most affected perimeter has been delimited to avoid overloading the civil structure.

Conclusions

99 sinkholes of varying dimensions were identified with the analysis of digital images obtained with an unmanned aerial vehicle and validated with 20 control points.

A mean square error of 0.03m^2 and a percentage error of 12.67% were obtained between the control points and the dimensions extracted from the digital images, associated with the non-ideal environmental conditions during the acquisition. This error can be reduced by performing the digital image acquisition under more appropriate environmental conditions, particularly with lower wind speeds.

Statistical analysis of the surface morphology of the sinkholes, as well as their location and frequency of occurrence, suggest that the origin of their formation is related to the inappropriate design of the wall on the perimeter of the dock, the damage being increased by the natural and anthropic factors to which it is exposed, particularly on the perimeter lines that have a greater activity of manoeuvres and traffic of vehicles and heavy machinery.

It is necessary to carry out complementary studies using geophysical methods to identify unexposed sinkholes and the physical characteristics of the subsoil at depth, as well as marine currents and groundwater, in order to provide more information on the causes of their formation.

Regular monitoring of the civil structure with the implementation of automated techniques for damage detection is also recommended.

Declarations

Conflict of interest

The authors declare that they have no conflicts of interest. They have no financial interests or personal relationships that could have influenced this book.

Authors' contributions

Pavón-Moreno, Julio: Original drafting, data acquisition and revision.

Escorza-Reyes, Marisol: Original drafting, statistical analysis and review.

Vergara-Huerta, Filiberto: Data processing and review.

Canto-Pérez, Emily: Data acquisition and review.

Availability of data and materials

The information contained in this paper is available on request from the lead author.

Funding

No funding was received.

Acknowledgements

We are grateful to the Administración Portuaria Integral de Ciudad del Carmen, Campeche, for providing access to their facilities and transport resources for the development of this research.

Abbreviations

DJI Da-Jiang Innovations

References

Basics

Alrowaimi, M., Chopra, M., Yun, H.-B., & Mokhtari, S. (2020). [Experimental Study of Sinkhole Failure Related to Groundwater Level Drops](#). *Journal of Testing and Evaluation*, 48(6), 20180064.

Bokhari, R., Shu, H., Tariq, A., Al-Ansari, N., Guluzade, R., Chen, T., Jamil, A., & Aslam, M. (2023). [Land subsidence analysis using synthetic aperture radar data](#). *Heliyon*, 9(3).

Busetti, A., Leone, C., Corradetti, A., Fracaros, S., Spadotto, S., Rai, P., Zini, L., & Calligaris, C. (2024). [Coastal Storm-Induced Sinkholes: Insights from Unmanned Aerial Vehicle Monitoring](#). *Remote Sensing*, 16(19), 3681.

Chen, Y., Guo, L., Xu, J., Yang, Q., Wang, H., & Zhu, C. (2024). [Monitoring and Cause Analysis of Land Subsidence along the Yangtze River Utilizing Time-Series InSAR](#). *ISPRS International Journal of Geo-Information*, 13(7).

Forcael, E., Román, O., Stuardo, H., Herrera, R. F., & Soto-Muñoz, J. (2024). [Evaluation of Fissures and Cracks in Bridges by Applying Digital Image Capture Techniques Using an Unmanned Aerial Vehicle](#). *Drones*, 8(1).

Fujii, Y., Shogaki, T., & Miyakawa, M. (2018). [Photogrammetric documentation and non-invasive investigation of a stone dry dock, the Yokosuka Arsenal dry dock No. 1, Japan](#). *Engineering Geology*, 234, 122-131.

Intrieri, E., Confuorto, P., Bianchini, S., Rivolta, C., Leva, D., Gregolon, S., Buchignani, V., & Fanti, R. (2023). [Sinkhole risk mapping and early warning: the case of Camaiole \(Italy\)](#). *Frontiers in Earth Science*, 11.

Jiang, X., Zhou, W., Guang, Z., Pan, Z., & Ma, X. (2023). [Analysis of sinkholes in a karst area adjacent to three mines in south China](#). *Discover Water*, 3(1).

Lee, E. J., Shin, S. Y., Ko, B. C., & Chang, C. (2016). [Early sinkhole detection using a drone-based thermal camera and image processing](#). *Infrared Physics & Technology*, 78, 223-232.

Liso, I. S. (2024). [Sinkhole occurrence and evolution, and seawater intrusion in a low-coastal setting of apulia](#). *Italian Journal of Engineering Geology and Environment*, Special Issue 1, 197-204.

Miller, S. J. (2010). [Submarine Cables Cause Dock Wall Failure at the Port of Milwaukee](#).

Omoko EN, Okeke OC, & Opara KD. (2018). [A Review of the Mechanism and Engineering/Environmental Problems of Subsidence Due to Groundwater Extraction \(Withdrawal\)](#). In *IARD International Journal of Geography and Environmental Management* (Vol. 4, Issue 4).

Park, K., Soliman, M., Je Kim, Y., & Hyun Nam, B. (2024). [Sinkhole stability chart for geotechnical investigation](#). *Transportation Geotechnics*, 45, 101191.

Rafique, M. U., Zhu, J., & Jacobs, N. (2022). [Automatic Segmentation of Sinkholes Using a Convolutional Neural Network](#). *Earth and Space Science*, 9(2).

Ramírez-Serrato, N. L., García-Cruzado, S. A., Herrera, G. S., Yépez-Rincón, F. D., & Villarreal, S. (2024). [Assessing the relationship between contributing factors and sinkhole occurrence in Mexico City](#). *Geomatics, Natural Hazards and Risk*, 15(1).

Shoab, M., Singh, V. K., & Ravibabu, M. V. (2022). [High-Precise True Digital Orthoimage Generation and Accuracy Assessment based on UAV Images](#). *Journal of the Indian Society of Remote Sensing*, 50(4), 613-622.

Waltham Tony, Bell Fred, & Culshaw Martin (2005). [Sinkholes and Subsidence Karst and Cavernous Rocks in Engineering and Construction](#). Springer-Praxis.

Support

Essa Al-Ansari, J. M., Hassan, K. E., Kantha Kumar, K., & Helali, K. N. (2023). [Development and Implementation of Ashghal Guidelines for the Evaluation and Repair of Sinkholes](#).

Schneider, C. A., Rasband, W. S., & Eliceiri, K. W. (2012). [NIH Image to ImageJ: 25 years of image analysis](#). In *Nature Methods* (Vol. 9, Issue 7, pp. 671-675).

Discussions

Del Grosso, A. (2001). [Monitoring of infrastructures in the marine environment](#). 107–117.

Guo, J., Liu, P., Xiao, B., Deng, L., & Wang, Q. (2024). [Surface defect detection of civil structures using images: Review from data perspective](#). In *Automation in Construction* (Vol. 158). Elsevier B.V.

Haryani, E. B. S., Hasan, S., & Candra, A. B. (2024). [Modeling sea currents in working environment area of Parit Rempak Karimun port](#). *Depik*, 13(1), 39-47.

Kaufmann, G. (2014). [Geophysical mapping of solution and collapse sinkholes](#). *Journal of Applied Geophysics*, 111, 271-288.

Margiotta, S., Negri, S., Parise, M., & Valloni, R. (2012). [Mapping the susceptibility to sinkholes in coastal areas, based on stratigraphy, geomorphology and geophysics](#). *Natural Hazards*, 62(2), 657-676.

Puzzilli, L. M., Ruscito, V., Madonna, S., Gentili, F., Ruggiero, L., Ciotoli, G., & Nisio, S. (2024). [Natural Sinkhole Monitoring and Characterization: The Case of Latera Sinkhole \(Latium, Central Italy\)](#). *Geosciences (Switzerland)*, 14(1).





Ranasinghe, R. (2016). [Assessing climate change impacts on open sandy coasts: A review](#). In *Earth-Science Reviews* (Vol. 160, pp. 320-332). Elsevier B.V.





Vega, B., Yang, J., Tchelepi, H., & Kovscek, A. R. (2020). [Investigation of Stress Field and Fracture Development During Shale Maturation Using Analog Rock Systems](#). *Transport in Porous Media*, 131(2), 503-535.





Inhibition of both CaSO₄ scales and corrosion using polyelectrolytes





Inhibición de la corrosión y las incrustaciones de CaSO₄ mediante la aplicación de polielectrolitos

Ramírez-Estrada, Alejandro*^a, Mena-Cervantes, Violeta Yasmín^b, Aguilar-Aguilar, Fidel Alejandro^c and Hernández-Altamirano, Raúl^d

^a  Instituto Politécnico Nacional •  FSC-2239-2022 •  0000-0001-6570-9203 •  563734

^b  Instituto Politécnico Nacional •  AFN-6089-2022 •  0000-0002-4403-8671 •  170728

^c  Instituto Politécnico Nacional •  LSL-8901-2024 •  0000-0003-3021-1186 •  402762

^d  Instituto Politécnico Nacional •  JGR-7510-2023 •  0000-0001-6685-2335 •  131289

CONAHCYT classification:

DOI: <https://doi.org/10.35429/H.2024.14.69.77>

Area: Engineering

Campo: Engineering

Discipline: Chemical Engineering

Subdiscipline: Corrosion

Key Handbooks

This research contributes to the field of enhanced hydrocarbon recovery. The polyelectrolytes evaluated in this work can be used for the control of corrosion and mineral fouling in oil reservoirs. The high temperature and salinity conditions of subway formations hinder the extraction of hydrocarbons due to the formation of mineral precipitates. In this regard, it is important to develop chemicals that prevent the formation of mineral scale in production wells and extraction equipment. Most of the products used in the oil industry come from foreign companies and are sometimes not effective enough. Therefore, it is necessary to develop proprietary technology to ensure domestic production and achieve energy dependence. The chemicals used in scale control must be effective in low pH conditions and must not promote corrosion of metallic materials. It has been found that performance of scale inhibitors is always influenced by the chemical characteristics and functional groups of the molecules. Therefore, it is necessary to perform precipitation and corrosion tests to select the appropriate inhibitor. The results showed that PEs inhibit 80% of CaSO₄ precipitation when added at low concentrations. PEs were found to inhibit the corrosion of carbon steel, generating efficiencies above 60%. HP_ITA was more effective in corrosion inhibition.

Citation: Ramírez-Estrada, Alejandro, Mena-Cervantes, Violeta Yasmín, Aguilar-Aguilar, Fidel Alejandro and Hernández-Altamirano, Raúl. 2024. Inhibition of both CaSO₄ scales and corrosion using polyelectrolytes. 69-77. ECORFAN.

* ✉ [alexram0021@gmail.com, aramirezes@ipn.mx]

Handbook shelf URL: <https://www.ecorfan.org/handbooks.php>



ISBN 978-607-8948-50-5/©2009 The Authors. Published by ECORFAN-Mexico, S.C. for its Holding Mexico on behalf of Handbook HRP. This is an open access chapter under the CC BY-NC-ND license [<http://creativecommons.org/licenses/by-nc-nd/4.0/>]

Peer Review under the responsibility of the Scientific Committee MARVID®- in contribution to the scientific, technological and innovation Peer Review Process by training Human Resources for the continuity in the Critical Analysis of International Research.



Abstract

This study aimed to inhibit both the precipitation of CaSO_4 and the corrosion of carbon steel by applying polyelectrolytes (PEs). A homopolymer of itaconic acid (HP_ITA) and a copolymer of itaconic acid and sodium vinyl sulfonate (HP_ITA-VS) were synthesized. In addition, static precipitation methods were used to induce the formation of CaSO_4 and evaluate the inhibition capacity of the PEs. Also, electrochemical techniques were used to analyze the corrosion processes and evaluate the effectiveness of the PEs. The results showed that the PEs inhibit the precipitation of CaSO_4 by up to 80% at low concentrations. On the other hand, it was found that the PEs inhibit the corrosion of carbon steel, generating efficiencies higher than 58%. In conclusion, the efficiency in inhibiting corrosion was found to be influenced by the specific functional groups present in the PEs.

Objectives	Methodology	Contribution
<ul style="list-style-type: none"> Synthesize polyelectrolytes Inhibit corrosion and CaSO_4 precipitation Found the best concentration 	<ul style="list-style-type: none"> Infrared spectroscopy Static precipitation test (NACE-TM0374). Electrochemical measures 	Polyelectrolytes inhibit both corrosion and CaSO_4 precipitation

Inhibition, Polyelectrolyte, Efficiency

Resumen

El objetivo de este trabajo es inhibir la precipitación del CaSO_4 y la corrosión del acero al carbono mediante la aplicación de polielectrolitos (PEs). Se sintetizó un homopolímero de ácido itacónico (HP_ITA) y un copolímero de ácido itacónico y vinil sulfonato de sodio (HP_ITA-VS). Además, se utilizaron métodos de precipitación estática para inducir la formación de CaSO_4 y evaluar la capacidad de inhibición de los PEs. También, se utilizaron técnicas electroquímicas para analizar los procesos de corrosión y evaluar la efectividad de los PEs. Los resultados mostraron que los PEs inhiben en un 80% la precipitación del CaSO_4 cuando se adicionan en bajas concentraciones. Por otra parte, se encontró que los PEs inhiben la corrosión del acero al carbono, generando eficiencias superiores al 58%. En conclusión, se tiene que la eficiencia en la inhibición de la corrosión es influenciada por los grupos funcionales que conforman a los PEs evaluados.

Objetivo	Metodología	Contribución
<ul style="list-style-type: none"> Sintetizar polielectrolitos Inhibir la corrosión y la precipitación de CaSO_4 Determinar la concentración adecuada 	<ul style="list-style-type: none"> Espectroscopia de infrarrojo. Precipitación mineral (NACE-TM0374). Mediciones electroquímicas 	Los polielectrolitos son capaces de inhibir la corrosión y la precipitación de CaSO_4

Inhibición, Polielectrolito, Eficiencia

Introduction

Corrosion and mineral scaling are common issues in the oil industry, especially in processes or operations involving the handling of water streams with high ionic content (Olajire, 2015). Mineral scales are typically composed of calcium carbonate (CaCO_3), calcium sulfate (CaSO_4), barium sulfate (BaSO_4), strontium sulfate (SrSO_4), calcium phosphate ($\text{Ca}_3(\text{PO}_4)_2$), or aluminosilicates. In some cases, scale deposits hinder oil and gas extraction operations by obstructing the pores that make up the formation. This issue is known as "formation damage" and arises from the incompatibility of waters within the formation (Peretomode et al., 2022). Additionally, mineral scaling can damage surface equipment (pipelines, boilers, pumps, heat exchangers, cooling towers, etc.), leading to production shutdowns or economic costs (Visser & Jeurnink, 1997; Walker et al., 2012).

Scale inhibitors are chemical substances that prevent the formation of mineral scales (Kamal et al., 2018). Ethylenediamine tetra(methylenephosphonate) (EDTMP), butylenediamine tetra(methylenephosphonate) (BDTMP), pentylenediamine tetra(methylenephosphonate) (PDTMP), hexamethylenediamine tetra(methylenephosphonate) (HDTMP), and ethylenediaminetetraacetic acid (EDTA) are examples of substances used as scale inhibitors (Mpelwa & Tang, 2019). However, it has been shown that these substances inhibit scaling only when used at high concentrations and generally precipitate or degrade under high-temperature or highly acidic conditions (Martinod et al., 2008). Additionally, there are reports indicating that phosphate-based inhibitors can cause eutrophication problems when discharged into water bodies (Nowack, 2003).

Polyelectrolytes are polymeric macromolecules that contain ionic groups in their structures (carboxylates, sulfonates, phosphates, etc.). They are used in water purification and treatment for the flotation of solid particles (Bolto & Gregory, 2007). The ionic groups in polyelectrolytes interact with charged particles and can form stable complexes to prevent the sedimentation of minerals (Meka et al., 2017). Additionally, they are used at low concentrations, and some are biodegradable. Polyelectrolytes can be a good option to prevent scale formation, and their ionic groups can also interact with charged surfaces to prevent the corrosion of metallic materials (Chen et al., 2019).

The objective of this work is to synthesize polyelectrolytes derived from itaconic acid and sodium vinyl sulfonate to analyze their effect on the inhibition of corrosion and the precipitation of CaSO_4 . Additionally, it aims to determine the appropriate inhibitor concentration and analyze the effect of chemical structure on the inhibition percentage.

Methodology

Polyelectrolyte synthesis

In this study, poly(itaconic acid) (HP_ITA) and poly(itaconic acid-co-sodium vinyl sulfonate) (CP_ITAC-VS) were synthesized. The synthesis of the inhibitors was based on the procedure described in patent US 11046605 B2. Subsequently, Fourier Transform Infrared Spectroscopy (FTIR) analyses were conducted to determine the functionality of the synthesized polyelectrolytes (Gao et al., 2015).

Precipitation test

The NACE-TM0374 methodology was used to analyze the effect of polyelectrolytes on the precipitation of CaSO_4 (Sanni et al., 2019). The test involves mixing (1:1) two brines (one containing calcium ions (Ca^{2+}) and the other containing sulfate ions (SO_4^{2-})) in different vials and adding a specific amount of polyelectrolyte (0, 50, 100, 150, and 200 ppm) to the mixture. The mixtures (brine + polyelectrolyte) are then heated to 80°C for 6 hours. After the heating period, the contents of each vial are filtered, and the amount of dissolved Ca^{2+} is determined. To evaluate the efficiency of CaSO_4 precipitation inhibition, the initial and final Ca^{2+} concentrations are compared using Equation 1.

$$\%EIP = \frac{C_A - C_B}{C_C - C_B} \quad [1]$$

Where C_A is the amount of Ca^{2+} in the solutions prepared with polyelectrolyte after heating, C_B is the amount of Ca^{2+} in the reference solution (without polyelectrolyte) after heating, and C_C is the amount of Ca^{2+} in the reference solution before heating.

Electrochemical measures

Electrochemical tests were conducted to analyze the effect of polyelectrolytes on the corrosion of AISI-1018 steel (Zou et al., 2011). For each experiment, fresh electrolyte solutions were prepared using analytical-grade reagents and deionized water. The corrosive medium consisted of a 0.01 M H_2SO_4 + 1.0 M NaCl solution. Additionally, to promote the formation of mineral scales, the corrosive solution also contained 0.01 M $\text{CaCl}_2 \cdot 2\text{H}_2\text{O}$. Measurements were performed at various polyelectrolyte concentrations (0, 100, 120, 150, 180, 200 ppm) to determine the optimal inhibitor concentration.

The electrochemical tests were conducted in a 250 mL glass cell under static conditions, atmospheric pressure, and a constant temperature of 40°C. The cell contained three electrodes: a piece of AISI-1018 steel coated with epoxy resin (0.71 cm² exposed area) as the working electrode (WE), a graphite rod as the counter electrode (CE), and a saturated calomel electrode (SCE) placed in a Luggin capillary as the reference electrode (RE). Potentiodynamic scans were performed to determine the corrosion rate. The WE was polarized in the cathodic direction to -300 mV vs OCP, followed by polarization in the anodic direction to +200 mV vs OCP.

Results

Spectroscopic analysis

Figure 1 shows the FTIR spectra of HP_ITA and CP_ITA-VS. In both spectra, a broad band is observed in the 3750–3400 cm⁻¹ region, representing the stretching of the O–H bond. Additionally, broad adsorption bands are seen in the 3400–3250 cm⁻¹ region, indicating the stretching of the –CH₂– bonds due to the vibration of the bonds linking the repeating units, and a band in the 1410–1380 cm⁻¹ interval indicating the bending of the O–H bond. Specifically, in the HP_ITA spectrum, a band at 1701 cm⁻¹ corresponds to the stretching of the C=O bond, and the band at 1176 cm⁻¹ represents the stretching of the C–O bond. On the other hand, in the CP_ITA-VS spectrum, a band at 1713 cm⁻¹ corresponds to the stretching of the C=O bond, and two adsorption bands at 1153 cm⁻¹ and 1036 cm⁻¹ indicate the asymmetric and symmetric stretching of the S=O bonds (Laschewsky, 2012).

Box 1

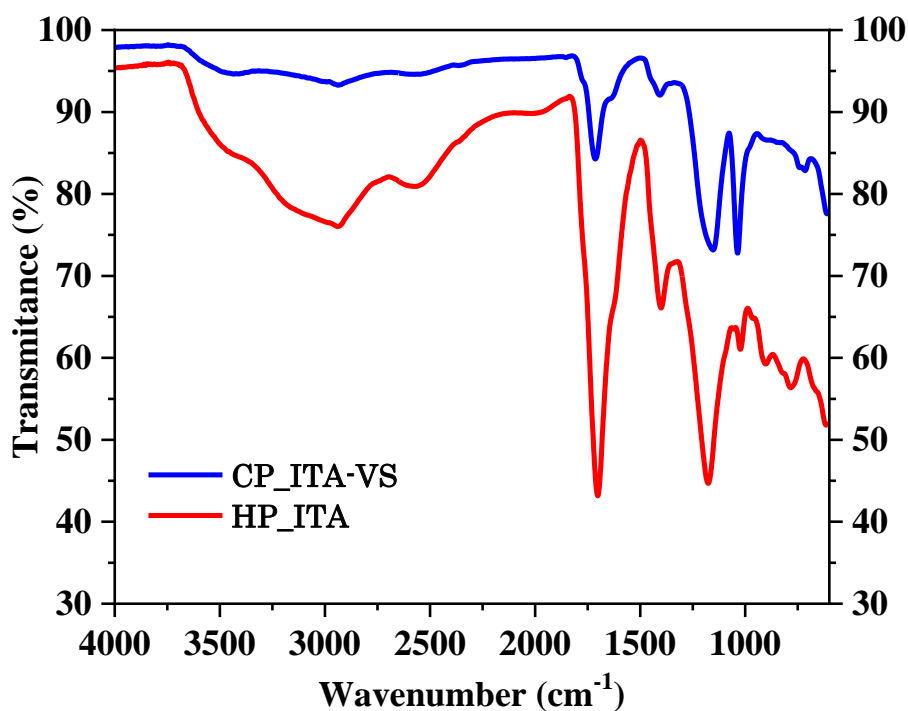


Figure 1

Infrared spectra of the synthesized polyelectrolytes

Source: Own construction

Inhibition of CaSO₄ precipitation

The results indicate that the polyelectrolytes can inhibit the precipitation of CaSO₄ at different concentrations. These polyelectrolytes have the ability to form stable complexes with the ionic species. Therefore, the inhibition can be attributed to the interaction of Ca²⁺ with the functional groups of the polyelectrolytes (Bisatto et al., 2022). Table 1 shows the results of the static precipitation tests. The synthesized polyelectrolytes exhibit high efficiency in inhibiting precipitation (EIP), with values greater than 80%. Additionally, it was found that the percentage of efficiency in inhibiting precipitation (EIP) increases as the concentration of polyelectrolytes increases.

Box 2

Table 1

The results of static precipitation tests at different polyelectrolyte concentrations

Concentration (ppm)	Efficiency in inhibiting precipitation	
	HP_ITA	HP_ITA
50	80.7 %	83.9%
100	89.1%	90.6%
150	97.8%	98.9%
200	>99%	>99%

Source: *Own construction*

Corrosion inhibition

Figure 2 shows the potentiodynamic scans of the working electrode (WE) in the presence and absence of HP_ITA. In the absence of polyelectrolyte (reference), the anodic current density (ACD) increases as the potential becomes more positive, indicating that anodic polarization promotes the corrosion of the metal surface. On the other hand, the cathodic current density (CCD) increases as the potential becomes more negative, indicating that cathodic polarization promotes the reduction of acidic species on the metal surface (Ramírez-Estrada et al., 2020).

Box 3

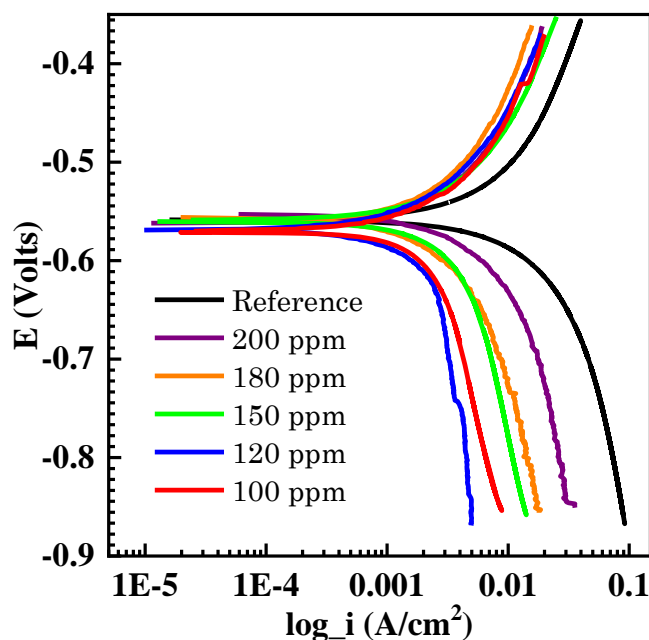


Figure 2

Potentiodynamic scans of AISI-1018 steel at different concentrations of HP_ITA

Source: *Own construction*

The ACD and CCD obtained in the presence of HP_ITA are lower than the current densities of the reference. The decrease in ACD in the presence of HP_ITA represents less corrosion of the material and suggests the formation of a protective film on the electrode surface (Tili et al., 2008).

On the other hand, the decrease in CCD in the presence of HP_ITA indicates that there are fewer active sites on the metal surface for the reduction of acidic species. This behavior can be attributed to the adsorption of HP_ITA molecules on the surface of the working electrode (Morizot et al., 1999).

Box 4

Table 2

Electrochemical parameters obtained from the potentiodynamic scans of AISI-1018 steel at different concentrations of HP_ITA

Concentration (ppm)	E_{corr} (Volts)	i_{corr} ($A \cdot cm^{-2}$)	β_a ($mV \cdot dec^{-1}$)	$-\beta_c$ ($mV \cdot dec^{-1}$)	CIE (%)
Reference	-0.564	7.95×10^{-3}	68	70	—
100	-0.570	2.83×10^{-3}	40	80	64.4
120	-0.565	2.17×10^{-3}	75	80	72.7
150	-0.560	2.48×10^{-3}	75	75	68.8
180	-0.560	2.91×10^{-3}	80	75	63.4
200	-0.560	3.28×10^{-3}	60	50	58.7

E_{corr} = corrosion potential; i_{corr} = current density of corrosion; β_a = anodic Tafel slope; β_c = cathodic Tafel slope; ICE = corrosion inhibition efficiency.

Source: Own construction

The electrochemical parameters from the potentiodynamic sweeps (Figure 2) are presented in Table 2. The results indicate that the corrosion inhibition efficiency (CIE) is greater than 58% and that at 120 ppm the efficiency is 72.7%. Additionally, it was found that the CIE decreases as the HP_ITA concentration increases (>120 ppm). PEs are soluble species that interact with ionic species and water molecules present on the metal surface. As the concentration of HP_ITA increases, more water molecules are attracted to the surface of the electrode (ET), which leads to an increase in the current density of corrosion (i_{corr}) and a decrease in the CIE. The appearance of the electrodes (images not shown) matches with the results of the electrochemical tests. In the absence of PEs (reference), the accumulation of $CaSO_4$ crystals on the electrode surface is observed. At low concentrations of HP_ITA (<180 ppm), the DCA values are lower than the reference, and the amount of scale deposits decreases. With 150 ppm of HP_ITA, very small crystals are observed on the electrode surface. However, at high concentrations (>150 ppm), the CIE values decrease, indicating an increase in the corrosion of the material. The images obtained at 180 ppm and 200 ppm show an increase in the number of crystals, indicating a rise in the corrosion of the metal surface.

Box 5

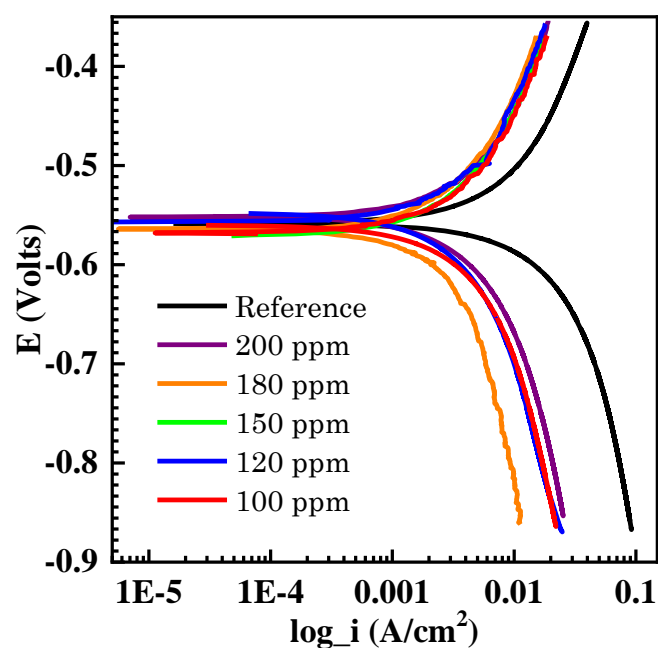


Figure 3

Potentiodynamic scans of AISI-1018 steel at different concentrations of CP_ITA-VS

Source: Own construction

Figure 3 shows the potentiodynamic sweeps of the WE in the presence and absence of CP_ITA-VS. The DCA and DCC obtained in the presence of CP_ITA-VS are lower than the current densities of the reference (Rehim et al., 2008). The decrease in the DCA by CP_ITA-VS represents less corrosion of the material and suggests the formation of a protective film on the electrode surface. Additionally, no changes are observed in the shape of the anodic curves when different concentrations of CP_ITA-VS are used, indicating that increasing the concentration does not alter the kinetics of the anodic reaction.

Box 6

Table 3

Electrochemical parameters obtained from the potentiodynamic scans of AISI-1018 steel at different concentrations of CP_ITA-VS

Concentration (ppm)	E_{corr} (Volts)	i_{corr} ($A \cdot cm^{-2}$)	β_a ($mV \cdot dec^{-1}$)	$-\beta_c$	CIE (%)
Reference	-0.564	7.95×10^{-3}	68	70	—
100	-0.560	3.14×10^{-3}	75	85	60.5
120	-0.550	2.51×10^{-3}	70	80	68.4
150	-0.571	2.31×10^{-3}	40	60	70.9
180	-0.570	2.68×10^{-3}	65	55	66.3
200	-0.550	2.81×10^{-3}	55	50	64.7

E_{corr} = corrosion potential; i_{corr} = current density of corrosion; β_a = anodic Tafel slope; β_c = cathodic Tafel slope; ICE = corrosion inhibition efficiency

Source: *Own construction*

The electrochemical parameters from the potentiodynamic sweeps (Figure 3) are presented in Table 3. The results indicate that at 150 ppm of CP_ITA-VS, the efficiency is 70.9%. However, it was found that as the concentration increases (>150 ppm), the corrosion inhibition efficiency (CIE) decreases. This behavior can be attributed to the increase in water molecules on the electrode surface; as the concentration of CP_ITA-VS increases, more water molecules are attracted to the electrode surface, which results in an increase in the corrosion current (i_{corr}) and a decrease in the CIE.

When comparing the results from Tables 2 and 3, it is found that the polyelectrolyte HP_ITA is more effective than CP_ITA-VS in corrosion inhibition. The CIE of HP_ITA is 72.7% at 120 ppm, while the CIE of CP_ITA-VS is 70.9% at 150 ppm. The difference in performance can be attributed to the functional groups that make up each polyelectrolyte (Saleh & Atia, 2006). The HP_ITA compound is composed solely of carboxyl groups, whereas the CP_ITA-VS compound contains both carboxyl and sulfonate groups.

Conclusions

The results showed that the PEs inhibit 80% of $CaSO_4$ precipitation when added at low concentrations. It was also found that the synthesized PEs inhibit carbon steel corrosion, achieving efficiencies greater than 60%. The HP_ITA compound was more effective in corrosion inhibition; the CIE of HP_ITA is 72.7% at 120 ppm, while the CIE of CP_ITA-VS is 70.9% at 150 ppm. Therefore, the sulfonate groups reduce the inhibition capacity of CP_ITA-VS.

Declarations

Conflict of interest

The authors declare that they have no conflicts of interest. They have no financial interests or personal relationships that could have influenced this book.

Authors' contributions

Ramírez-Estrada, Alejandro: Contributed to the conceptualization and design of the study, development of the methodology, data analysis, and manuscript writing.

Mena-Cervantes, Violeta Yasmín: Participated in project supervision, critical analysis of results, and manuscript review.

Aguilar-Aguilar, Fidel Alejandro: Collaborated in conducting laboratory experiments and in the collection and processing of experimental data.

Hernández-Altamirano, Raúl: Contributed to the technical analysis of results, data validation, and technical and academic review of the final document.

Availability of data and materials

The data and graphics shown in this study are available.

Funding

The research did not receive any type of funding for its realization.

Acknowledgments

We extend our sincere gratitude to the Centro Mexicano para la Producción más Limpia (CMP+L) and the Laboratorio Nacional de Desarrollo y Aseguramiento de la Calidad de Biocombustibles (LaNDACBio) for providing access to their laboratory facilities. We also thank the Consejo Nacional de Humanidades, Ciencias y Tecnologías (CONAHCyT) for their support

Abbreviations

ACD: Anodic current density
 CCD: Cathodic current density
 CE: Counter electrode
 CIE: Corrosion inhibition efficiency
 E_{corr} : Corrosion potential
 EIP: Efficiency in inhibiting precipitation
 FTIR: Fourier transform infrared spectroscopy
 HP_ITA: Poly(itaconic acid)
 HP_ITA-VS: Poly(itaconic acid-co-sodium vinyl sulfonate)
 I_{corr} : Current density of corrosion
 OCP: Open circuit potential
 PEs: Polyelectrolytes
 RE: Reference electrode
 WE: Working electrode

References

Antecedents

Olajire, A. A. (2015). [A review of oilfield scale management technology for oil and gas production](#). *Journal of Petroleum Science and Engineering*, 135, 723–737.

Peretomode, E., Oluyemi, G., & Haque, N. (2022). [Oilfield chemical formation interaction and the effects on petrophysical properties: a review](#). *Arabian Journal of Geosciences*.

Visser, J., & Jeurnink, Th. J. M. (1997). [Fouling of heat exchangers in the dairy industry](#). *Experimental Thermal and Fluid Science*, 14(96), 407–424.

Walker, M. E., Safari, I., Theregowda, R. B., Hsieh, M. K., Abbasian, J., Arastoopour, H., Dzombak, D. a., & Miller, D. C. (2012). [Economic impact of condenser fouling in existing thermoelectric power plants](#). *Energy*, 44(1), 429–437.

Basics

Kamal, M. S., Hussein, I., Mahmoud, M., Sultan, A. S., & Saad, M. A. S. (2018). [Oilfield scale formation and chemical removal: A review](#). *Journal of Petroleum Science and Engineering*, 171(January), 127–139.

- Mpelwa, M., & Tang, S. F. (2019). [State of the art of synthetic threshold scale inhibitors for mineral scaling in the petroleum industry: a review](#). *Petroleum Science*, 16(4), 830–849.
- Martinod, A., Euvrard, M., Foissy, A., & Neville, A. (2008). [Progressing the understanding of chemical inhibition of mineral scale by green inhibitors](#). *Desalination*, 220(1–3), 345–352.
- Nowack, B. (2003). [Environmental chemistry of phosphonates](#). In *Water Research* (Vol. 37, Issue 03, pp. 2533–2546).
- Bolto, B., & Gregory, J. (2007). [Organic polyelectrolytes in water treatment](#). *Water Research*, 41, 2301–2324.
- Meka, V. S., Sing, M. K. G., Pichika, M. R., Nali, S. R., Kolapalli, V. R. M., & Kesharwani, P. (2017). [A comprehensive review on polyelectrolyte complexes](#). *Drug Discovery Today*, 22(11), 1697–1706.
- Chen, M., Shafer-Peltier, K., Veisi, M., Randtke, S., & Peltier, E. (2019). [Complexation and precipitation of scale-forming cations in oilfield produced water with polyelectrolytes](#). *Separation and Purification Technology*, 222(January), 1–10.

Support

- Gao, Y., Fan, L., Ward, L., & Liu, Z. (2015). [Synthesis of polyaspartic acid derivative and evaluation of its corrosion and scale inhibition performance in seawater utilization](#). *Desalination*, 365, 220–226.
- Sanni, O. S., Bukuaghangin, O., Charpentier, T. V. J., & Neville, A. (2019). [Evaluation of laboratory techniques for assessing scale inhibition efficiency](#). In *Journal of Petroleum Science and Engineering* (Vol. 182). Elsevier B.V.
- Zou, Y., Wang, J., & Zheng, Y. Y. (2011). [Electrochemical techniques for determining corrosion rate of rusted steel in seawater](#). *Corrosion Science*, 53(1), 208–216.

Differences

- Laschewsky, A. (2012). [Recent trends in the synthesis of polyelectrolytes](#). *Current Opinion in Colloid & Interface Science*, 17(2), 56–63.
- Bisatto, R., Picoli, V. M., & Petzhold, C. L. (2022). [Evaluation of different polymeric scale inhibitors for oilfield application](#). *Journal of Petroleum Science and Engineering*, 213(February).
- Ramírez-Estrada, A., Mena-Cervantes, V. Y., Hernández-Altamirano, R., Vazquez-Arenas, J., García-Solares, M., Manzo-Robledo, A., & Trejo, G. (2020). [Implications of CaSO₄ scale growth on the corrosive response of carbon steel in acid media](#). *Colloids and Surfaces A: Physicochemical and Engineering Aspects*, 588(October 2019), 124336.





Discussions



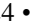
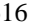
- Tlili, M. M., Rousseau, P., Ben Amor, M., & Gabrielli, C. (2008). [An electrochemical method to study scaling by calcium sulphate of a heat transfer surface](#). *Chemical Engineering Science*, 63, 559–566.
- Morizot, A., Neville, A., & Hodgkiess, T. (1999). [Studies of the deposition of CaCO₃ on a stainless steel surface by a novel electrochemical technique](#). *Journal of Crystal Growth*, 198–199(PART I), 738–743.
- Rehim, S. S. A., Hazzazi, O. a., Amin, M. a., & Khaled, K. F. (2008). [On the corrosion inhibition of low carbon steel in concentrated sulphuric acid solutions. Part I: Chemical and electrochemical \(AC and DC\) studies](#). *Corrosion Science*, 50(8), 2258–2271.
- Saleh, M. M., & Atia, A. A. (2006). [Effects of structure of the ionic head of cationic surfactant on its inhibition of acid corrosion of mild steel](#). *Journal of Applied Electrochemistry*, 36(8), 899–905.




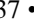
Effect of microstructural changes associated with hydrogen damage in API 5L X60 steels



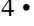
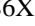
Efecto de los cambios microestructurales asociados al daño por hidrógeno en aceros API 5L X60

Calan-Canche, Damián*^a, Reda-Cruz, Alfredo^b, González-Sánchez, Jorge^c and Flores-Chan, J.E.^d

^a  Universidad Autónoma del Carmen •  U-3760-2018 •  0000-0001-6688-4468 •  415663

^b  Universidad Autónoma del Carmen •  LXW-3806-2024 •  0000-0002-8767-3616 •  952544

^c  Universidad Autónoma del Carmen •  LYO-8207-2024 •  0000-0001-5327-5137 •  31164

^d  Universidad Autónoma del Carmen •  LXW-4586-2024 •  0000-0003-4714-686X •  175430

CONAHCYT classification:

DOI: <https://doi.org/10.35429/H.2024.14.78.88>

Area: Engineering

Field: Engineering

Discipline: Electronic Engineering

Subdiscipline: Electrochemistry

Key Handbooks

Cathodic protection systems are complementary methods used to counteract the corrosion of carbon steel pipeline systems. During the cathodic polarization of the steel in this type of protection methods, hydrogen is generated on the steel surface, which in the best case evolves to molecular hydrogen and is released into the environment. However, part of this generated hydrogen is absorbed in the volume of the steel, causing loss of mechanical properties. In this research work, the microstructure of the steel is modified and the effects on the mechanisms of hydrogen absorption are analyzed. The mechanisms by which hydrogen damage occurs are due to the different environments to which the steel is subjected. Pipelines buried in the ground are mainly in contact with acidic and alkaline media. In acidic environments hydrogen release occurs naturally and in alkaline environments hydrogen release occurs as a consequence of water reduction, this in environments with absence of oxygen. To understand this process, it is essential to relate it to the microstructure present in the steel, which normally has characteristic phases that promote mechanical properties. Very important is the resistance to corrosion in the different media to which the steels are subjected. Modification of the microstructure by quenching heat treatment can be used on an industrial scale because of the associated costs. The quenching heat treatment modifies the mechanisms associated with hydrogen absorption. The microstructure formed consists of different phases of ferrite, bainite and martensite that provide the steel with superior mechanical properties. The heat treatment modifies the corrosion rate with respect to the base material.

Citation: Calan-Canche, Damián, Reda-Cruz, Alfredo, González-Sánchez, Jorge and Flores-Chan, J.E. 2024. Effect of microstructural changes associated with hydrogen damage in API 5L X60 steels. 78-88. ECORFAN.

* ✉ [\[jodcalan@gmail.com\]](mailto:jodcalan@gmail.com)

Handbook shelf URL: <https://www.ecorfan.org/handbooks.php>









ISBN 978-607-8948-50-5/©2009 The Authors. Published by ECORFAN-Mexico, S.C. for its Holding Mexico on behalf of Handbook HRPG. This is an open access chapter under the CC BY-NC-ND license [<http://creativecommons.org/licenses/by-nc-nd/4.0/>]

Peer Review under the responsibility of the Scientific Committee **MARVID**[®] in contribution to the scientific, technological and innovation Peer Review Process by training Human Resources for the continuity in the Critical Analysis of International Research.



Abstract







The effect of unconventional heat treatment and electrochemical behavior on API 5L X60 steel is evaluated by electrochemical processes/mechanisms associated with corrosion. The susceptibility to hydrogen absorption in soil solutions representative of the State of Campeche, Mexico, was evaluated. In the energy, chemical, metallurgical/mechanical, and petrochemical industries, API 5L X60 steel is used for storage tanks and pipelines for the transportation and transmission of oil and gas. These steels are in contact with different aggressive environments and are therefore subject to different degrees of corrosion and even cracking. The determination of the absorbed atomic hydrogen makes it possible to assess the susceptibility to hydrogen damage through the outer layers of the pipes. To study the influence of microstructure on the susceptibility to hydrogen absorption in API 5L X60 steel with and without heat treatment at 1050 °C for 30 minutes, the material was characterized by Scanning Electron Microscopy (SEM) and the electrochemical behavior of the metal under simulated CAM conditions, using Potentiodynamic Polarization Curves (PPC) and Oxidation and Hydrogenation Tests. The results indicated a change in the microstructure presenting polygonal grains of β (ferrite), α (perlite) and non-metallic inclusions in the matrix, which generates a significant influence on its ability to absorb atomic hydrogen in the subsurface layers. The kinetics revealed variability in the corrosion potential and passivity mechanism related to the interaction of the microstructure of the material and the chemistry of the solution. In short and intermediate periods of electrochemical charge, a higher corrosion rate is exhibited.

Objetive	Methodology	Contributions
 <p>Evaluate the effect of unconventional heat treatment on the electrochemical behavior and susceptibility to hydrogen absorption of API 5L X60 steel under simulated soil conditions from the State of Campeche, Mexico.</p>	 <p>Sample preparation and heat treatment.</p>  <p>Characterization Microstructure and electrochemistry</p>  <p>Results</p>	 <p>Understanding the corrosion and passivation mechanisms in this type of steel conditions</p>  <p>Simulating soil conditions allows this absorption phenomenon to be studied more realistically.</p>

Hydrogen, Heat treatment, Microstructure, steel, Soil solution

Resumen

El efecto del tratamiento térmico no convencional y el comportamiento electroquímico en el acero API 5L X60 se evalúa mediante procesos/mecanismos electroquímicos asociados con la corrosión. Se evaluó la susceptibilidad a la absorción de hidrógeno en soluciones de suelo representativas del Estado de Campeche, México. En las industrias energética, química, metalúrgica/mecánica y petroquímica, el acero API 5L X60 se utiliza para tanques de almacenamiento y tuberías para el transporte y la transmisión de petróleo y gas. Estos aceros están en contacto con diferentes ambientes agresivos y, por lo tanto, están sujetos a diferentes grados de corrosión e incluso a agrietamiento. La determinación del hidrógeno atómico absorbido permite evaluar la susceptibilidad al daño del hidrógeno a través de las capas externas de las tuberías. Para estudiar la influencia de la microestructura en la susceptibilidad a la absorción de hidrógeno en acero API 5L X60 con y sin tratamiento térmico a 1050 °C durante 30 minutos, se caracterizó el material por Microscopía Electrónica de Barrido (MEB), el comportamiento electroquímico del metal en condiciones CAM simuladas, con Curvas de Polarización Potenciodinámicas (CPP) y Ensayos de Oxidación e Hidrogenación. Los resultados indicaron un cambio en la microestructura presentando granos poligonales de β (ferrita), α (perlita) e inclusiones no metálicas en la matriz, lo que genera una influencia significativa en su capacidad para absorber hidrógeno atómico en las capas subsuperficiales. La cinética reveló variabilidad en el potencial de corrosión y el mecanismo de pasividad relacionado con la interacción de la microestructura del material y la química de la solución. En períodos cortos e intermedios de carga electroquímica se exhibe una mayor tasa de corrosión.

Efecto de los cambios microestructurales asociados al daño por hidrógeno en aceros API 5L X60		
Objetivo	Metodología	Contribuciones
 <p>Evaluar el efecto del tratamiento térmico no convencional sobre el comportamiento electroquímico y la susceptibilidad a la absorción de hidrógeno del acero API 5L X60 en condiciones de suelo simuladas del estado de Campeche, México.</p>	 <p>Preparación de muestras y tratamiento térmico</p>  <p>Caracterización Microestructural y Electroquímica</p>  <p>Resultados</p>	 <p>Comprender los mecanismos de corrosión y pasivación en este tipo de condiciones de</p>  <p>La simulación de las condiciones del suelo permite estudiar este fenómeno de absorción de forma más realista.</p>

Hidrógeno, Tratamiento térmico, Microestructura, Acero, Solución del suelo

Introduction

API 5L X60 steels have high corrosion resistance and optimal mechanical properties in different environments. This is due to the thermo-mechanical treatment carried out in its manufacturing process. These steels are used as automotive parts, in the manufacture of storage tanks, in the metal-mechanical industry, and in the transportation and conduction of fossil fuels.

Among the main weaknesses of this type of steel is that they are susceptible to hydrogen absorption, a phenomenon that can significantly compromise their structural integrity and cause adverse failures. The effect of absorbed hydrogen on the mechanical properties of steels involves phenomena such as embrittlement, stress corrosion, blistering, delamination or exfoliation^{1,2}. It is common practice in industry to minimise the absorption of hydrogen from the environment during this type of process, to avoid its embrittlement that occurs due to a process of absorption and diffusion of hydrogen, when it is incorporated into the crystal lattice permanently or temporarily³. The mechanism of hydrogen absorption is shown in Figure 1.

Box 1

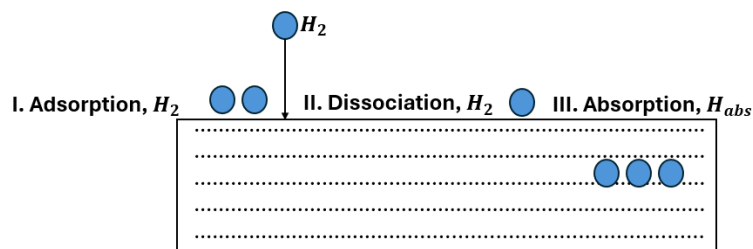


Figure 1

Mechanism of hydrogen absorption⁴

Source: Own elaboration

According to the theory the mechanisms that explain the interaction of hydrogen with iron is manifested by cathodically polarizing and evolving atomic hydrogen from the electrochemical reaction of hydrogen ions or water molecules, these are absorbed through the surface of the material as described in the following reactions⁵.



In equation (1), the hydronium ion (H_3O^+) gain an electron (e^-) resulting in an adsorbed hydrogen atom (H_{ad}) on the surface of the material and at the same time releasing a molecule of water (H_2O). In equation (2), a molecule of water (H_2O) gain an electron (e^-) The extra electron binds to a hydrogen atom in the water, forming a hydride ion (H^-), at the same time a hydroxide ion is released (OH^-). Depending on the reaction conditions, the hydrogen atom adsorbed on the surface of the material (3) can be absorbed or de-absorbed according to the Tafel reaction (4), as observed in the reaction (4).



In this reaction (4), two hydrogen atoms ($2H_{ad}$) adsorbed hydrogen molecules combine to form an adsorbed hydrogen molecule ($(H_2)_{ad}$). Another possibility of desorption is the Heyrovsky mechanism⁴ which also leads to a recombination with hydrogen according to the reaction (5).



The reaction (5) describes a reduction process in which the hydronium ion (H_3O^+) reduces one electron (e^-) and form water (H_2O). At the same time, the adsorbed hydrogen atom (H_{ad}) combines with other hydrogen to form the molecule of (H_2). The interaction between atomic hydrogen and metals has been extensively researched due to its impact on the properties of materials.

The small dimension of the hydrogen atom facilitates its penetration and diffusion into metals, especially when combined with the presence of carbon dioxide (CO_2), which accelerates corrosion and degrades protective layers⁶.

Experimental Methodology

Materials & Heat Treatment

API 5L X60 steel was used (See Figure 2), with the chemical composition shown in Table 1. Steel was evaluated in arrival condition (MCLMB) and subjected to a heat quenching treatment (MCLTT).

Box 2

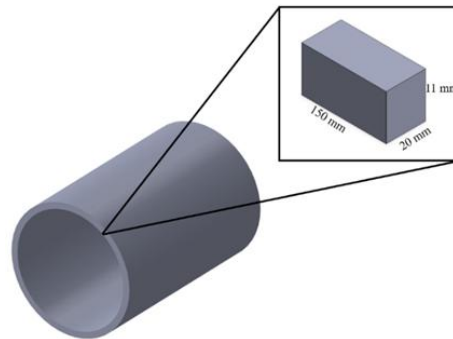


Figure 2

Material Steel API 5L X60

Source: Own elaboration

Box 3

Table 1

Chemical composition of API 5L X60 Steel

C	Mn	Si	Al	Nb	Cu	Cr	Ni	Ti	Co
0.067	1.381	0.206	0.023	0.038	0.022	0.016	0.023	0.0094	0.0055

Source: Own elaboration

The analyzed samples were subjected to unconventional quenching, which began with a gradual heating until permanence 1050°C, and for 30 minutes they were kept like this until they were finally quenching in water at room temperature^{7,8}. The heat treatment design is shown in Figure 3.

Box 4

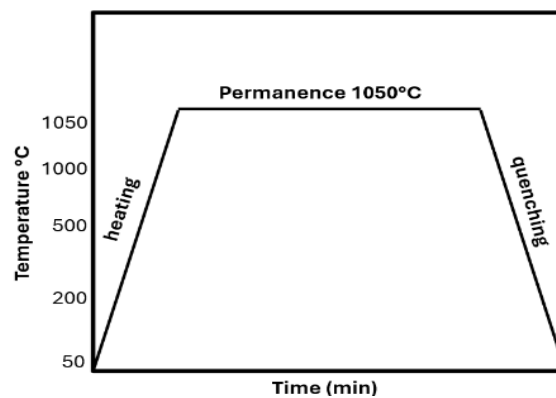


Figure 3

Heat treatment design

Source: Own elaboration

Electrochemical Testing

Electrolyte

For the electrochemical tests, the CAM solution was used, which simulates the composition of a soil characteristic of the state of Campeche. The chemical composition of the CAM solution is shown in Table 3⁹.

Box 5

Table 2

Chemical Composition of CAM Solution (g/l)

MgSO ₄ *7H ₂ O	CaCl ₂ *H ₂ O	KNO ₃	CaCO ₃	NaHCO ₃
0.0251	0.0215	0.050	0.202	0.823

Source: *Own elaboration*

The composition of the CAM solution shows the main constituents and has a pH of 8.1.

Characterization of the electrochemical behavior of the steels tested

The characterization of the electrochemical behavior of MCLMB and MCLTT in CAM solution was carried out by means of potentiodynamic polarization curves (PPC) and susceptibility to hydrogen damage by means of hydrogenation and oxidation assays. All tests were performed in a conventional three electrode electrochemical cell, MCLMB and MCLTT steels were the working electrodes, a saturated calomel electrode (SCE), as a reference and a graphite bar as an auxiliary electrode. The solution used as an electrolytic medium is representative of the Yucatan Peninsula, Mexico.

Other solutions with alkaline pH have been used to test steels^{10,11} but are representative of other locations. To characterize the electrochemical behavior using CPPs, polarization was polarized from -300 mV to 600 mV with respect to the open-circuit potential (OCP), at a speed of 10 mV/min. From these CPP graphs, the aggressiveness of the electrolytic medium and the corrosion rate of MCLMB and MCLTT are determined. All measurements were carried out on a Solartron Potentiostat/Galvanostat. The total amount of hydrogen evolved can be calculated by¹²:

$$Q_H^{ev} \int_0^{\tau_{exp}} I_{cathodic}(\tau) d\tau \quad E_{cathodic} = const \quad [6]$$

Hydrogenation was performed at constant cathode potential (-200 mV vs E_{corr}), at different times and in the absence of oxygen. Hydrogen oxidation was performed by the method described by Yan, M., et al.¹¹. The total amount of hydrogen absorbed sub-superficially by the metal can be defined through equation⁸:

$$Q_H^{abs} = \int_0^{\tau_{des}} [I_H(\tau) - I_{ref}(\tau)] d\tau \quad E_{anodic} = const \quad [7]$$

Where $I_H(\tau)$ is the anodic bias current for the sample charged with hydrogen and $I_{ref}(\tau)$ is the anodic bias current for the sample without hydrogenation. For the quantification of absorbed hydrogen (H_{abs}), Equation 8 was used for the samples tested.

$$C_H = \frac{Q_H^{abs}}{zFv} \quad [8]$$

Where, z is the number of electrons participating in the reaction, F is Faraday's constant, and v is the effective volume of the sample.

Results

Microstructural characterization of the steels tested

Figure 4 shows a micrograph of MCLMB, the main phases that were identified were polygonal ferrite (α) and perlite (β), characteristics of API 5L X60 steels. Non-metallic inclusions were also randomly found in the steel matrix, ranging in size from 3 to 50 μm . In recent research, Velázquez et al. revealed that non-metallic inclusions have a role in pitting corrosion directly, causing defects in the microstructure. Inclusions with smaller areas were observed that tend to be more prone to corrosion than larger inclusions. However, it seems that elongated inclusions are more active than circular inclusions because the proportion of inclusions to active starts is higher than that of circular ones¹³.

Box 6

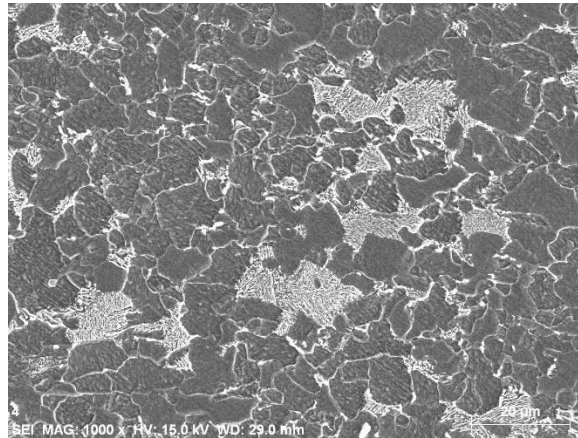


Figure 4

MCLMB Steel Microstructure

Source: *Own elaboration*

The inclusions identified in MCLMB steel are rich in silicon (Si), Aluminium (Al), Magnesium (Mg) and Calcium (Ca), although they may be present as complexes of O-Al-Mg-Ca¹³. Inclusions consist of one or several deformed or non-deformed thin parts, deformed thin parts are mainly low-melting calcium aluminates, while non-deformed particles contain more CaS or CaO y Al₂O₃ high melting point¹⁴. The main elements that exist in inclusions are Al, O, Ca, Mg, Mn y C, as well as complexes or mixes Al-Mg-Ca-O. The interfaces of non-metallic and precipitated inclusions are considered strongly irreversible traps for hydrogen at normal temperatures and conditions¹⁴. The microstructure of MCLTT steel is characterized phases of bainite and ferrite. The microstructure of MCLTT steel increases the mechanical properties with more diverse phases in the matrix.

Electrochemical behavior of MCLMB and MCLTT steel, in CAM solution

Figure 5 shows the CPPs of MCLMB and MCLTT steels in CAM solution. In PPCs, it is observed that MCLMB steel exhibits a more negative corrosion potential, and a higher corrosion current density compared to MCLTT¹⁵. However, MCLMB steel is more susceptible to corrosion, due to the formation of corrosion products and the dissolution of the phases present by the chemistry of the solution¹³. The two metallurgical conditions tested show a controlled process by charge transfer, indicating that they are susceptible to corrosion in CAM solution. MCLTT steel revealed greater corrosion resistance, with a nobler corrosion potential and lower current densities¹⁵. The corrosion rates for MCLMB and MCLTT specimens are 2.42 mm/year and 1.9 mm/year, respectively. This behavior can be attributed to the fact that heat treatment can produce a protective effect against grain regrouping corrosion in steel¹⁶.

Box 7

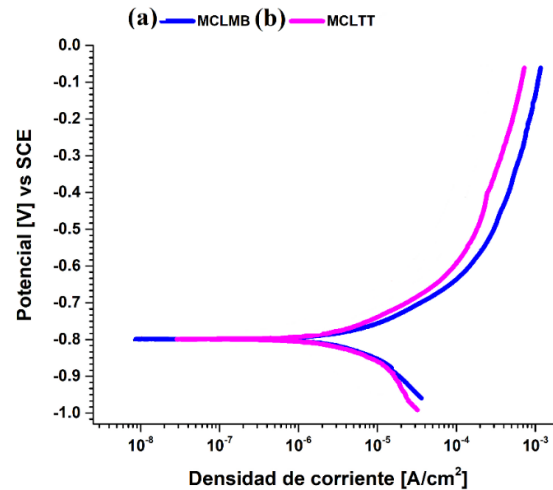


Figure 5

CPP of MCLMB (a) and MCLTT (b) steel, in CAM solution

Source: *Own elaboration*

Behavior of the cathodic and anodic current density associated with hydrogen

The current time series associated with the evolution of atomic hydrogen can be statistically analyzed to give us information on the behavior of the hydrogen-metal interaction. Electrochemical noise is defined as low-frequency (<10 Hz) and low-amplitude potential or current fluctuations, originating from natural electrochemical variations of corrosive kinetics. Electrochemical noise under potentiostatic and galvanostatic control¹⁷ has been used to interpret corrosive processes in stainless steels¹⁸, processes associated with the evolution of hydrogen^{19,20}.

Figure 6 shows the behavior of the average current density of the MCLMB and MCLTT. The MCLMB sample shows an overall increase in cathodic current density over time, although with some fluctuations. This suggests that the rate of the reduction reaction increases over time. On the other hand, it was observed that MCLTT steel also shows an overall increase in current density, but with a slightly lower slope than MCLMB. In addition, it has a more marked fluctuation around 10 hours. The differences in the behavior of the two metallurgical conditions are attributed to different electrochemical processes that occur on the surface of each of the steels tested. These processes may include the adsorption of chemical species, the formation of passive films, or more complex reactions¹⁹.

Box 8

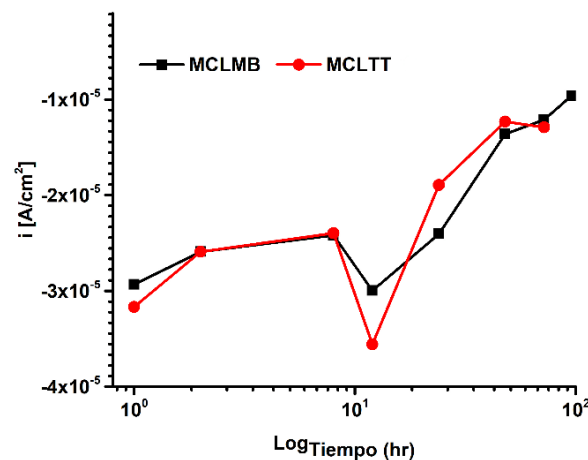


Figure 6

Behavior of the average current density of MCLMB and MCLTT in CAM solution.

Source: *Own elaboration*

On the other hand, heat treatment generates different phases, among which are: bainite, acicular ferrite, globular ferrite, Widmanstätten ferrite.

On the contrary, the base metal has ferrite and perlite as its main phases, in these phases the average cathodic current density tends to decrease with increasing assay time, this is in accordance with the cathodic protection mechanism, since the entire surface inhibits the anode and cathode sites that could cause the average current density to vary widely, this is due to the cathodic potential applied. Figure 7 shows the concentration of atomic hydrogen (AC) and the permeation coefficient of the steels in CAM solution.

Box 9

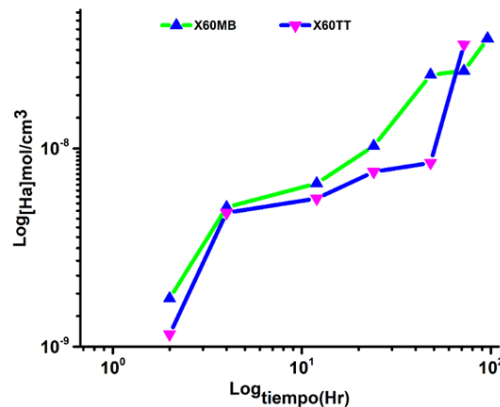


Figure 7

Hydrogen concentration in MCLMB (a) and MCLTT (b) steels

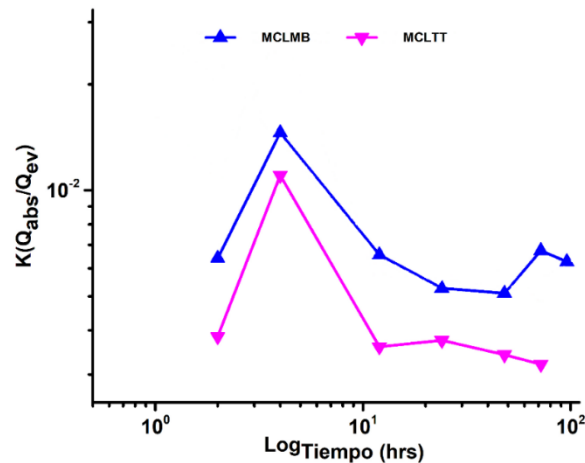
Source: *Own elaboration*

MCLMB steel shows a higher susceptibility to sup-surface atomic hydrogen adsorption compared to MCLTT steel in the first hours of electrochemical charge, although it always tends to increase with longer test times. In the 48 hours of electrochemical charge MCLMB steel almost equals the concentration of adsorbed atomic hydrogen as MCLTT steel, this behavior may be due to a slower process kinetics in MCLTT steel. The higher absorption capacity of atomic hydrogen in MCLMB steel is mainly due to the microstructure constituted by ferrite-perlite interfaces, grain boundaries and non-metallic inclusions²⁰. Unlike MCLTT steel which absorbs less atomic hydrogen compared to non-heat-treated steel according to the concentration of absorbed hydrogen (Ha).

Previous research by Park, G. T.²¹, has shown that the presence of an acicular bainite-ferrite structure, mainly associated with Acicular Ferrite, is characterized by randomly oriented grain boundaries and a high density of dislocations. Due to the complex and entangled network of dislocations, atomic hydrogen is trapped in reversible traps (dislocations), decreasing absorption and consequent diffusion into the volume of the steel. It was observed that MCLTT steel has a lower concentration of hydrogen compared to MCLTT steel. This suggests that heat treatment is more effective in reducing hydrogen diffusion. The difference in hydrogen concentration between heat-treated and non-heat-treated steels becomes more apparent at longer exposure times.

Figure 8 shows the behavior of the permeation coefficient of MCLMB and MCLTT steels, this parameter does not indicate the sup-surface absorption efficiency of the steels tested¹⁹. Initially, MCLMB steel has a permeation coefficient higher than X60MCLTT. However, over time, this difference narrows. This indicates that heat treatment could give the steel a lower initial permeability to hydrogen, but in the long term, both alloys tend to behave similarly.

It was observed that, during the first hours of exposure, a maximum was reached for MCLMB steel and in the four-hour test for MCLTT steel. Subsequently, both types of steel show an overall decrease in the permeation coefficient as exposure time increases. This suggests that, over time, steel become less permeable to hydrogen, this may be due to atomic hydrogen saturation in the subsurface film of the steels²¹.

Box 10**Figure 8**

Permeation coefficient behavior in MCLMB and MCLTT steels.

Source: Own elaboration

Hydrogen saturation on the metal surface, which exceeds its solubility limit, is the main cause of the decrease in the K-coefficient as the hydrogenation process progresses. This coefficient, which initially reaches high values, reflects the intense electrochemical activity that occurs in the early stages¹⁹.

Conclusions

MCLMB and MCLTT steel showed susceptibility to subsurface hydrogen absorption in the CAM solution. At short and medium electrochemical charge times it shows aggressiveness and tends to increase the concentration of hydrogen. This indicates the need for longer hydrogenation times to be able to observe behavior comparable to real operating situations.

The microstructure has a significant influence on the susceptibility to subsurface absorption of atomic hydrogen, since in the two solutions tested it tends to absorb less hydrogen, although a more in-depth study and analysis of the influence of heat treatment is necessary.

Declarations

Conflict of interest

The authors declare that they have no conflict of interest. They have no financial interests or personal relationships that could have influenced this book.

Authors' contribution

Calan-Canche, Damian: Main author of research topic, contribution to methodology and analysis of results.

Reda-Cruz, Alfredo: Review of research methodology.

Gonzalez-Sanchez, Jorge: Contribution to the subject of research, review of methodology and analysis of results.

Flores-Chan, J. E.: Analysis of results

Availability of data and materials

The data and materials used in this study are available.

Financing

No financing

References

Antecedents

Uribe Pérez, I., et.al (2011). [Fundamentals of hydrogen damage in steels](#). Man, and Machine, pages 2-5.

Thompson, A W, & Bernstein, I M (1976). Effect of hydrogen on behavior of materials.

M. Barteri, F. Mancina, A. (1987) [Engineering diagrams and sulphide stress corrosion cracking of duplex stainless steels in deep sour well environment](#). Corrosion Science, pages 1-5.

Truschner, M., Trautmann, A., & Mori, G. (2021). [The basics of hydrogen uptake in iron and steel](#). BHM Berg-und Huttenmannische Monatshefte, pages 1-7.

E. G. Dafft, K.B.a.H.J.E., (1999). [Investigations of hydrogen evolution kinetics and hydrogen absorption by iron electrodes during cathodic polarization](#). Corrosion Science, pages 1-7.

Linter, B. ., y Burstein, G. . (1999). [Reactions of pipe steels in carbon dioxide solutions](#). Corrosion Science, 41(1), 117–139.

Basics

Niu, L., Cheng, Y.F., (2007), [Mechanism for hydrogen evolution reaction on pipeline steel in near-neutral pH solution](#). Electrochemistry Communications, pages 1-5.

B.R. Linter, G.T.B., (1999), [Reactions of pipelines steels in carbon dioxide solutions](#). Corrosion Science, pages 1-9.

ASTM, Designation: E407-07, “[Standard Practice for Microetching Metals and Alloys](#)”, 2015.

Noor, E.A., (2011) [Comparative analysis for the corrosion susceptibility of Cu, Al, Al-Cu and C-Steel in soil solution](#). Materials and Corrosion, pages. 1-4.

K. Belmkre, N.A., F. Kermiche, M. Wery and J. Pagetti, (1998) [Corrosion study of carbon steel protected by a primer, by electrochemical impedance spectroscopy \(EIS\) in 3% NaCl medium and in a soil simulating solution](#). Materials and Corrosion: pages. 1-4.

Maocheng Yan, Y.W. (2006) [Study on hydrogen absorption of pipeline steel under cathodic charging](#). Corrosion Science, pages. 1-4.

Support

Velázquez, J.C. et.al (2023) [Study on the Influence of Non-Metallic Inclusions on the Pitting Corrosion of API 5L X60 Steel](#). Coatings 2023, pages1-10

Xinhua Wang, X.L., Qiang Li, Fuxiang Huang, Haibo Li, and Jian Yang (2014). [Control of stringer shaped non-metallic inclusions of CaO-Al₂O₃ system in API X80 linepipe steel plates](#). Steel research international pages. 1-9.

Discussions

Luo Jinheng, Z.L., et al. (2016). [Electrochemical corrosion behaviors of the X90 linepipe steel in NS4 solution](#). Natural Gas Industry B. pages. 1-3.

Luo Jinheng, Z.L., Li Lifeng, Yang Fengping, Ma Weifeng, Wang Ke, Zhao Xinwei²⁵. [Electrochemical corrosion behaviors of the X90 linepipe steel in NS4 solution](#). *Natural Gas Industry B*, 2016. 3: p. 346-351.

L. Zhang, M.D., and Y. Li, (2012) [Effects of Applied Potentials on the Hydrogen-Induced Cracking of Pipeline Steel in Low-Temperature and Low-Dissolved-Oxygen Seawater](#). *Corrosion*. pages 1-5.

Cheng, Y.F., (2007). [Fundamentals of hydrogen evolution reaction and its implications on near-neutral pH stress corrosion cracking of pipelines](#). *Electrochemical Acta*, pages.1-5.

Gyu Tae Park, S.U.K., Hwan Gyo Jung, Kyo Young Kim. [Effect of microstructure on the hydrogen trapping efficiency and hydrogen induced cracking of linepipe steel](#). *Corrosion Science*, pages 1-4.





Benítez, José Luis, Lárez Velásquez, Cristóbal, & Rojas de Gáscue, Blanca. (2015). [Cinética de absorción y transporte del agua en hidrogeles sintetizados a partir de acrilamida y anhídrido maleico](#). *Revista Latinoamericana de Metalurgia y Materiales*, pages 1-4.





R.K. Gupta, N.L. Sukiman, M.K. Cavanaugh, B.R.W. Hinton, C.R. Hutchinson, N. Birbilis, (2012). [Metastable pitting characteristics of aluminium alloys measured using current transients during Potentiostatic polarisation](#). *Electrochimica Acta*. 66 245–254.





Effect of heat treatment on hydrogen permeation of API 5L X60 steel in soil solution





Efecto del tratamiento térmico en la permeación de hidrógeno del acero API 5L X60 en solución de suelo

Calan-Canche, Damián^{*a}, Pérez-Montejo, Saltiel^b, Flores-Chan, J. E.^c and González-Sánchez, Jorge^d

^a  Universidad Autónoma del Carmen •  U-3760-2018 •  0000-0001-6688-4468 •  415663

^b  Universidad Autónoma del Carmen •  LYO-9195-2024 •  0000-0002-1750-0154 •  594590

^d  Universidad Autónoma del Carmen •  LXW-4586-2024 •  0000-0003-4714-686X •  175430

^c  Universidad Autónoma del Carmen •  LYO-8207-2024 •  0000-0001-5327-5137 •  31164

CONAHCYT classification:

DOI: <https://doi.org/10.35429/H.2024.14.89.96>

Area: Engineering

Field: Engineering

Discipline: Electronic Engineering

Subdiscipline: Electrochemistry

Key Handbooks

This work deepens the study of the influence of steel microstructure on hydrogen permeation. The evaluated steel was subjected to a quenching heat treatment, favoring the formation of phases such as bainite and acicular ferrite. These phases increase the mechanical properties and increase the reversible traps (dislocations), which promote hydrogen absorption/release. This mechanism occurs at the metal-electrolyte interface and favors increasing the service life of the steels. It is of vital importance to deepen the knowledge of the influence of the microstructure on the susceptibility to hydrogen damage. With a heat treatment with accessible and simple costs for the industry we can obtain good results in the behavior of hydrogen diffusion in the tested steel. The microstructural changes due to quenching heat treatment have a multidisciplinary approach to understand the changes in mechanical properties, susceptibility to hydrogen damage and corrosion rate. For this purpose, a classical electrochemical technique such as electrochemical hydrogen permeation is used to obtain information related to the microstructure and the behavior of hydrogen diffusion in the volume of the steel. Steels are the most widely used material due to their mechanical properties and resistance to corrosion in the different environments to which they are subjected. Hence the interest in improving their properties to extend their useful life. The quenching heat treatment modifies the diffusion of hydrogen through the steel. The bainite and acicular ferrite phases promote the formation of reversible hydrogen traps.

Citation: Calan-Canche, Damián, Pérez-Montejo, Saltiel, Flores-Chan, J. E. and González-Sánchez, Jorge. 2024. Effect of heat treatment on hydrogen permeation of API 5L X60 steel in soil solution. 89-96. ECORFAN.

*  [\[jodcalan@gmail.com\]](mailto:jodcalan@gmail.com)

Handbook shelf URL: <https://www.ecorfan.org/handbooks.php>









ISBN 978-607-8948-50-5/©2009 The Authors. Published by ECORFAN-Mexico, S.C. for its Holding Mexico on behalf of Handbook HRP. This is an open access chapter under the CC BY-NC-ND license [<http://creativecommons.org/licenses/by-nc-nd/4.0/>]

Peer Review under the responsibility of the Scientific Committee **MARVID**[®] in contribution to the scientific, technological and innovation Peer Review Process by training Human Resources for the continuity in the Critical Analysis of International Research.



Abstract







Hydrogen permeation tests were carried out on API 5L X60 steel specimens under three conditions: base material and heat-treated specimens at 1050 °C for 15 and 20 minutes, then quenched in water. These specimens were subjected to hydrogen permeation tests in CAM soil solution, representative of the state of Campeche. The heat treatment modified the microstructure present in the steel and therefore the behavior of the hydrogen permeation curves. The bainite and acicular ferrite phases present in the heat-treated steel acted as reversible traps, due to their large number of dislocations. The diffusion coefficient and the number of reversible traps present in the volume of the steel were determined.

Objective	Methodology	Contributions
 <p>Determine the influence of microstructure on hydrogen permeation, in conditions representative of the state of Campeche, Mexico.</p>	 <p>Sample preparation and heat treatment.</p>  <p>Characterization Microstructure and electrochemistry</p>  <p>Results</p>	 <p>Understanding the influence of microstructure on hydrogen permeation.</p>  <p>Simulating soil conditions allows this absorption phenomenon to be studied more realistically.</p>

Hydrogen, Heat treatment, Microstructure

Resumen

Se realizaron pruebas de permeación de hidrógeno en probetas de acero API 5L X60 bajo tres condiciones: material base y probetas tratadas térmicamente a 1050 °C durante 15 y 20 minutos, posteriormente templadas en agua. Estas probetas fueron sometidas a pruebas de permeación de hidrógeno en solución de suelo CAM, representativa del estado de Campeche. El tratamiento térmico modificó la microestructura presente en el acero y por ende el comportamiento de las curvas de permeación de hidrógeno. Las fases bainita y ferrita acicular presentes en el acero tratado térmicamente actuaron como trampas reversibles, debido a su gran número de dislocaciones. Se determinó el coeficiente de difusión y el número de trampas reversibles presentes en el volumen del acero.

Objetivo	Metodología	Contribuciones
 <p>Determinar la influencia de la microestructura en la permeación del hidrógeno en condiciones representativas del estado de Campeche, México.</p>	 <p>Preparación de muestras y tratamiento térmico</p>  <p>Caracterización Microestructural y Electroquímica</p>  <p>Resultados</p>	 <p>Entendimiento de la influencia de la microestructura sobre la permeación del hidrógeno</p>  <p>La simulación de las condiciones del suelo permite estudiar este fenómeno de absorción de forma más realista.</p>

Hidrógeno, Tratamiento térmico, Microestructura

Introduction

Low-strength alloy steels (HSLA) are good mechanical properties of strength, toughness and weldability due to the thermo-mechanical work performed during manufacture and their low carbon content. The different environments to which these steels are subjected range from acidic (swamp) and basic (soil) media, these hinder the prolonged use of HSLA steels due to susceptibility to corrosion and hydrogen damage.

One of the methods that minimize the loss of material by corrosion is cathodic protection, this has the indirect effect of evolving hydrogen on the surface of steel, a part of the evolved hydrogen enters inside as an atom, hydrogen is stored in reversible and irreversible traps.

Reversible traps are sites where the energy needed to bond is small this facilitates the entry and exit of hydrogen atoms, on the contrary, irreversible traps have a high binding energy this makes their exit from the inside metal difficult. The presence of hydrogen affects the mechanical properties of strength and toughness. The formation and presence of microstructural defects accelerates the effects of hydrogen damage.

Heat treatments are an effective method to improve mechanical properties and corrosion resistance. HSLA steels with low carbon (C) and Niobium (Nb), can be heat treated by hardening, the low carbon quantity minimizes the formation of martensite and the presence of Nb does not allow a large increase in average grain size.

This work studies the influence of microstructure and the effect of heat treatment on API 5L X60 micro-alloy steels on hydrogen diffusion. In addition to the effect of the constant cathodic potential on the evolutionary dynamics of atomic hydrogen in steels with and without heat treatment. The diffusion coefficient of the untreated and heat-treated steels was determined.

Methodology

API 5L X60 steel with ferrite as the main constituent was used, in addition to perlite bands (MCLMB). This steel was cut into strips of 150 mm x 20 mm x 11 mm, then subjected to 1050 °C for 15 (MCLTT15) and 30 (MCLTT30) minutes, immediately quenched in water.

The microstructure of the heat-treated test pieces was bainite and acicular ferrite, the latter being highly sub-structured and equiaxiated which is formed in continuous cooling by mixing diffusion and stresses which give the steels a high tenacity^{1,2}.

For the hydrogen permeation tests, steel with and without heat treatment was milled to 1 mm in thickness, with an effective working area of 1 cm². The input side of the hydrogen was sanded with silicon carbide (CS) paper from #100 to #1200 and the output side was sanded with CS from #100 to #2000, then polished with 1 μm diamond paste, this was electrochemically coated with palladium in order to minimize the base hydrogen permeation current density.

Permeation tests were carried out in a double cell, one for the generation or electrochemical charge of hydrogen and the other for the oxidation of hydrogen. The solution used for the electrochemical charge was CAMP (pH=8.1), the chemical composition of the soil-simulating solution is shown in Table 1.

Box 1

Table 1

Chemical composition of the CAM solution

Compound	MgSO ₄ *7H ₂ O	CaCl ₂ *H ₂ O	KNO ₃	CaCO ₃	NaHCO ₃
Quantity (g/l)	0.0251	0.0215	0.050	0.202	0.823

The CAM solution is representative of the soil in the state of Campeche. A constant cathode potential of -950 mV vs SCE was applied to the input side allowing hydrogen generation and diffusion within the test pieces. On the output side, 0.2 molar solution of NaOH was used at a constant anode potential of 170 mV vs SCE, this potential was sufficient for the formation of a stable passive layer. Prior to permeation tests, high purity argon was bubbled to remove dissolved oxygen from the solution in order to prevent surface oxidation. The permeation current was recorded by means of a Solartron Potentiostat/Galvanostat and the reduction current was recorded with a Uicorr Potentiostat. All tests were conducted at 25°C 1.

Analysis of the permeation current

In Figure 1, the characteristic parameters that can be obtained from the hydrogen permeation curve are shown.

Box 2

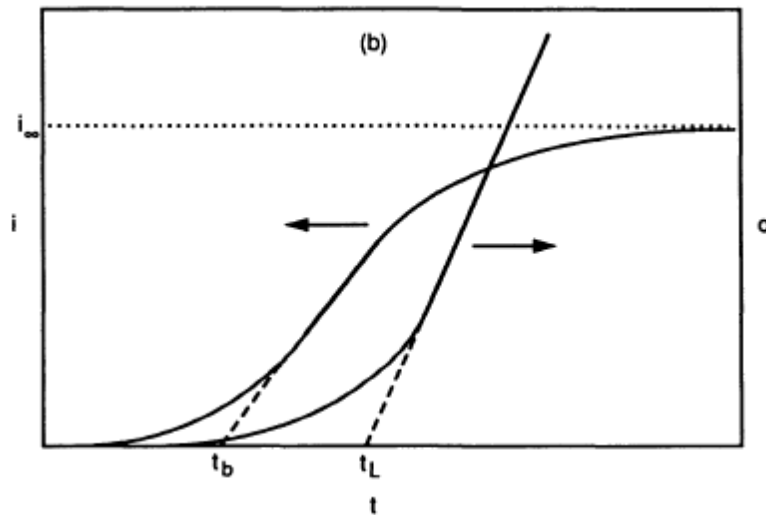


Figure 1

Variation in the anode current over time for a membrane with a constant flow on the electrochemical charge side

Source: 3, 10, 11.

The flow of hydrogen J_H ($\frac{\text{molH}}{\text{m}^2\text{s}}$), through the steel was measured by the steady-state permeation current density ($\frac{i_p^\infty}{nF}$)^{3, 10, 11}:

$$J_H = \frac{i_p^\infty}{nF} \quad [1]$$

Where n is the number of electrons transferred and F is the Faraday constant. The rate of hydrogen permeation ($\frac{\text{molH}}{\text{m}^2\text{s}}$), is defined by^{3, 10, 11}:

$$J_H L = \frac{i_p^\infty}{nF} \quad [2]$$

Where L is the thickness of the test piece. The effective diffusivity of hydrogen D_{eff} , can be calculated by^{3, 10, 11}:

$$D_{eff} = \frac{L^2}{6t_L} \quad [3]$$

Where the time of backtracking t_L , is the point on the hydrogen permeation curve where $i_t = 0.63i_p^\infty$. If the surface hydrogen is in thermodynamic equilibrium with the sub-surface hydrogen, the apparent hydrogen solubility (C_{app}), is^{3, 10, 11}:

$$C_{app} = \frac{J_H L}{D_{eff}} \quad [4]$$

In addition, the density of hydrogen traps can be estimated according to the following equation:

$$N_T = \frac{c_0}{3} \left(\frac{D_1}{D_{eff}} - 1 \right) \quad [5]$$

Where N_T is the number of hydrogen trap sites per unit volume and D_1 is the diffusion coefficient in the crystal lattice for α -Fe is $1.28 \times 10^{-4} \text{ cm}^2\text{s}^{-1}$ ^{4,5}.

Results

Analysis of the cathode current associated with the hydrogen evolution process

Figure 2 shows the I_{cath} of MCLMB, MCLTT15 and MCLTT30 in CAMP solution at potential -950 mV vs SCE.

At a cathodic potential of -950 mV vs SCE, the Volmer reaction is favored:



H_{ad} atoms can be absorbed by steel:



This input mechanism is given with water molecules and proceed in alkaline and neutral media^{6,7}. Curve 1 has the lowest I_{cath} values compared to heat-treated steels. In general, the I_{cath} values tend to increase from $45 \mu\text{Acm}^{-2}$ to $12 \mu\text{Acm}^{-2}$, the I_{cath} values are similar to those obtained by the test pieces in NS4 solution. For hardened and tempered steels, the stress corrosion mechanism appears to be dominated by hydrogen embrittlement^{8,9}.

Box 3

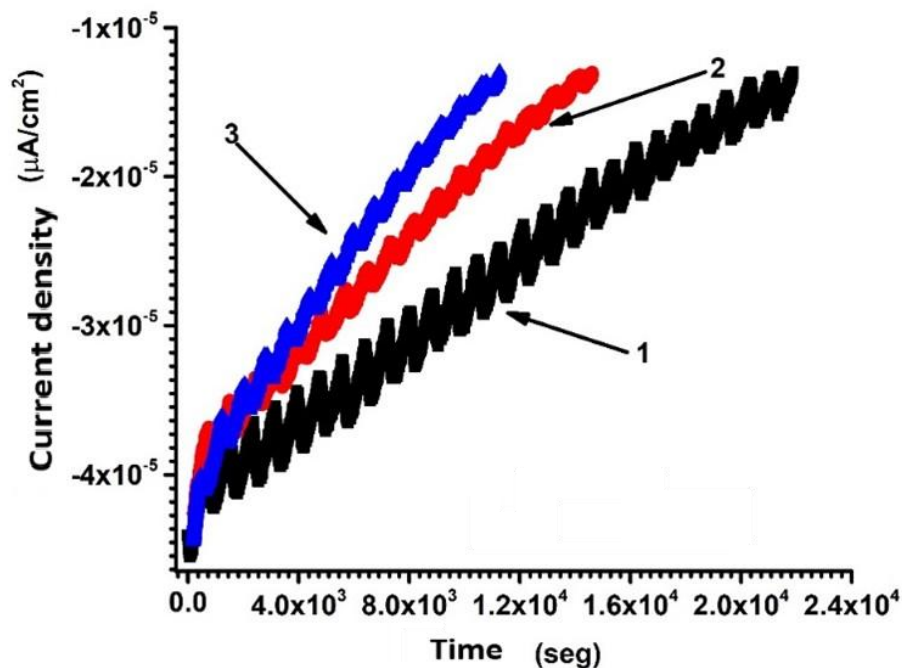


Figure 2

Cathode current density in 1-MCLMB, 2-MCLTT15 and 3-MCLTT30 steels in CAM solution

Source [Own elaboration]

Analysis of hydrogen permeation stream in CAM solution

Figure 3 shows the hydrogen permeation curves of API 5L X60 steel specimens with and without non-conventional heat treatment at cathodic potential (170 mV vs SCE), in standard CAM solution. Curves 1, 2 and 3 are MCLMB, MCLTT30 and MCLTT15 respectively.

Box 4

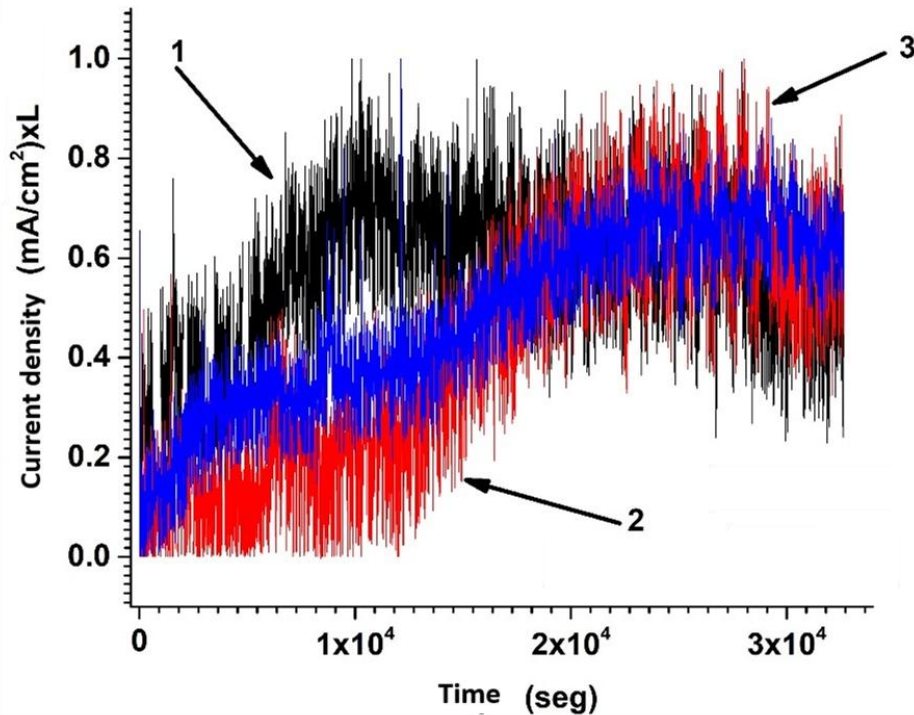


Figure 3

Hydrogen permeation curve of the test pieces with and without non-conventional heat treatment in CAM solution

Source [Own elaboration]

Liang, O. et al.,^{10, 11 13} tells us that in solutions simulating deoxygenated soil with alkaline pH there is an electrical reduction of the solution itself, as well as a drop in ohmic potential, which brings more negative potentials during hydrogen reduction.

The permeation current density of steel with and without unconventional heat treatment shows a great similarity for the three tested conditions.

La i_{∞} , gradually increases to a constant average value of $0.826 \mu\text{Acm}^{-2}$, $0.672 \mu\text{Acm}^{-2}$ and $0.817 \mu\text{Acm}^{-2}$ for the MCLMB, MCLTT15 and MCLTT30 test pieces in CAM solution. The results show that the i_{∞} , of 8.27×10^{-7} was the highest and is for the MCLMB test piece. The stationary current densities of MCLTT15 and MCLTT30 were 6.73×10^{-7} and 8.17×10^{-7} , respectively.

Box 5

Table 2

Parameters associated with hydrogen permeation in steel with and without non-conventional heat treatment in CAM solution

Solution CAM	i_{∞} (μAcm^{-2})	t_L (seg)	J_{∞} ($\text{molcm}^{-2}\text{s}^{-1}$)	D_{eff} (cm^2s^{-1})	C_0 (molcm^{-3})	N_T (cm^3)
MCLMB	8.26e-7	3977	8.52e-12	5.69e-9	1.74e-5	7.95e22
MCLTT15	6.73e-7	12887	6.97e-12	1.63e-9	5.73e-5	1.32e24
MCLTT30	8.17e-7	8959	8.47e-12	2.16e-9	5.13e-5	1.17e24

Table 2 presents the main average parameters associated with the hydrogen permeation curves in CAM solution at 170 mV vs SCE. The highest value of the D_{eff} is given in the MCLTTMB test piece, followed by the MCLTT30 test piece and finally the MCLTT15 test piece. This shows that microstructural changes due to unconventional heat treatment have no great influence on the behavior of hydrogen permeation¹² in CAM solution.

Conclusions

Heat treatment of tempering modifies the microstructure generating bainite and acicular ferrite from ferrite and perlite. The phases present after heat treatment increase the properties of the material in arrival condition. The microstructure favors the formation of reversible traps (dislocations mainly), which modify the behavior in hydrogen diffusion.

Declarations

Conflict of interest

The authors declare that they have no conflict of interest. They have no financial interests or personal relationships that could have influenced this book.

Authors' contribution

Calan-Canche, Damian: Main author of research topic, contribution to methodology and analysis of results.

Pérez-Montejo, Salatiel: Review of the research methodology.

Gonzalez-Sanchez, Jorge: Contribution to the subject of research, review of methodology and analysis of results.

Flores-Chan, J. E.: Analysis of results

Availability of data and materials

The data and materials used in this study are available.

Financing

No financing

Acknowledgements

We extend our thanks to the Universidad Michoacana de San Nicolas de Hidalgo and the Universidad Autónoma de Campeche for their support in carrying out this research.

References

Antecedents

E. G. Dafft, K.B.a.J.E. 1979. [Investigations of hydrogen evolution kinetics and hydrogen absorption by iron electrodes during cathodic polarization](#). Corrosion Science, 19: p. 591-612.

ZÜCHNER, N.B.a.H. 1976. [Electrochemical methods for studying diffusion, permeation and solubility of hydrogen in metals](#). Journal of the Less-Common Metals, 49: p. 223-240.

Basics

Honeycombe, H.K.D.H.B.a.R. 2006. [Steels: Microstructure and properties](#). Third edition ed.: Elsevier Ltd.

Gyu Tae Park, S.U.K., Hwan Gyo Jung, Kyoo Young Kim. 2008. [Effect of microstructure on the hydrogen trapping efficiency and hydrogen induced cracking of linepipe steel](#). Corrosion Science, 50: p. 1865-1871.

Chatterjee, K.B.a.U.K. 2001. [Hydrogen permeation and hydrogen content under cathodic charging in HSLA 80 and HSLA 100 steels](#). *Scripta Materialia*, 44: p. 213-216.

C. F. Dong, X.G.L., Z. Y. Liu, Y. R. Zhang. 2009. [Hydrogen-induced cracking and healing behavior of X70 steel](#). *Journal of alloys and compounds*, 484: p. 966-972.

C. F. Dong, Z.Y.L., X. G. Li, Y. F. Cheng. 2009. [Effects of hydrogen-charging on the susceptibility of X100 pipeline steel to hydrogen-induced cracking](#). *International journal of hydrogen energy*, 34: p. 9879-9884.

Discussions

A. H.S. Bueno, E.D.M., P. Siqueira, J. A. C.P. Gomes. 2014. [Effect of cathodic potential on hydrogen permeation of API grade steels in modified NS4 solution](#). *Materials Science & Engineering*. 507: p. 117-121.

Hung M. Ha, I.M.G., Akram Alfantazi. 2016. [Hydrogen evolution and absorption in an API X100 line pipe steel exposed to near-neutral pH solutions](#). *Electrochimica Acta*, 204: p. 18-30.

M. A. Arafin, J.A.S. 2011. [Effect of bainitic microstructure on the susceptibility of pipeline steels to hydrogen induced cracking](#). *Materials Science & Engineering A*, 528: p. 4927-4940.

A. Torres-Islas, V.M.S.-B., J. L. Albarran, J. C. Gonzalez-Rodriguez. 2005. [Effect of hydrogen on the mechanical properties of X-70 pipeline steel in diluted NaHCO₃ solutions at different heat treatments](#). *International Journal Hydrogen energy*, 30: p. 1317-1322.

Ming-Chun Zhao, Y.-Y.S., Fu Ren Xiao, Ke Yang, Yu Hai Li. 2002. [Investigation on the H₂S-resitant behaviors of acicular ferrite and ultrafine ferrite](#) *Materials Letters*, 57: p. 141-145.





Ping Liang, X.L., Cuiwei Du, Xu Chen. 2009. [Stress corrosion cracking of X80 pipeline steel in simulated alkaline soil solution](#). *Materials & Design*, 30: p. 1712-1717.





Instructions for Scientific, Technological and Innovation Publication





[Title in TNRoman and Bold No. 14 in English and Spanish]

Surname, Name 1st Author*^a, Surname, Name 1st Co-author^b, Surname, Name 2nd Co-author^c and Surname, Name 3rd Co-author^d [No.12 TNRoman]

^a  Affiliation institution,  Researcher ID,  ORCID,  SNI-CONAHCYT ID or CVU PNPC [No.10 TNRoman]

^b  Affiliation institution,  Researcher ID,  ORCID,  SNI-CONAHCYT ID or CVU PNPC [No.10 TNRoman]

^c  Affiliation institution,  Researcher ID,  ORCID,  SNI-CONAHCYT ID or CVU PNPC [No.10 TNRoman]

^d  Affiliation institution,  Researcher ID,  ORCID,  SNI-CONAHCYT ID or CVU PNPC [No.10 TNRoman]

All ROR-Clarivate-ORCID and CONAHCYT profiles must be hyperlinked to your website.

Prot-  [University of South Australia](#) •  [7038-2013](#) •  [0000-0001-6442-4409](#) •  416112

CONAHCYT classification: <https://marvid.org/area-i.php> [No.10 TNRoman]

Area:

Field:

Discipline:

Subdiscipline:

DOI: <https://doi.org/>


Key Handbooks

(Explain the following aspects:)

- What are the main contributions to generating Science and Technology written in this research?
- What are the key aspects to be understood in order to apply to the generation of universal knowledge?
- Outline the main conclusions of the research.
- How many citations did the authors of the work generate in the last year?
- From which institutions do they originate?

Citation: Surname, Name 1st Author, Surname, Name 1st Co-author, Surname, Name 2nd Co-author and Surname, Name 3rd Co-author. Year. Book title. [Pages]. ECORFAN.

Contact e-mail address:

*  [example@example.org]

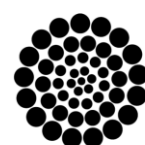
Handbook shelf URL: <https://www.ecorfan.org/handbooks.php>



ISBN XXX-XX-XXXXX-XX-X/© 2009 The Author[s]. Published by ECORFAN-Mexico, S.C. for its Holding X on behalf of Book X. This is an open access chapter under the CC BY-NC-ND license <http://creativecommons.org/licenses/by-nc-nd/4.0/>

Peer Review under the responsibility of the Scientific Committee **MARVID**[®] - in contribution to the scientific, technological and innovation Peer Review Process by training Human Resources for the continuity in the Critical Analysis of International Research.

ECORFAN[®] All rights reserved México – Bolivia – Spain – Ecuador – Cameroon – Colombia – Salvador – Guatemala – Paraguay – Nicaragua – Peru - Democratic Republic of Congo – Taiwan



RENIECYT

Registro Nacional de Instituciones y Empresas Científicas y Tecnológicas

1702902 CONAHCYT

Instructions for Scientific, Technological and Innovation Publication

Abstract [In English]

Must contain up to 150 words

Graphical abstract [In English]

Your title goes here		
Objectives	Methodology	Contribution

Authors must provide an original image that clearly represents the work described in the chapter. Graphical abstracts should be submitted as a separate file. Please note that, as well as each article must be unique. File type: the file types are MS Office files. No additional text, outline or synopsis should be included. Any text or captions must be part of the image file. Do not use unnecessary white space or a "graphic abstract" header within the image file.

Keywords [In English]

Indicate 3 keywords in TN Roman and Bold No. 12

Abstract [In Spanish].

Must contain up to 150 words

Graphical abstract [In Spanish]

Your title goes here		
Objectives	Methodology	Contribution

Authors must provide an original image that clearly represents the work described in the book. Graphical abstracts should be submitted as a separate file. Please note that, as well as each article must be unique. File type: the file types are MS Office files. No additional text, outline or synopsis should be included. Any text or captions must be part of the image file. Do not use unnecessary white space or a "graphic abstract" header within the image file.

Keywords [In Spanish]

Indicate 3 keywords in TN Roman and Bold No. 12

Introduction

ECORFAN® All rights reserved México – Bolivia – Spain – Ecuador – Cameroon – Colombia – Salvador – Guatemala – Paraguay – Nicaragua – Peru - Democratic Republic of Congo – Taiwan

Instructions for Scientific, Technological and Innovation Publication

Text in TNRoman No.12, single space.

General explanation of the subject and explain why it is important.

What is your added value with respect to other techniques?

Clearly focus each of its features

Clearly explain the problem to be solved and the central hypothesis.

Explanation of sections Chapter.

Development of headings and subheadings of the chapter with subsequent numbers

Products in development No.12 TNRoman, single spaced.

Including figures and tables-Editable

In the Chapter content any figure and table should be editable formats that can change size, type and number of letters, for the purposes of edition, these must be high quality, not pixelated and should be noticeable even reducing image scale.

[Indicating the title at the top with No.12 and TNRoman Bold]

Box

Table 1

Title [Should not be images-everything must be editable]

Source [in italic]

Box

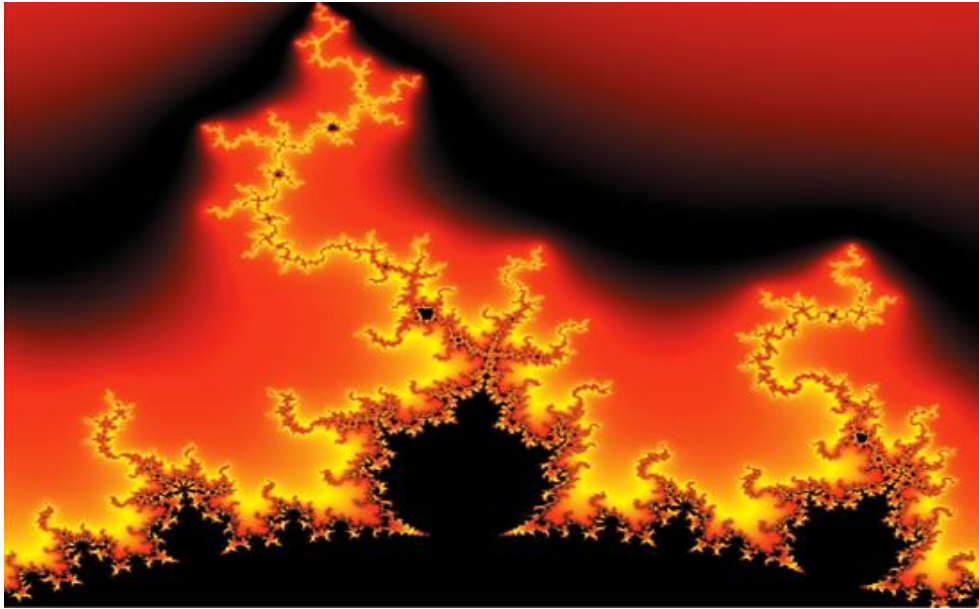


Figure 1

Title [Should not be images-everything must be editable]

Source [in italic]

The maximum number of Boxes is 10 items

For the use of equations, noted as follows:

$$\int_{lim^{-1}}^{lim^1} = \int \frac{lim^1}{lim^{-1}} = \left[\frac{1(-1)}{lim} \right]^2 = \frac{(0)^2}{lim} = \sqrt{lim} = 0 = 0 \rightarrow \infty \quad [1]$$

Must be editable and number aligned on the right side.

Methodology

Develop give the meaning of the variables in linear writing and important is the comparison of the used criteria.

Results

The results shall be by section of the chapter.

Conclusions

Clearly explain the results and possibilities of improvement.

Annexes

Tables and adequate sources.

The international standard is 7 pages minimum and 14 pages maximum.

Declarations

Conflict of interest

The authors declare no interest conflict. They have no known competing financial interests or personal relationships that could have appeared to influence in this chapter.

Instructions for Scientific, Technological and Innovation Publication

Author contribution

Specify the contribution of each researcher in each of the points developed in this research.

Prot-

Benoit-Pauleter, Gerard: Contributed to the project idea, research method and technique.

Availability of data and materials

Indicate the availability of the data obtained in this research.

Funding

Indicate if the research received some financing.

Acknowledgements

Indicate if they were financed by any institution, University or company.

Abbreviations

List abbreviations in alphabetical order.

ANN Artificial Neural Network

References

Use APA system. Should not be numbered, nor with bullets, however if necessary numbering will be because reference or mention is made somewhere in the chapter.

Use the Roman alphabet, all references you have used should be in Roman alphabet, even if you have cited a chapter, book in any of the official languages of the United Nations [English, French, German, Chinese, Russian, Portuguese, Italian, Spanish, Arabic], you should write the reference in Roman alphabet and not in any of the official languages.

Citations are classified the following categories:

Antecedents. The citation is due to previously published research and orients the citing document within a particular scholarly area.

Basics. The citation is intended to report data sets, methods, concepts and ideas on which the authors of the citing document base their work.

Supports. The citing article reports similar results. It may also refer to similarities in methodology or, in some cases, to the reproduction of results.

Differences. The citing document reports by means of a citation that it has obtained different results to those obtained in the cited document. This may also refer to differences in methodology or differences in sample sizes that affect the results.

Discussions. The citing article cites another study because it is providing a more detailed discussion of the subject matter.

The URL of the resource is activated in the DOI or in the title of the resource.

Prot-

Mandelbrot, B. B. [2020]. [Negative dimensions and Hölders, multifractals and their Hölder spectra, and the role of lateral preasymptotics in science](#). Journal of Fourier Analysis and Applications Special. 409-432.

Instructions for Scientific, Technological and Innovation Publication

Intellectual Property Requirements for editing:

- Authentic Signature in Color of [Originality Format](#) Author and Coauthors.
- Authentic Signature in Color of the [Acceptance Format](#) of Author and Coauthors.
- Authentic Signature in blue color of the [Conflict of Interest Format](#) of Author and Co-authors.

Reservation to the Editorial Policy

ECORFAN Handbooks reserves the right to make any editorial changes required to bring the Scientific Work into compliance with the ECORFAN Handbooks Editorial Policy. Once the Scientific Work has been accepted in its final version, ECORFAN Handbooks will send the author the proofs for review. ECORFAN® will only accept the correction of errata and errors or omissions arising from the editing process of the journal, reserving in its entirety the rights of authorship and dissemination of content. Deletions, substitutions or additions that alter the formation of the Scientific Work will not be accepted.

Code of Ethics - Good Practices and Statement of Solution to Editorial Conflicts

Declaration of Originality and unpublished character of the Scientific Work, of Authorship, on the obtaining of data and interpretation of results, Acknowledgements, Conflict of interests, Assignment of rights and distribution.

The Management of ECORFAN-Mexico, S.C. claims to the Authors of the Scientific Work that its content must be original, unpublished and of Scientific, Technological and Innovation content in order to submit it for evaluation.

The Authors signing the Scientific Work must be the same who have contributed to its conception, realization and development, as well as to the obtaining of the data, the interpretation of the results, its writing and revision. The Corresponding Author of the proposed Scientific Work should fill in the following form.

Title of the Scientific Work:

- The submission of a Scientific Paper to ECORFAN Handbooks implies the author's commitment not to submit it simultaneously to the consideration of other serial publications. To do so, he/she must complete the Originality Form for his/her Scientific Paper, unless it is rejected by the Referee Committee, it may be withdrawn.
- None of the data presented in this Scientific Work has been plagiarized or invented. The original data are clearly distinguishable from those already published. And we are aware of the PLAGSCAN test, if a positive plagiarism level is detected, we will not proceed to refereeing.
- The references on which the information contained in the Scientific Work is based are cited, as well as theories and data from other previously published Scientific Works.
- The authors sign the Authorization Form for their Scientific Work to be disseminated by the means that ECORFAN-Mexico, S.C. in its Holding Mexico considers pertinent for the dissemination and diffusion of their Scientific Work, ceding their Scientific Work Rights.
- Consent has been obtained from those who have provided unpublished data obtained through verbal or written communication, and such communication and authorship are properly identified.
- The Author and Co-Authors signing this work have participated in its planning, design and execution, as well as in the interpretation of the results. Likewise, they critically reviewed the work, approved its final version and agree with its publication.
- No signature responsible for the work has been omitted and the criteria for Scientific Authorship have been met.
- The results of this Scientific Work have been interpreted objectively. Any results contrary to the views of the signatories are stated and discussed in the Scientific Work

Copyright and Access

The publication of this Scientific Work implies the assignment of the copyright to ECORFAN-Mexico, S.C. in its Holding Mexico for its ECORFAN Handbooks, which reserves the right to distribute on the Web the published version of the Scientific Work and the availability of the Scientific Work in this format implies for its Authors the compliance with the provisions of the Law of Science and Technology of the United Mexican States, regarding the obligation to allow access to the results of Scientific Research.

Title of the Scientific Work:

Name and surname(s) of Contact Author and Co-authors	Signature
1.	
2.	
3.	
4.	

Principles of Ethics and Editorial Conflict Resolution Statement

Editor's Responsibilities

The Editor undertakes to guarantee the confidentiality of the evaluation process, and may not reveal the identity of the Authors to the Referees, nor may he/she reveal the identity of the Referees at any time.

The Editor assumes the responsibility of duly informing the Author of the stage of the editorial process in which the submitted text is, as well as of the resolutions of the Double Blind Arbitration.

The Editor must evaluate manuscripts and their intellectual content without distinction of race, gender, sexual orientation, religious beliefs, ethnic origin, nationality, or political philosophy of the Authors.

The Editor and its editorial staff of ECORFAN® Holdings will not disclose any information about the submitted Scientific Work to anyone other than the corresponding Author.

The Editor must make fair and impartial decisions and ensure a fair peer review process.

Responsibilities of the Editorial Board

The description of the peer review process is made known by the Editorial Board so that the Authors are aware of the evaluation criteria and will always be ready to justify any controversy in the evaluation process. In case of Plagiarism Detection to the Scientific Work, the Committee notifies the Authors for Violation of the Right of Scientific, Technological and Innovation Authorship.

Responsibilities of the Referee Committee

The Referees undertake to notify any unethical conduct on the part of the Authors and to point out any information that may be a reason to reject the publication of the Scientific Work. In addition, they must undertake to keep confidential the information related to the Scientific Work they evaluate.

Any manuscript received for refereeing must be treated as a confidential document, not to be shown or discussed with other experts, except with the permission of the Editor.

Referees should conduct themselves in an objective manner; any personal criticism of the Author is inappropriate.

Referees should express their views clearly and with valid arguments that contribute to the Scientific, Technological and Innovation achievements of the Author.

Referees should not evaluate manuscripts in which they have conflicts of interest and which have been notified to the Editor before submitting the Scientific Work for evaluation.

Responsibilities of Authors

Authors must guarantee that their Scientific Works are the product of their original work and that the data have been obtained in an ethical manner.

Authors must guarantee that they have not been previously published or that they are not being considered in another serial publication.

Authors must strictly follow the rules for the publication of Scientific Works defined by the Editorial Board.

Authors should consider that plagiarism in all its forms constitutes unethical editorial conduct and is unacceptable; consequently, any manuscript that incurs in plagiarism will be eliminated and will not be considered for publication.

Authors should cite publications that have been influential in the nature of the Scientific Work submitted for refereeing.

Information Services

Indexing - Bases and Repositories

VLEX (Global Legal Intelligence Platform)

RESEARCH GATE (Germany)

MENDELEY (Bibliographic Reference Manager)

GOOGLE SCHOLAR (Citation Indexes-Google)

REDIB (Ibero-American Network of Innovation and Scientific Knowledge- CSIC)

Editorial Services

Citation Identification and H Index

Originality and Authorization Format Management

Handbooks Testing with PLAGSCAN

Evaluation of Scientific Work

Issuance of Referee Certificate

Scientific Work Editing

Web Layout

Indexing and Repository

Publication of Scientific Work

Scientific Work Certificate

Invoicing for Publishing Services

Editorial Policy and Administration

Park Pedregal Business 3580 – Adolfo Ruiz Cortines Boulevard, CP-01900. San Jeronimo Aculco Álvaro Obregón - Mexico City. Tel: +52 1 55 6159 2296, +52 1 55 1260 0355, +52 1 55 6034 9181; E-mail: contact@ecorfan.org www.ecorfan.org

ECORFAN®

Editor in Chief

Vargas-Delgado, Oscar. PhD

Executive Director

Ramos-Escamilla, María. PhD

Editorial Director

Peralta-Castro, Enrique. MsC

Web Designer

Escamilla-Bouchan, Imelda. PhD

Web Diagrammer

Luna-Soto, Vladimir. PhD

Editorial Assistant

Trejo-Ramos, Iván. BsC

Philologist

Ramos-Arancibia, Alejandra. BsC

Advertising and Sponsorship

(ECORFAN® - Mexico – Bolivia – Spain – Ecuador – Cameroon – Colombia - El Salvador – Guatemala – Nicaragua – Peru – Paraguay - Democratic Republic of The Congo - Taiwan),
sponsorships@ecorfan.org

Site Licenses

03-2010-032610094200-01-For printed material, 03-2010-031613323600-01-For electronic material, 03-2010-032610105200-01-For photographic material, 03-2010-032610115700-14-For Compilation of Data, 04 -2010-031613323600-01-For its Web page, 19502-For Ibero-American and Caribbean Indexing, 20-281 HB9-For Latin American Indexing in the Social Sciences and Humanities, 671-For Indexing in Electronic Scientific Journals in Spain and Latin America, 7045008-For dissemination and publication in the Ministry of Education and Culture-Spain, 25409-For its repository in the University Library-Madrid, 16258-For its indexing in Dialnet, 20589-For Indexing in the Directory in the countries of Iberoamerica and the Caribbean, 15048-For the international registration of Congresses and Colloquia.
financingprograms@ecorfan.org

Management Offices

Park Pedregal Business 3580 - Adolfo Ruiz Cortines Boulevard, CP-01900. San Jeronimo Aculco Álvaro Obregón - Mexico City.

21 Santa Lucia, CP-5220. Libertadores -Sucre - Bolivia.

38 Matacerquillas, CP-28411. Moralzarzal -Madrid-Spain.

18 Marcial Romero, CP-241550. Avenue, Salinas I - Santa Elena-Ecuador.

1047 Avenida La Raza - Santa Ana, Cusco-Peru.

Boulevard de la Liberté, Immeuble Kassap, CP-5963.Akwa- Douala-Cameroon.

Avenida Suroeste, San Sebastian - León-Nicaragua.

31 Kinshasa 6593- Republique Démocratique du Congo.

Avenida San Quentin, R 1-17 Miralvalle - San Salvador-El Salvador.

16 kilometers, U.S. highway, Terra Alta house, D7 Mixco Zone 1-Guatemala.

105 Alberdi Rivarola Capitán, CP-2060. Luque City- Paraguay.

69 Street YongHe District, Zhongxin. Taipei-Taiwan.

43 Street # 30 -90 B. El Triunfo CP.50001. Bogotá-Colombia.

